

國立交通大學

電子工程學系 電子研究所

博士論文

多模干涉光子晶體波導元件與

B型抗諧振反射光波導光子晶體波導元件之研究

Investigation on Multimode Interference Photonic Crystal
Waveguide Devices and ARROW-B Photonic Crystal
Waveguide Devices

研究生：呂明峰

指導教授：黃遠東教授

中華民國九十九年七月

多模干涉光子晶體波導元件與
B型抗諧振反射光波導光子晶體波導元件之研究
Investigation on Multimode Interference Photonic Crystal
Waveguide Devices and ARROW-B Photonic Crystal
Waveguide Devices

研究生：呂明峰

Student : Ming-Feng Lu

指導教授：黃遠東

Advisor : Yang-Tung Huang

國立交通大學

電子工程學系 電子研究所

博士論文

A Dissertation

Submitted to Department of Electronics Engineering and

Institute of Electronics

College of Electrical and Computer Engineering

National Chiao Tung University

in partial Fulfillment of the Requirements

for the Degree of

Doctor of Philosophy

in

Electronics Engineering

July 2010

Hsinchu, Taiwan, Republic of China

多模干涉光子晶體波導元件與 B 型抗諧振反射光波導光子晶體波導元件之研究

研究生：呂明峰

指導教授：黃遠東 博士

國立交通大學

電子工程學系電子研究所



本文運用模態匹配法，藉由直波導和彎折波導之場形積分的最大化來改善光子晶體彎折波導的傳輸效率。本文也利用多模干涉效應 (multimode interference effect) 設計一種光子晶體步階式漸變耦合器，此耦合器具有不同的分段長度。多模干涉效應亦用來設計一種極短長度的光子晶體極化分光器 (polarization beam splitter)，此極化分光器的長度只有 7 個晶格常數。另外，有別於傳統波導利用內部全反射機制導光，本論文提出 B 型抗諧振反射光波導 (ARROW-B) 結構之光子晶體波導，在波導的水平方向和垂直方向分別以光子能隙 (photonic band gap) 和 B 型抗諧振反射作為導光的機制，以利垂直方向和單模光纖的耦合。除了高傳輸效率的直波導之外，此結構亦要當作高效率的彎折波導、耦合器及其他光子晶體元件的設計平台。模擬結果顯示 B 型抗諧振反射光波導 (ARROW-B) 結構之光子晶體波導具有高傳輸效率和低彎折損耗，同時光子晶體在水平方向藉步階式漸變耦合結構可使得此波導元件與單模光纖的直接耦合效率有效提昇。

Investigation on Multimode Interference Photonic Crystal Waveguide Devices and ARROW-B Photonic Crystal Waveguide Devices

Student: Ming-Feng Lu

Advisor: Dr. Yang-Tung Huang

Department of Electronics Engineering and Institute of Electronics
National Chiao Tung University

ABSTRACT

A mode matching approach to improve the transmission efficiency of photonic crystal (PC) waveguide bends through maximization of the overlap integral of fields between the straight waveguide and the waveguide bend is presented. The multimode interference (MMI) effect is used to design a PC step tapered coupler with different section lengths. The theoretical design method for a compact PC polarization beam splitter (PBS) based on the MMI effect is shown. The length of the MMI section can be only seven lattice constants. In addition, in contrast to conventional waveguides utilizing the total internal reflection to guide the light, the PC slab waveguide based on a type-B antiresonant reflecting optical waveguide (ARROW-B) structure is proposed for improving the butt-coupling efficiency with a single-mode fiber in the vertical direction. Optical confinement in this device is supported by the photonic band gaps and antiresonance reflection in the lateral and vertical direction, respectively. Besides high-transmission PC waveguides, efficient waveguide bends, couplers and other PC devices could be built on this platform. Simulations show that an ARROW-B-based PC waveguide has high transmissions and low bending losses. With the aid of a PC step tapered coupler, the butt-coupling efficiencies between a single-mode optical fiber and a PC waveguide with an ARROW-B structure can be high for TM and TE modes.

Acknowledgement

It is a long road for me to finish this work. I am deeply grateful to my advisors, Prof. Yang-Tung Huang, for his guidance on my research. Prof. Huang is patient to correct mistakes made by students. I would like to thank Profs. Way-Seen Wang, Yi-Jen Chan, Chii-Chang Chen, Shih-Chao, Jung-Yaw Huang, Po-Tsung Lee, and Gray Lin for their comments on my dissertation.

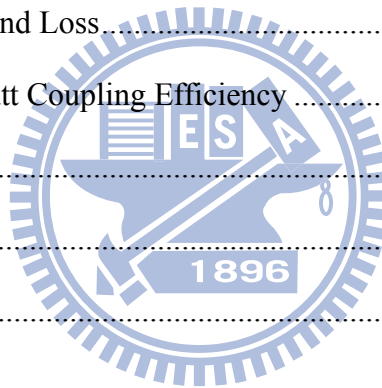
I would like to express my gratitude to graduates of Nanophotonics and Biophotonics Lab., Drs. Jiun-Shiou Deng, Shih-Hsin Hsu, Ting-Hang Pei, Chun-Ting Lin, and Yu-Lin Yang, for their assistance and suggestions on my research. Besides, Jian-Hua Chen, Yu-Hui Huang, Chung-Yu Hong, Shan-Mei Liao, and other members in our laboratory gave me a great deal of technical assistance in experiments for these years.

Finally, I sincerely appreciate my wife, Dr. Su-Ting Shy, for her support and must say sorry to my children, Jessie and Randy, for lacking my companion during their growth. This dissertation is dedicated to them.

Contents

List of Figures	vi
List of Tables	xii
Chapter 1 Introduction	1
Chapter 2 Theory for Analysis	7
2.1 Plane-Wave Expansion Method	7
2.2 Finite-Difference Time-Domain Method	10
2.3 Transfer-Matrix Method	11
2.4 Summary	14
Chapter 3 Transmission Improvement in a Photonic Crystal Waveguide Bend by Mode Matching Technique	16
3.1 Introduction	16
3.2 Transmission Improvement in a PC Waveguide Bend by Mode Matching Technique	17
3.3 Summary	22
Chapter 4 Design of a Photonic Crystal Tapered Coupler Based on Multimode Interference and Mode Matching	24
4.1 Introduction	24
4.2 MMI in PC Waveguides	26
4.3 Design of a PC Tapered Coupler with Different Section Lengths Based on MMI and Mode Matching	32
4.4 Summary	38
Chapter 5 Ultra Compact Photonic Crystal Polarization Beam Splitter Based on Multimode Interference	40
5.1 Introduction	40

5.2	Design of an MMI-based PC PBS by Using the Self-imaging Principle.....	42
5.3	Design of a Compact PC PBS by Difference of Interference between Two Polarizations	50
5.4	Summary	58
Chapter 6 Photonic Crystal Waveguides with Type-B Antiresonant Reflecting Optical Waveguide (ARROW-B) Structures		
6.1	Introduction	60
6.2	Design of a PC Waveguide Based on an ARROW-B Platform.....	62
6.3	Characteristics of a PC Waveguide Based on an ARROW-B Platform	67
6.3.1	Transmission	67
6.3.2	Bend Loss.....	68
6.3.3	Butt Coupling Efficiency	71
6.4	Summary	73
Chapter 7 Conclusion.....		75
Bibliography.....		78



List of Figures

- Fig. 2.1: A multilayer planar waveguide. 14
- Fig. 3.1: (a) Wave transmitted through a conventional 60° photonic crystal waveguide bend at $f = 0.2350$ (a/λ). (b) Field profiles in the straight waveguide (black line) and in the bend without offset (gray line). (c) Lattice points around the bend corner. The lattice points are shifted $0.2a$ along the Γ -K direction indicated by the arrow. (d) Field profiles in the straight waveguide (black line) and in the bend with offset $0.2a$ (gray line). 19
- Fig. 3.2: (a) Wave propagation in a conventional 120° photonic crystal waveguide bend at $f = 0.2350$ (a/λ). (b) Field image in a cavity with three missing holes. (c) Lattice points around the bend corner. The lattice points around the bend corner are shifted $0.2a$ along the Γ -K direction indicated by the arrow. (d) Propagation of wave in the 120° PC waveguide bend with offset. (e) Field image in a three-missing-hole cavity with offset. The first annulus of lattice points around the cavity are shifted $0.2a$ along the Γ -K direction. (f) Field profiles in the straight waveguides corresponding to (a) and (d) (black line), in the three-missing-hole cavity without offset corresponding to (b) (gray line), and in the three-missing-hole cavity with offset corresponding to (e) (gray dashed line). 21
- Fig. 3.3: (a) Transmission spectra of the straight PC waveguide, the 120° PC waveguide bend without offset, and the 120° PC waveguide bend with offset $0.2a$. Point **a** is the low transmission point of the 120° PC bend without offset at $f = 0.2350$ (a/λ). Point **b** is the high

transmission point of the 120° PC waveguide bend with offset $0.2a$ at $f = 0.2350 (a/\lambda)$. Point **c** is a high transmission point of the 120° PC bend without offset at $f = 0.2315 (a/\lambda)$. (b) Field image in the three-missing-hole cavity without offset at $f = 0.2315 (a/\lambda)$. (c) Field profiles in the straight waveguide (black line), and in the three-missing-hole cavity without offset (gray line) at $f = 0.2315 (a/\lambda)$ 22

Fig. 4.1: The PC step tapered coupler which connects one input ridge waveguide and one output single-line-defect PC waveguide. The PC structure is a triangular lattice of air holes with a lattice constant $a = 0.25 \mu\text{m}$ and an air hole radius $r = 0.3a$. The effective indices of the ridge waveguide and the cladding layer are 3.343 and 3.342, respectively. 27

Fig. 4.2: Various lengths of PC tapered couplers used to compare their transmission from a $1.6\text{-}\mu\text{m}$ -wide ridge waveguide to a single-line-defect PC waveguide. The section lengths of each segment in the PC tapered coupler are $2.5a$, $3.5a$, and $4.5a$ in cases (a), (b), and (c), respectively. 28

Fig. 4.3: Self-imaging phenomena in multiple-line-defect PC waveguides. The light is launched (a) from W1 to W3, and (b) from W3 to W1. The dual-head arrows represent the distances between two single images. 29

Fig. 4.4: Transmission efficiencies (a) from W3 to W1, (b) from W5 to W3, and (c) from W7 to W5 PC waveguide. A Gaussian wave is launched from the wider to the narrower section to test the transmission between two PC waveguides with different widths.

The transmissions vary periodically with the launch position of the light source.....	31
Fig. 4.5: (a) Projected band diagram of the single-line-defect PC waveguide. (b) Field profile of the fundamental mode in the W1 PC waveguide. (c) Projected band diagram of the W3 PC waveguide.....	33
Fig. 4.6: The section length of W3 in a PC step tapered coupler can be fine-tuned from $3.5a$ to $3.9a$ by adjusting the positions of the first two air holes of the W1 waveguide.....	34
Fig. 4.7: (a) MMI phenomenon in the well-designed PC tapered coupler with different section lengths. The taper structure is the same as the case in Fig. 4.2(a) except that the section length of W3 is fine-tuned from $2.5a$ to $3.9a$. (b) Power profile of a single image in the W1 PC waveguide. (c) Power profile of two-fold image at the entrance of the W3 PC waveguide. (d) Transmission spectrum of the well-designed PC tapered coupler as a function of the operating wavelength.....	36
Fig. 4.8: The taper structure of the first test case. It is the same as that of the case in Fig. 4.2(a) except that the section length of W3 is adjusted from $2.5a$ to $11.7a$, which is the length of one two-fold-image distance plus one single-image distance.	37
Fig. 4.9: (a) The taper structure of the second test case. It is the same as that of the case in Fig. 4.2(a) except that the section length of W3 is $3.5a$. The radius of the first two air holes of the W1 waveguide is modified from $0.3a$ (the dashed line circles) to $0.16a$ (the solid line circles). The equivalent section length of W3 after fine tuning is $3.84a$. (b) Transmission as a function of the radius of the first two	

air holes of the W1 waveguide. The maximum coupling efficiency is 85.1% when the radius of the modified air holes is $0.16a$	38
Fig. 5.1: (Color) Band diagram of the PC structure. The PC structure is a square lattice of dielectric rods with refractive index 4.1 and the radius of dielectric rods $r = 0.38a$, where a is the lattice constant of the PC.	45
Fig. 5.2: Schematic structure of a PC PBS based on the MMI effect. The 1×2 MMI coupler has one input and two output access ports. W1 PC waveguides act as the access waveguides. A W5 PC waveguide acts as the multimode interference region and its section length is to be designed.	45
Fig. 5.3: (a) TE and (b) TM projected band diagram of the W1 PC waveguide. This PC waveguide supports two TE defect modes and one TM defect mode.	46
Fig. 5.4: TE projected band diagram of the W5 PC waveguide. This PC multimode waveguide supports four modes at the operating frequency of $0.444 (a/\lambda)$	47
Fig. 5.5: TM projected band diagram of the W5 PC waveguide. This multimode PC waveguide supports four guided modes at the operating frequency of $0.444 (a/\lambda)$	49
Fig. 5.6: (Color) Steady-state electric field distributions of the PC PBS designed by the self-imaging principle for (a) a TE, and (b) a TM wave.	50
Fig. 5.7: Open-ended W5 PC waveguide to be studied. The optical powers within the upper- (Channel 1) and lower- (Channel 2) half portions of the open-ended W5 PC waveguide are measured by Monitors A	

and B, respectively.	52
Fig. 5.8: Transmissions of a TE wave measured by Monitor A (solid curve) and Monitor B (dashed curve) under different positions within the W5 PC waveguide. The first peaks of transmission along Channel 2 and Channel 1 happen at about $44a$ and $88a$, respectively.	52
Fig. 5.9: Transmissions of TM wave measured by Monitor A (solid curve) and Monitor B (dashed curve) under different positions within the W5 PC waveguide.	53
Fig. 5.10: (Color) Normalized field profiles of the (a) W1 and (b) W5 PC waveguides.	54
Fig. 5.11: (Color) (a) Power profile of all TM modes within the W5 PC waveguide. (b) Field superposition of all modes along the z -axis at $y = 2a$. (c) Power profile of a TM wave at $z = 6a$	55
Fig. 5.12: Transmissions of TM wave measured by Monitor B (dashed curve) in Fig. 5.9 and TE wave measured by Monitor A (solid curve) in Fig. 5.8 under different positions within the W5 PC waveguide. It can be seen that both transmissions at Channel 1 for TE wave and at Channel 2 for TM wave are high at $6a$	57
Fig. 5.13: Structure of the ultra compact PC PBS. The length of the MMI region is only $7a$. The TE wave is routed to the upper output port (Port 1) and TM wave to the lower output port (Port 2).	57
Fig. 5.14: Steady-state electric field distributions of the compact PC PBS for (a) TE and (b) TM waves.	59
Fig. 6.1: (a) Cross sectional view of an ARROW structure. (b) Index profile of an ARROW structure. (c) Index profile of an ARROW-B structure.	62

Fig. 6.2: A photonic crystal waveguide based on an ARROW-B platform.....	63
Fig. 6.3: Propagation losses of the ARROW-B waveguide as a function of the thickness of the first cladding layer for (a) TE modes and (b) TM modes.	65
Fig. 6.4: The joint band gap of a photonic crystal structure with a triangular lattice. The refractive index of background is 3.2.....	66
Fig. 6.5: Transmission spectra for TE and TM modes.....	68
Fig. 6.6: (a) The wave propagation in a 60° PC waveguide bend without offset (TE mode as an example). (b) The propagation of wave in the 60° PC waveguide bend with offset. The lattice points around the bend corner are shifted $0.3a$ along the Γ -K direction indicated by the arrow. (c) The wave propagation in a 120° PC waveguide bend without offset (TE mode as an example). (d) The propagation of wave in the 120° PC waveguide bend with offset. The lattice points around the bend corner are shifted $0.3a$ along the Γ -K direction indicated by the arrow.....	70
Fig. 6.7: (a) An ARROW-B-based PC waveguide coupled directly with a single-mode optical fiber. (b) The top view of (a). (c) An ARROW-B-based PC waveguide coupled with a single-mode optical fiber through a three-dimensional PC tapered coupler. (d) The top view of (c).....	72

List of Tables

Table 5.1: Parameters used to calculate the locations of images of the W5 PC waveguide for a TE wave at $0.444 (a/\lambda)$	48
Table 5.2: Parameters used to calculate the locations of the mirror image of the W5 PC waveguide for a TM wave at $0.444 (a/\lambda)$	48
Table 5.3: Transmissions, extinction ratios and insertion losses of the PC PBS designed by the self-imaging principle.	50
Table 5.4: Transmissions, extinction ratios and insertion losses of the compact PC PBS.....	59



Chapter 1

Introduction

Photonic crystals (PCs) are periodic dielectric structures that exhibit photonic band gaps (PBGs) and have attracted extensive interest in recent years. Due to the periodicity of refractive indices in a photonic crystal, light of certain wavelength could not propagate in this periodic lattice. The photonic band gap is caused by the Bragg's diffraction and is similar to the electronic bandgap in semiconductors. Photonic crystals are also named as electromagnetic crystals. The idea of "photonic crystal" was first proposed by Eli Yablonovitch in 1987 [1]. Sajeev John proposed the light confinement of photonic crystal at the same time [2]. But someone regarded that a detailed investigation of the effect of a photonic band gap on the spontaneous emission of embedded atoms and molecules has been performed by V. P. Bykov in 1972 [3], [4]. He obtained the energy and the decay law of the excited state with transition frequency in the photonic band gap, and calculated the spectrum which accompanies this decay. Bykov's investigation revealed that the spontaneous emission could be strongly suppressed in volumes much greater than the wavelength. However, Yablonovitch et al. produced the first artificial photonic crystal by drilling a lot of small holes with a diameter just below 1 mm in a dielectric substrate. This material, which became known as "Yablonovite", prevented microwaves from propagating in any direction. After the efforts of many researchers, photonic crystal becomes one of the most exciting and fast-growing fields in optoelectronics now. Today, the field of optoelectronics is in a stage of development similar to where the field of electronics was many decade of years ago.

The behavior of light in a photonic crystal can be compared to the displacement of

electrons and holes in a semiconductor. The photons of certain wavelengths cannot pass photonic crystals just as the electrons of certain energies are excluded in semiconductors. The electrons traveling through the lattice of a crystal experience a periodic potential. Existence of this periodic potential leads to the formation of bandgaps. No electrons will be found in these forbidden energy gaps. However, electrons can exist within the band gap if the periodicity of the lattice is broken by a vacancy (missing atom), a substitutional site (impurity atom occupying a site), or an interstitial site. To a photon, the periodicity in refractive index looks just like the periodic potential that an electron traveling through. This results in the formation of a photonic band gap.

By making point defects in a photonic crystal, light can be localized or trapped in these defects [5]-[10]. Adding localized states in the bandgap has a direct analogy to doping effects for semiconductors. Such a resonant cavity can be utilized to produce a very sharp channel drop filter through resonant tunneling. Another application of resonant cavities is enhancing the efficiency of lasers by taking the advantage of the density of states at the resonant frequency is very high. By changing the size or the shape of the defect, its frequency can easily be tuned.

One-dimensional (1D) photonic crystals are structures of alternating layers with different refractive indices, including optical coatings and Bragg stacks [11]-[15]. Only light of the allowed modes can propagate through this layer composition. Incident light of a frequency within the photonic stop band will be reflected by this structure.

Planar patterns can be generated by standard photolithography or electron-beam lithography and dry etching techniques of semiconductors. Therefore, fabrications of two-dimensional (2D) PC structures are relatively easy by utilizing tools and techniques of silicon process [16]-[19]. The critical factors to be controlled are the refractive index contrast, the arrangement of the lattice and the fraction of high and low index materials in the lattice. In principle, the higher the refractive index contrast is the larger the

bandgap is achievable.

A three-dimensional (3D) photonic crystal will have a complete bandgap [20]-[23]. However, the complicated structure is apparently difficult to fabricate. The first experimental evidence of a 3D PC was presented by E. Yablonovitch and co-workers in 1991. This was an array of holes drilled into a high refractive index material showing a stop band for the transmission of microwave radiation that extended from 10 to 13 GHz. The demonstration by E. Yablonovitch is known as the “three-cylinder model” today and presents a structure with the symmetry of the diamond. Using techniques drawn from semiconductor manufacturing, Shawn Lin had devised the first 3D photonic crystal operating at a wavelength of 1.5 microns [24]. The crystal is a tiny pile of criss-crossed polysilicon rods with air in between. Each silicon bar is 1.2 microns wide and 1.5 microns high. As predicted, light of infrared wavelengths cannot escape from the structure. Susumu Noda fabricated a 3D photonic crystal by the method of wafer bonding [25]. This method basically uses wafer fusion to stack semiconductor stripes thus forming a 3D crystal. The resulting crystal structure is an asymmetrical f.c.c. structure and a bandgap is formed in all directions. The important point of the method is that the positions of parallel stripes are displaced from each other by half a period. To achieve this, they have developed equipment used to align the optical laser diffraction pattern.

Light propagation with a frequency within the PBGs is forbidden. While line defects are introduced into PCs, the PC waveguides are formed and provide a powerful way to control the flow of electromagnetic waves. From the simulations and experiments of recent years, the planar photonic crystal (PPC) waveguides have been demonstrated to have good confinement of light [26]-[31]. The most important is that manufacturing of PPC waveguides can use the same mature technologies in semiconductor. However, the same as conventional waveguides, there is a problem of vertical loss because light is

localized to the slab by means of the total internal reflection in the vertical direction. Three-dimensional PC structures may solve this problem. But from a manufacturing point of view, the 3D technologies, either the wafer bonding or cross rods, are very difficult to realize. Production cost is another issue must be concerned.

Most of the researchers on photonic crystals in Taiwan focused on the study of photonic band theory by finite-difference time-domain method [32]-[35]. The group of National Tsing Hua University studied the photonic crystals in the frequency range of terahertz to reveal the formation of photonic band gaps [36]-[40]. Dr. Hsieh, professor of National Chiao Tung University, used the Green function to calculate the defect modes of photonic crystals and observed the phenomena of negative refractive index [41]-[43]. The PC nanocavity was used to improve the performance of lasers [44]. Some researchers discussed the multimode interference phenomena in photonic crystals and designed the PC beam splitters [45]-[49].

Conventional waveguides utilize the total internal reflection to guide the light. The antiresonant reflecting optical waveguide (ARROW) structures, which utilize the antiresonant reflection instead of the total internal reflection, have the advantages of high coupling efficiency, flexible design and low transmission loss [50]-[54]. ARROW structures based on the materials of high contrast ratio of refractive index have been widely used in couplers, splitters, waveguides, photodetectors, etc. However, ARROW structures guide TE waves only, whereas type-B antiresonant reflecting optical waveguide (ARROW-B) structures support TE and TM modes [55]-[57].

The core size of traditional PC slab waveguide is less than one micron. In contrast, the core thickness of a single-mode optical fiber is in size on the order of a few microns. The coupling losses due to mismatch of core sizes are over 20 dB. Measurements and further applications of PC devices are limited by the coupling issue. So, a PC slab waveguide based on an ARROW-B platform is proposed in this study to solve the

coupling issue between a PC waveguide and a single-mode optical fiber in the vertical direction. Besides high-transmission PC waveguides, efficient waveguide bends, couplers, and other devices should be built on this platform. The multimode interference (MMI) effect and mode matching technique are used to design an efficient PC waveguide bend, a PC step tapered coupler with different section lengths, and a compact PC polarization beam splitter.

The organization of this dissertation is as follows. In Chapter 2, several numerical methods for analyzing the PC structures and optical waveguides, such as the plane-wave expansion (PWE) method, finite-difference time-domain (FDTD) method and transfer-matrix method are reviewed.

An approach to improve the transmission efficiency of PC waveguide bends through maximization of the overlap integral of fields between the straight waveguide and the waveguide bend is presented in Chapter 3. By shifting the lattice points around the bend corner, the bound state in the waveguide bend and the guided mode in the straight waveguide are matching, and the transmissions of 60° and 120° PC waveguide bends can be significantly improved. The bound state in a PC waveguide bend is similar to a cavity mode; therefore, the PC waveguide bend performs a narrow-band transmission. Frequency-shift of the spectra for a PC waveguide bend due to this lattice shifting can also be observed.

In Chapter 4, the multimode interference phenomena in multiple-line-defect PC waveguides are observed. Step tapered couplers, which act as mode converters, are usually used between PC waveguides and other optical devices for efficient coupling. It is found that the optimal length of each section in a PC step tapered coupler is related to the imaging length of MMI. Therefore, a PC step tapered coupler with different section lengths can be designed. Because the modes are matched between two adjacent sections and the scattering losses occurring at the corners of abrupt steps are reduced, it

can provide an excellent transmission between PC waveguides and other optical devices. This study also reveals the reason why in some cases, the transmission of PC step tapered couplers decreases counterintuitively when the taper length is increased.

In Chapter 5, the theoretical design method for a compact PC polarization beam splitter (PBS) based on the MMI effect is proposed. The size of a conventional MMI device designed by the self-imaging principle is not compact enough; therefore, we design a compact PC PBS based on the difference of interference effect between TE and TM modes. Within the MMI coupler, the dependence of interference of modes on propagation distance is weak for a TE wave and strong for a TM wave; as a result, the length of the MMI section can be only seven lattice constants. Simulation results show that the insertion losses are low and the extinction ratios are high for TE and TM modes.

In Chapter 6, a PC waveguide based on an ARROW-B platform is proposed to solve the coupling issue between a PC waveguide and a single-mode optical fiber in the vertical direction. The optical confinement of this device is supported by the photonic band gap in the lateral plane and by the antiresonant reflection instead of the total internal reflection in the vertical direction of the slab. Simulations show that an ARROW-B-based PC waveguide has high transmissions and low bending losses both for TM and TE modes. With the aid of a PC tapered coupler, the butt-coupling efficiencies between a single-mode optical fiber and a PC waveguide with an ARROW-B structure can be high for TM and TE modes.

Finally, a conclusion will be given and future works will be suggested in Chapter 7.

Chapter 2

Theory for Analysis

The basic theory of electromagnetism in periodic structures and interpretation of the band diagrams of photonic crystals can be found in a lot of literatures [58]-[62]. Numerical methods, such as the plane-wave expansion (PWE) method, $k \cdot p$ method, and finite-difference time-domain (FDTD) method, are used for producing band diagrams of photonic bandgap structures. The plane-wave expansion technique is based on the Fourier expansion of electromagnetic fields and dielectric functions, and is suitable for calculation of a global band structure [63]. The $k \cdot p$ method is for calculating the band structure around a particular k value in the Brillouin zone. The FDTD method is for the problems of dispersion and lossy materials [64], [65]. Usually, the band diagram is calculated along high symmetry directions in the first Brillouin zone. In the cases where the photonic crystal is used to trap the light, such as a cavity or a waveguide, this is sufficient. However, in phenomena of superprism or self collimation, we have to calculate the band diagram in the whole Brillouin zone. In this chapter, the transfer-matrix method for analyzing the optical waveguides is also reviewed.

2.1 Plane-Wave Expansion Method

The Maxwell's equations in SI units without sources (\mathbf{J} and ρ are zero) can be expressed as

$$\nabla \times \mathbf{E} = -\frac{\partial \mathbf{B}}{\partial t} + \mathbf{J} = -\frac{\partial \mathbf{B}}{\partial t}, \quad (2.1)$$

$$\nabla \times \mathbf{H} = \frac{\partial \mathbf{D}}{\partial t}, \quad (2.2)$$

$$\nabla \cdot \mathbf{D} = \rho = 0, \quad (2.3)$$

$$\nabla \cdot \mathbf{B} = 0, \quad (2.4)$$

where \mathbf{H} and \mathbf{E} are the magnetic and electric fields, \mathbf{B} is the magnetic induction, \mathbf{D} is the electric displacement, \mathbf{J} and ρ are the current and charge densities. Combining Eqs. (2.1) and (2.2) with the constitutive relations of linear and lossless materials,

$$\mathbf{D} = \varepsilon \mathbf{E}, \quad (2.5)$$

$$\mathbf{B} = \mu_0 \mathbf{H}, \quad (2.6)$$

the wave equations become

$$\frac{1}{\varepsilon} \nabla \times \nabla \times \mathbf{E} = -\frac{1}{c^2} \frac{\partial^2 \mathbf{E}}{\partial t^2}, \quad (2.7)$$

$$\nabla \times \frac{1}{\varepsilon} \nabla \times \mathbf{H} = -\frac{1}{c^2} \frac{\partial^2 \mathbf{H}}{\partial t^2}, \quad (2.8)$$

where ε is the dielectric function, μ_0 is the vacuum permeability, and c is the speed of light in vacuum. Assume that within the frequency ranges of interest, the dielectric function is independent of \mathbf{E} and frequency. Also assume that the absorption of light by materials can be neglected, ε is a real number in this case. All of these magnetic, electric and dielectric functions are functions of the position vector \mathbf{r} and the time t . By separation of time and space, the fields expanding into a set of harmonic modes are

$$\mathbf{E}(\mathbf{r}, t) = \mathbf{E}(\mathbf{r}) \exp(-j\omega t), \quad (2.9)$$

$$\mathbf{H}(\mathbf{r}, t) = \mathbf{H}(\mathbf{r}) \exp(-j\omega t), \quad (2.10)$$

where ω is the eigen-angular frequency and $\mathbf{H}(\mathbf{r})$, $\mathbf{E}(\mathbf{r})$ are the eigen-functions. Then, the wave equations are converted to the Helmholtz equations:

$$\frac{1}{\varepsilon(\mathbf{r})} \nabla \times \nabla \times \mathbf{E}(\mathbf{r}) = \frac{\omega^2}{c^2} \mathbf{E}(\mathbf{r}), \quad (2.11)$$

$$\nabla \times \frac{1}{\epsilon(\mathbf{r})} \nabla \times \mathbf{H}(\mathbf{r}) = \frac{\omega^2}{c^2} \mathbf{H}(\mathbf{r}). \quad (2.12)$$

These equations are referred to as the “master equations” in the field of photonic crystals. The possible solution to the Helmholtz equation is a plane wave. Those on the left of these equations are Hamiltonian operators. From the Bloch-Floquet theorem, the solution of a Hermitian eigen-problem is in the form of a periodic function as

$$\mathbf{E}(\mathbf{r}) = \mathbf{E}_{kn}(\mathbf{r}) = v_{kn}(\mathbf{r}) \exp(j\mathbf{k} \cdot \mathbf{r}), \quad (2.13)$$

$$\mathbf{H}(\mathbf{r}) = \mathbf{H}_{kn}(\mathbf{r}) = u_{kn}(\mathbf{r}) \exp(j\mathbf{k} \cdot \mathbf{r}), \quad (2.14)$$

where \mathbf{k} is the wave vector, n is the band index, and u, v are periodic functions of position. By the Fourier series expansion,

$$\mathbf{E}_{kn}(\mathbf{r}) = \sum_{\mathbf{G}} \mathbf{E}_{kn}(\mathbf{G}) \exp[j(\mathbf{k} + \mathbf{G}) \cdot \mathbf{r}], \quad (2.15)$$

$$\mathbf{H}_{kn}(\mathbf{r}) = \sum_{\mathbf{G}} \mathbf{H}_{kn}(\mathbf{G}) \exp[j(\mathbf{k} + \mathbf{G}) \cdot \mathbf{r}], \quad (2.16)$$

$$\frac{1}{\epsilon(\mathbf{r})} = \sum_{\mathbf{G}} \kappa(\mathbf{G}) \exp(j\mathbf{G} \cdot \mathbf{r}), \quad (2.17)$$

where \mathbf{G} is the reciprocal lattice vector, the eigenvalue equations can be expressed as

$$-\sum_{\mathbf{G}'} \kappa(\mathbf{G} - \mathbf{G}')(\mathbf{k} + \mathbf{G}') \times \{(\mathbf{k} + \mathbf{G}') \times \mathbf{E}_{kn}(\mathbf{G}')\} = \frac{\omega_{kn}^2}{c^2} \mathbf{E}_{kn}(\mathbf{G}) \quad (2.18)$$

$$-\sum_{\mathbf{G}'} \kappa(\mathbf{G} - \mathbf{G}')(\mathbf{k} + \mathbf{G}') \times \{(\mathbf{k} + \mathbf{G}') \times \mathbf{H}_{kn}(\mathbf{G}')\} = \frac{\omega_{kn}^2}{c^2} \mathbf{H}_{kn}(\mathbf{G}). \quad (2.19)$$

When the eigen-frequencies ω are plotted as a function of the wave vector \mathbf{k} , the band diagram of a photonic crystal is formed. The lattice prohibits the propagation of certain waves; therefore, gaps are formed in the energy band structure.

The fields propagating within the lattice plane of two-dimensional PCs are separable and support TE and TM polarizations. Assume that the PC structure is uniform in the

x -direction, the equations can be expressed as

$$\sum_{G'_{yz}} \kappa(\mathbf{G}_{yz} - \mathbf{G}'_{yz}) |\mathbf{k}_{yz} + \mathbf{G}'_{yz}|^2 \mathbf{E}_x(\mathbf{G}'_{yz}) = \frac{\omega^2}{c^2} \mathbf{E}_x(\mathbf{G}_{yz}) \quad (2.20)$$

$$\sum_{G'_{yz}} \kappa(\mathbf{G}_{yz} - \mathbf{G}'_{yz})(\mathbf{k}_{yz} + \mathbf{G}_{yz}) \cdot (\mathbf{k}_{yz} + \mathbf{G}'_{yz}) \mathbf{H}_x(\mathbf{G}'_{yz}) = \frac{\omega^2}{c^2} \mathbf{H}_x(\mathbf{G}_{yz}). \quad (2.21)$$

The refractive index distribution is assumed to be identical at all the frequencies of the modes being found. The operator is Hermitian only if the material is lossless. Consequently, the PWE method cannot treat the problems of dispersion and lossy materials. These limitations can be avoided by using the FDTD method.

2.2 Finite-Difference Time-Domain Method

The FDTD method is widely used as a propagation solution technique in integrated optics. This method is a rigorous solution to Maxwell's equations and does not have any approximations or theoretical restrictions.

Maxwell's equations without currents and isolated charges can be written as six simple scalar equations as:

$$\frac{\partial H_x}{\partial t} = -\frac{1}{\mu} \left(\frac{\partial E_y}{\partial z} - \frac{\partial E_z}{\partial y} \right), \quad (2.22)$$

$$\frac{\partial H_y}{\partial t} = -\frac{1}{\mu} \left(\frac{\partial E_z}{\partial x} - \frac{\partial E_x}{\partial z} \right), \quad (2.23)$$

$$\frac{\partial H_z}{\partial t} = -\frac{1}{\mu} \left(\frac{\partial E_x}{\partial y} - \frac{\partial E_y}{\partial x} \right), \quad (2.24)$$

$$\frac{\partial E_x}{\partial t} = -\frac{1}{\varepsilon} \left(\frac{\partial H_z}{\partial y} - \frac{\partial H_y}{\partial z} \right), \quad (2.25)$$

$$\frac{\partial E_y}{\partial t} = -\frac{1}{\varepsilon} \left(\frac{\partial H_x}{\partial z} - \frac{\partial H_z}{\partial x} \right), \quad (2.26)$$

$$\frac{\partial E_z}{\partial t} = -\frac{1}{\varepsilon} \left(\frac{\partial H_y}{\partial x} - \frac{\partial H_x}{\partial y} \right). \quad (2.27)$$

These equations describe that the temporal change in the \mathbf{E} field is dependent upon the spatial variation of the \mathbf{H} field, and vice versa. Therefore, we can solve Maxwell's equations by discretizing these equations via central differences in time and space. The most common method is based on Yee's mesh and then numerically solves these equations in software [66], [67].

The boundary conditions at the spatial edges of the computational domain must be carefully considered. An absorbing boundary condition that eliminates any outward propagating energy that impinges on the domain boundaries. One of the most effective is the perfectly matched layer (PML), in which the wave impedance remains constant, absorbing the energy without inducing reflections [68], [69]. Periodic boundary conditions (PBC) are applied to PBG structures in some cases. This boundary condition is chosen such that the simulation is equivalent to an infinite structure composed of the basic computational domain repeated endlessly in all dimensions.

2.3 Transfer-Matrix Method

The transfer-matrix method is used to analyze the modal characteristics, including propagation constants, dispersion relations, field distributions, and propagation losses, of multilayer structures [70]. The Maxwell's equations in a homogeneous, isotopic, and lossless material can be expressed as

$$\nabla^2 \mathbf{E} - \mu\varepsilon \frac{\partial^2 \mathbf{E}}{\partial t^2} = 0, \quad (2.28)$$

$$\nabla^2 \mathbf{H} - \mu\epsilon \frac{\partial^2 \mathbf{H}}{\partial t^2} = 0, \quad (2.29)$$

where μ and ϵ are the magnetic permeability and the dielectric permittivity. Consider a plane wave propagating along the z -direction with a propagation constant β , the field components E_y , H_x , and H_z for the transverse electric (TE) mode becomes

$$E_y = -\frac{1}{j\omega\epsilon} \left(\frac{\partial H_z}{\partial x} + j\beta H_x \right), \quad (2.30)$$

$$H_x = -\frac{1}{j\omega\mu} E_y, \quad (2.31)$$

$$H_z = -\frac{1}{j\omega\mu} \frac{\partial E_y}{\partial x}, \quad (2.32)$$

If we define two variables U and V as

$$U = E_y, \quad (2.33)$$

$$V = \omega\mu H_z, \quad (2.34)$$

and substitute them into Eqs. (2.30) to (2.32), we obtain

$$\frac{\partial^2 U}{\partial x^2} = (\beta^2 - k^2 n^2) U, \quad (2.35)$$

$$\frac{\partial^2 V}{\partial x^2} = (\beta^2 - k^2 n^2) V. \quad (2.36)$$

The general solutions of Eqs. (2.35) and (2.36) are

$$U = A \exp(-j\kappa x) + B \exp(+j\kappa x), \quad (2.37)$$

$$V = \kappa [A \exp(-j\kappa x) - B \exp(+j\kappa x)], \quad (2.38)$$

where

$$\kappa = k^2 n^2 - \beta^2. \quad (2.39)$$

Assume that the input values at the plane $x = 0$ are $U(0) = U_0 = A + B$ and $V(0) = V_0 = \kappa(A - B)$, the constants A and B are

$$A = \frac{1}{2} \left(U_0 + \frac{V_0}{\kappa} \right), \quad (2.40)$$

$$B = \frac{1}{2} \left(U_0 - \frac{V_0}{\kappa} \right). \quad (2.41)$$

The relation between the quantities of output U , V and input U_0 , V_0 can be described by a matrix \mathbf{M} ,

$$\begin{pmatrix} U_0 \\ V_0 \end{pmatrix} = \mathbf{M} \begin{pmatrix} U \\ V \end{pmatrix}. \quad (2.42)$$

where \mathbf{M} is the characteristic matrix of the layer and has the form

$$\mathbf{M} = \begin{pmatrix} \cos \kappa x & (j/\kappa) \sin \kappa x \\ j\kappa \sin \kappa x & \cos \kappa x \end{pmatrix}. \quad (2.43)$$

Consider a multilayer waveguide as shown in Fig. 2.1, the characteristic matrix of the i th layer is

$$\mathbf{M} = \begin{pmatrix} \cos \kappa_i d_i & (j/\kappa_i) \sin \kappa_i d_i \\ j\kappa_i \sin \kappa_i d_i & \cos \kappa_i d_i \end{pmatrix}. \quad (2.44)$$

where d_i is the thickness of each layer. The relation between the quantities of cover layer U_c , V_c and substrate layer U_s , V_s can be expressed as

$$\begin{pmatrix} U_s \\ V_s \end{pmatrix} = \mathbf{M} \begin{pmatrix} U_c \\ V_c \end{pmatrix}. \quad (2.45)$$

\mathbf{M} is the characteristic matrix of the multilayer and has the form

$$\mathbf{M} \equiv \begin{pmatrix} m_{11} & m_{12} \\ m_{21} & m_{22} \end{pmatrix} = \prod_i \mathbf{M}_i = \mathbf{M}_1 \mathbf{M}_2 \cdots \mathbf{M}_n. \quad (2.46)$$

There are no input components, i.e., $A_s = 0$, $B_c = 0$, for the modes guided in a multilayer slab waveguide. Inserting these conditions into Eq. (2.45) yields the dispersion relation

$$\kappa_s (m_{11} + \kappa_c m_{12}) + (m_{21} + \kappa_c m_{22}) = 0. \quad (2.47)$$

Following the same steps, the dispersion relation for the TM mode is

$$-\frac{\kappa_s}{n_s^2} (m_{11} - \frac{\kappa_c}{n_c^2} m_{12}) + (m_{21} - \frac{\kappa_c}{n_c^2} m_{22}) = 0. \quad (2.48)$$

Solving these dispersion relations, we can obtain the propagation constant for each mode.

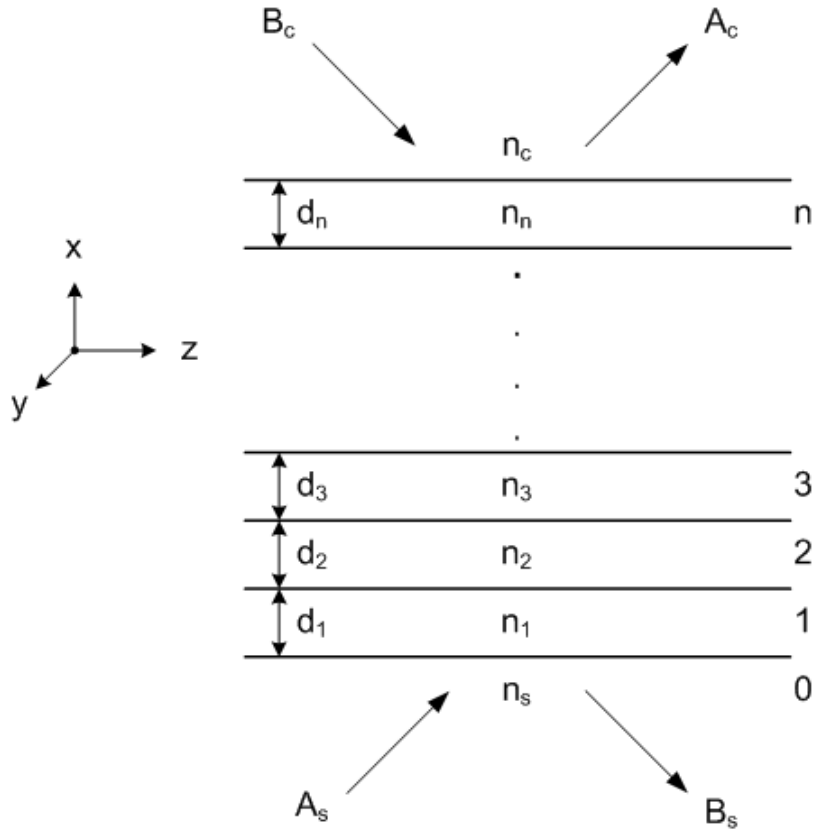


Fig. 2.1: A multilayer planar waveguide.

2.4 Summary

There are other computation methods proposed to solve the PBGs of photonic crystals. Steven G. Johnson and John D. Joannopoulos proposed a fully vectorial, three-dimensional algorithm, block-iterative frequency-domain method, to compute the eigenstates of Maxwell's equations in arbitrary periodic dielectric structures, including

systems with anisotropy or magnetic materials [71]. Ben Hiatt presented an efficient finite element method (FEM) for computing spectra of photonic band gap materials [72]. The FEM divides the problem domain into piecewise polynomial functions. This computation has the disadvantages of being expensive in time and memory. Botten proposed the Rayleigh multipole methods for photonic crystal calculations [73]. They provided highly accurate and efficient computational methods due to their use of rapidly convergent field expansions adapted to the particular geometry. Multipole methods have been proved to be superior to plane wave and other numerical techniques in both speed and accuracy.

The integrated CAD tool produced by the Rsoft Design Group, Inc. includes BandSOLVE, FullWAVE, and other photonic simulation tools [74]. BandSOLVE is based on the plane-wave expansion technique for generating and analyzing photonic band structures and can be applied to find the time-independent modes of any lossless photonic structure. FullWAVE is a simulation engine based on the FDTD technique which calculates the electromagnetic field as a function of time and space in a given index structure in response to a given electromagnetic excitation. We will use these simulation tools produced by Rsoft and the programs developed by ourselves to analyze the problems in this study.

Chapter 3

Transmission Improvement in a Photonic Crystal Waveguide

Bend by Mode Matching Technique

3.1 Introduction

PC waveguides provide a powerful way to manipulate and control the flow of electromagnetic waves. High transmission of light through sharp bends in PC waveguides has been demonstrated [26]. A 60° photonic band gap (PBG) waveguide bend which has near 100% efficiency at $\lambda = 1.55 \mu\text{m}$ was observed [75]. A tapered structure which is incorporated into a 60° PC bend for adiabatic mode transformation demonstrated a 90% transmission [76]. By decreasing the size of holes in the immediate vicinity of the bend, the guided mode of the bend can be shifted in frequency to that of a straight waveguide that allows the light of PC waveguides with very low group velocities to be guided around corners [77]. Transmission spectra of a nonresonant PC bend and a cavity-resonant PC bend were measured [78]. The cavity-resonant bend was shown to have a narrow-band transmission with a low insertion loss. However, flat dispersion of defect modes results in a very narrow guiding bandwidth. Thus, there have been many bend structures proposed for bandwidth improvement [79]. By making the waveguide become single mode at the PC bend, the bandwidth of transmission can be improved [80]. Significant performance improvements of PC waveguide bends have been numerically and experimentally demonstrated by the topology optimization [81], [82].

The periodicity of the PC waveguide gives rise to mode gaps between different guided modes. Such mode gaps make it possible to create bound states in a waveguide

with a constriction and in bends. Bound states in PBG bends closely correspond to cavity modes [83]. In next section, the cavity mode of a PC waveguide bend and the guided mode of a PC straight waveguide are analyzed. An approach for improving the transmission efficiency of PC waveguide bends through maximization of the overlap integral of fields between the straight waveguide and the waveguide bend is presented.

In the following paragraphs, the mode matching technique for highly efficient transmission in a 60° PC waveguide bend will be presented. By shifting the lattice points around a waveguide bend, the transmission of a 120° PC waveguide bend can also be significantly improved. Finally, the transmission spectrum of this offset PC waveguide bend will be discussed. The numerical simulations are calculated by the 2D FDTD method. Perfectly matched layers are applied to the four sides of the computational domain to delimit the boundary.

3.2 Transmission Improvement in a PC Waveguide Bend by Mode Matching Technique

The radiation losses due to the scattering at the index discontinuities along the waveguide can be significantly reduced by the mode matching technique [84]. The overlap integral is the inner product of two wave functions over space and mode matching can be evaluated from the overlap integral of modes. Offset is one kind of mode matching technique used at the waveguide junctions within the bend to minimize the transmission loss. The mechanism is that the relatively low refractive-index region outside the corner operates as a phase-front accelerator of the propagating mode.

We will show that the transmission of a 2D PC waveguide bend can also be improved by the position offset of lattice points around the bend corner. The wave transmitted through a conventional 60° PC waveguide bend simulated by the FDTD

method is shown in Fig. 3.1(a). The PC structure is a hexagonal array of air holes perforated on the matrix with refractive index $n = 3.44$. The ratio of the radius of air holes over the lattice constant (r/a) is 0.33. The normalized field profiles of the guided modes in the straight waveguide (black line) and in the bend (gray line) at the normalized frequency $f = 0.2350$ (a/λ) are shown in Fig. 3.1(b), respectively. The reference plane of the straight waveguide is a plane cross the waveguide within a unit cell. The reference plane in the bend is a plane along the Γ -K direction. The field profiles are taken at the same time while in the steady state. The intensities of fields are normalized. The overlap integral of these two normalized fields is 0.76. These two fields do not fully match; therefore, the transmission through this PC waveguide bend is only 72.7%.

Bent waveguides can be viewed as one finite and two semi-infinite waveguide sections joined together. Guided modes exist in these two semi-infinite sections and bound states exist in the bend section. The transmission of a PC waveguide bend can be improved by mode matching between the bound states in the waveguide bends and the guided modes in the straight waveguides. Shift of lattice points is used to design and fabricate the smallest PC laser reported to date, and can also provide the mode matching in PCs [85]-[87]. The distance between the two peaks of fields in Fig. 3.1(b) is about $0.2a$. If the lattice points around the bend corner are shifted $0.2a$ along the Γ -K direction indicated by the arrow like Fig. 3.1(c), the normalized field profile in the straight waveguide (black line) and in the bend after adjustment (gray line) are shown in Fig. 3.1(d). The overlap integral of these two fields is increased to 0.92 and the transmission of this PC waveguide bend is improved to 87.5% due to mode matching. Relatively high refractive-index region exists just outside the bend corner after shifting air holes; therefore, the mechanism of transmission improvement in a PC waveguide bend by shifting the lattice points is different from that of a phase-front accelerator.

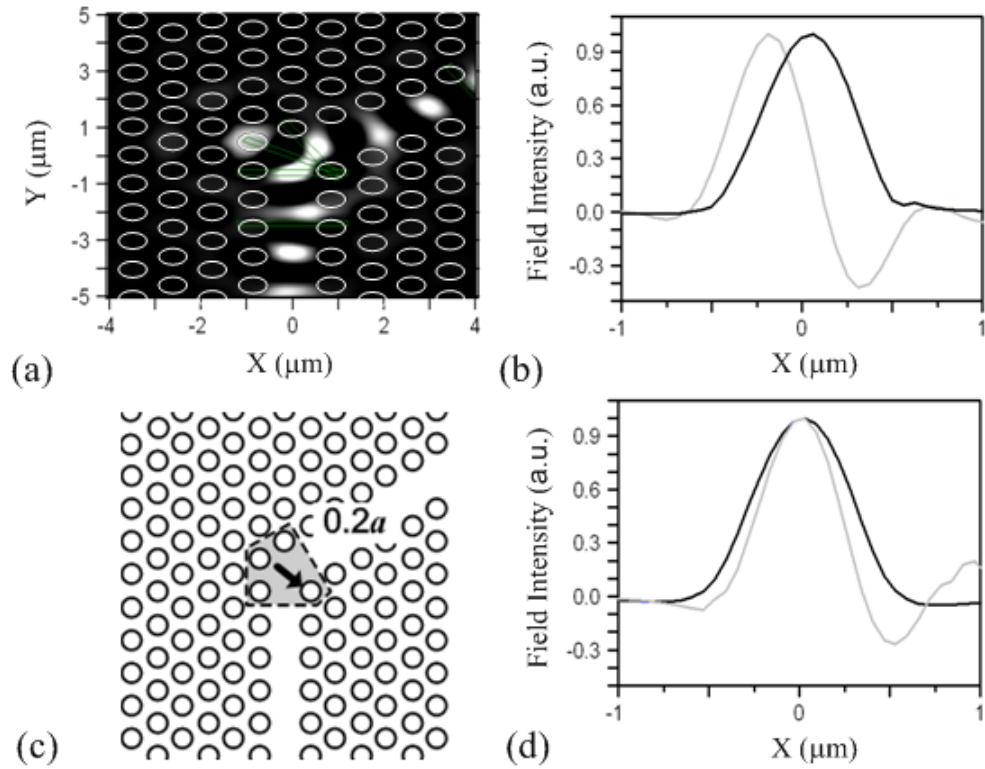


Fig. 3.1: (a) Wave transmitted through a conventional 60° photonic crystal waveguide bend at $f = 0.2350 (a/\lambda)$. (b) Field profiles in the straight waveguide (black line) and in the bend without offset (gray line). (c) Lattice points around the bend corner. The lattice points are shifted $0.2a$ along the Γ -K direction indicated by the arrow. (d) Field profiles in the straight waveguide (black line) and in the bend with offset $0.2a$ (gray line).

The mode matching technique can also be used to design a high efficient 120° PC waveguide bend. The propagation of wave with $f = 0.2350 (a/\lambda)$ in the 120° PC waveguide bend constructed by the material same as that in Fig. 3.1 is shown in Fig. 3.2(a). Most of the power of light is reflected backward from the bend corner; therefore, the transmission is only 5.7%. The bent region of the 120° PC waveguide bend is equivalent to a cavity with three missing holes and the cavity field image determined at the resonant frequency through Fourier analysis is shown in Fig. 3.2(b). It can be seen that the cavity mode does not match the guided mode in the straight waveguide. The

directions for 60° or 120° are the same in a PC structure with a hexagonal array of lattices. Therefore, if the lattice points around the bend corner are shifted $0.2a$ along the Γ -K direction indicated by the arrow like Fig. 3.2(c), the transmission of this 120° PC waveguide bend with offset is dramatically improved from 5.7% to 87.5%. The propagation of wave in this 120° PC waveguide bend with offset and the field image of the three-missing-hole cavity with offset are shown in Fig. 3.2(d) and Fig. 3.2(e), respectively. The field profiles in the straight waveguide (black line), in the three-missing-hole cavity without offset (gray line), and in the three-missing-hole cavity with offset (gray dashed line) are shown in Fig. 3.2(f). The reference plane of the cavity mode is a plane along the x-direction near the center of cavity. Obviously, it can be seen that the transmission improvement of this PC waveguide bend with offset is caused by mode matching.

The transmission spectra of the straight PC waveguide, the 120° PC waveguide bend without offset, and the 120° PC waveguide bend with $0.2a$ offset calculated by the Fast Fourier Transform (FFT) are shown in Fig. 3.3(a). We can see that the transmission of the straight waveguide is high within the PBG range from 0.216 to 0.307 (a/λ). On the other hand, the PC waveguide bends show a narrow band transmission. Point **a** in Fig. 3.3(a) is the low transmission point of the 120° PC bend without offset at $f = 0.2350$ (a/λ) and its transmission is only 5.7%, corresponding to Fig. 3.2(a). Point **b** in the figure is the high transmission point of the 120° PC waveguide bend with offset $0.2a$ at $f = 0.2350$ (a/λ) and its value is improved to 87.5%, corresponding to Fig. 3.2(d). Point **c** is a high transmission point of the 120° PC bend without offset at $f = 0.2315$ (a/λ). Frequency-shift of the spectra for a PC waveguide bend due to this lattice shifting is observed. The field image in the cavity without offset at $f = 0.2315$ (a/λ) as shown in Fig. 3.3(b). Why the transmission at point **c** is high can be seen from Fig. 3.3(c). The field profiles in the straight waveguide (black line), and in the three-missing-hole cavity

without offset (gray line) at $f = 0.2315$ (a/λ) are well matched. These cases show that the transmission of a sharp PC waveguide bend can be significantly improved if the modes of the bound state in the waveguide bend and the guided mode in the straight waveguide can be matched.

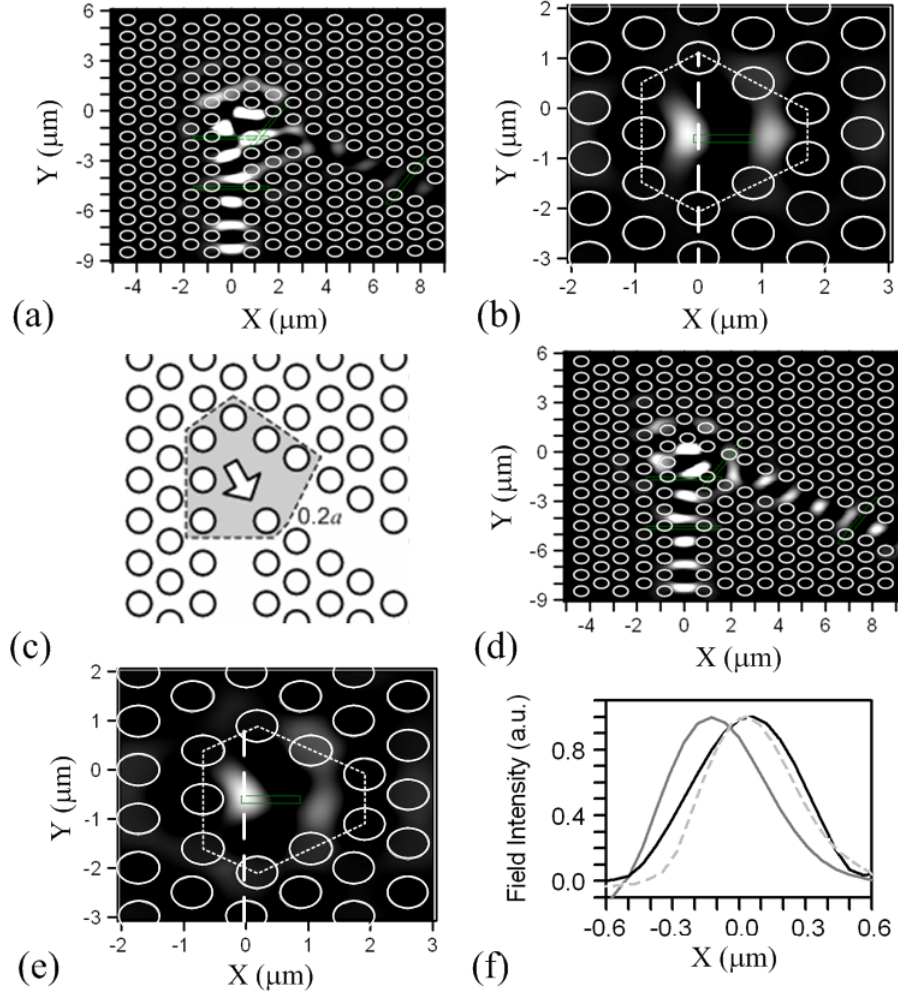


Fig. 3.2: (a) Wave propagation in a conventional 120° photonic crystal waveguide bend at $f = 0.2350$ (a/λ). (b) Field image in a cavity with three missing holes. (c) Lattice points around the bend corner. The lattice points around the bend corner are shifted $0.2a$ along the Γ -K direction indicated by the arrow. (d) Propagation of wave in the 120° PC waveguide bend with offset. (e) Field image in a three-missing-hole cavity with offset. The first annulus of lattice points around the cavity are shifted $0.2a$ along the Γ -K direction. (f) Field profiles in the straight waveguides corresponding to (a) and (d) (black line), in the three-missing-hole cavity without offset corresponding to (b) (gray line), and in the three-missing-hole cavity with offset corresponding to (e) (gray dashed line).

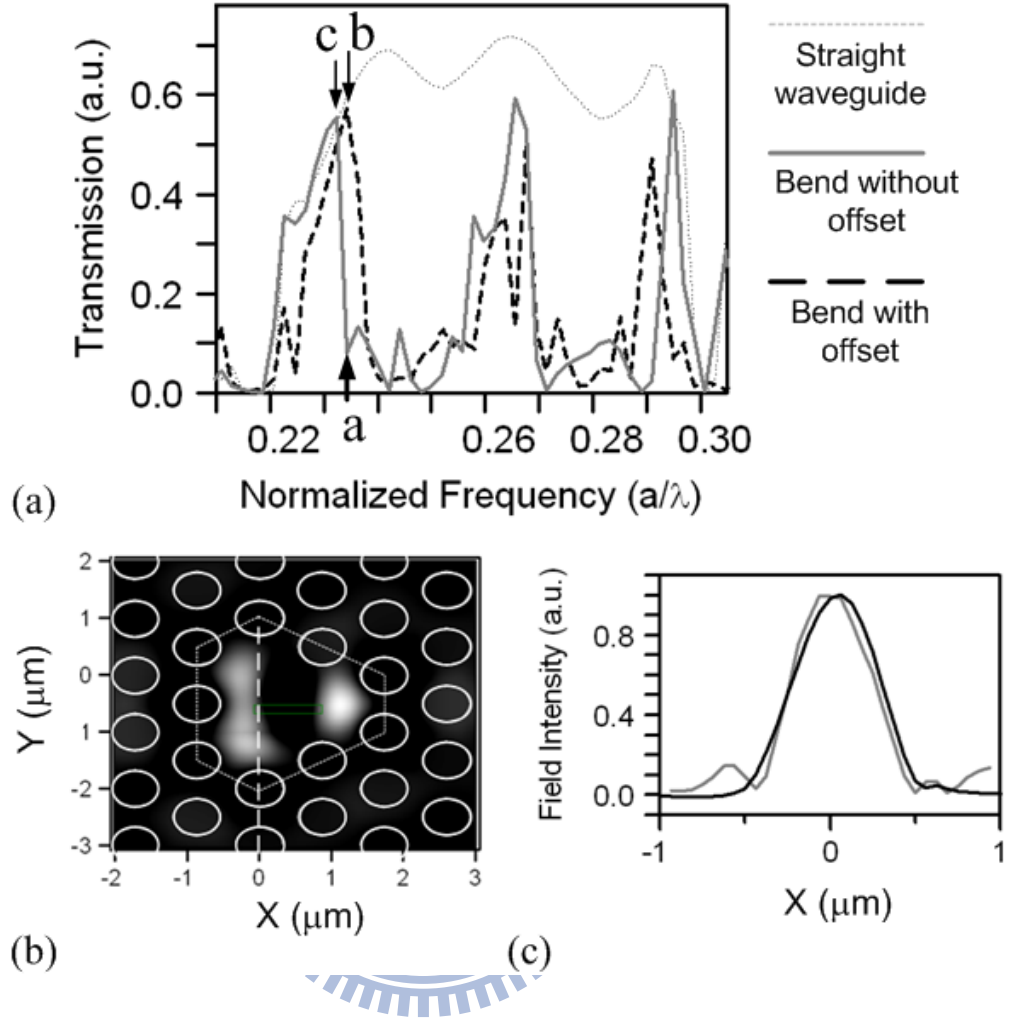
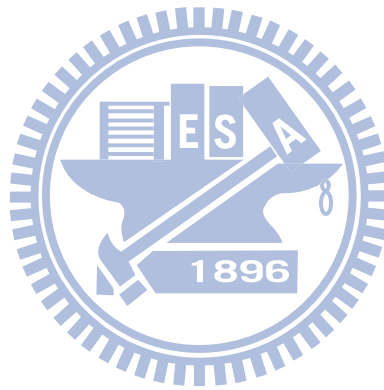


Fig. 3.3: (a) Transmission spectra of the straight PC waveguide, the 120° PC waveguide bend without offset, and the 120° PC waveguide bend with offset $0.2a$. Point **a** is the low transmission point of the 120° PC bend without offset at $f = 0.2350$ (a/λ). Point **b** is the high transmission point of the 120° PC waveguide bend with offset $0.2a$ at $f = 0.2350$ (a/λ). Point **c** is a high transmission point of the 120° PC bend without offset at $f = 0.2315$ (a/λ). (b) Field image in the three-missing-hole cavity without offset at $f = 0.2315$ (a/λ). (c) Field profiles in the straight waveguide (black line), and in the three-missing-hole cavity without offset (gray line) at $f = 0.2315$ (a/λ).

3.3 Summary

We have shown that a high efficient photonic crystal waveguide bend can be designed by mode matching technique. By shifting lattice points around the bend corner,

the bound state in the waveguide bend and the guided mode in the straight waveguide can be matched. In this study, the transmissions of the 60° and 120° PC waveguide bend with mode matching are improved from 72.7% to 87.5% and from 5.7% to 87.5%, respectively. The bound state in a waveguide bend is similar to a cavity mode; therefore, the PC waveguide bend performs a narrow-band transmission. Frequency-shift of the spectra for a PC waveguide bend due to this lattice shifting is observed.



Chapter 4

Design of a Photonic Crystal Tapered Coupler Based on Multimode Interference and Mode Matching

4.1 Introduction

To maintain the features of single-mode and PBGs, the core sizes of PC waveguides must be less than one micron. On the contrary, single-mode fibers or other integrated optic devices have sizes on the order of a few microns. Due to the mismatch of core sizes, the coupling losses between PC waveguides and optical fibers that have been verified and reported are on the order of 20-30 dB. Consequently, coupling between PC waveguides and other optical devices becomes a serious problem.

The measurements and further applications of PC devices are also restricted by the coupling issues. Thus, there have been many couplers proposed for efficient transmission. Compact mode converters with low coupling loss, including gratings, lens or mirrors, and tapered structures are now becoming key building blocks in integrated PC systems. The tapered coupler is the most popular device in connecting PC waveguides with other optical devices. The waveguide taper was used for efficient light coupling between dielectric and PC waveguides [88]. As a result of resonant tunneling in an adiabatic coupling, the transmission coefficient of a tapered slab waveguide at resonant frequencies was high [89]. A mathematical model derived from the step theory was proposed to calculate the transmission efficiency of waveguide tapers [90]. A slow and continuous transition is required in conventional tapered structures; thus, these types of couplers are very long [91]. On the other hand, the size of a PC tapered coupler can be much smaller than that of a conventional waveguide taper due to its large dispersion of modes. Various designs for segmented PC tapers were compared and it

was found that in some cases the transmission decreases counterintuitively when the taper length is increased [92]. Mode matching techniques for highly efficient coupling based on setting localized defects in PC tapered waveguides were studied [93]-[95]. Furthermore, PC continuous tapers were designed by varying progressively the radii of air holes for low-loss direct coupling [76], [96].

The highest transmission efficiency of those coupling structures can be greater than 90%. However, the optimal design methodologies of PC tapered couplers are not clear till now. Note that the section lengths in a conventional PC step tapered coupler are the same. To find out what the optimum length of each section in a PC step tapered coupler is and why the transmission decreases counterintuitively when the taper length is increased in some cases, we inspect the multimode interference (MMI) phenomena in multiple-line-defect PC waveguides.

The MMI phenomenon is an observable fact in multimode devices. On the basis of the self-imaging principle, a field profile can be reproduced in single or multiple images at regular intervals along the path of propagation [97]. The MMI effect can be introduced in optical power splitters/combiners, switches, Mach-Zehnder interferometers, and other applications. However, in the field of PCs, only a few researchers focus on this topic. Power splitters based on the MMI effect in PC waveguides have been presented [98], [99]. Wavelength demultiplexers can be realized by the combination of MMI and PCs [100]-[102].

In this chapter, the design of a PC tapered coupler with different section lengths based on the MMI effect and mode matching is proposed. We have found out that the optimal length of each section in a PC step tapered coupler is related to the imaging length of MMI. The mode profiles between two adjacent sections are matched in the well-designed taper coupler and the scattering losses occurring at the corners of abrupt steps can be eliminated. It provides excellent coupling between PC waveguides and

other optical devices. This study also reveals why in some cases the transmission of PC step tapered couplers decreases counterintuitively when the taper length is increased.

In the following sections, the MMI phenomena in 2D PC waveguides will be discussed. The design method of a PC tapered coupler with different section lengths based on the MMI effect and mode matching will be presented. Finally, the validity and robustness of our method will be verified by two test cases.

4.2 MMI in PC Waveguides

To explore the transmission mechanism behind PC tapered couplers, we first investigate the MMI in the PC structure that was utilized in ref. [92] as shown in Fig. 4.1. The PC tapered coupler connects one input ridge waveguide and one output single-line-defect PC waveguide. In this structure, the material of the matrix is GaAs/Al_{0.6}Ga_{0.4}As. The effective indices of the ridge waveguide and the cladding layer are 3.343 and 3.342, respectively; therefore, the wave within the 1.6- μm -wide ridge waveguide is weakly guided. The PC structure is a triangular lattice of air holes with a lattice constant $a = 0.25 \mu\text{m}$ and an air hole radius $r = 0.3a$, which results in a transverse-electric (TE) bandgap only in the frequency range from 0.211 to 0.282 (a/λ). TE polarization indicates that the electric field is perpendicular to the normal of the lattice plane, which follows the convention used in a photonic crystal. The single-line-defect PC waveguide is formed by removing one row of air holes along the Γ -K direction in the triangular lattice and denoted by a W1 PC waveguide. Wn stands for a PC waveguide with n rows of air holes removed. Consequently, the PC tapered coupler is composed of W3, W5, and W7 sections. A Gaussian wave with a wavelength λ of 1 μm is launched from the ridge waveguide to test the transmission efficiency of the PC tapered coupler.

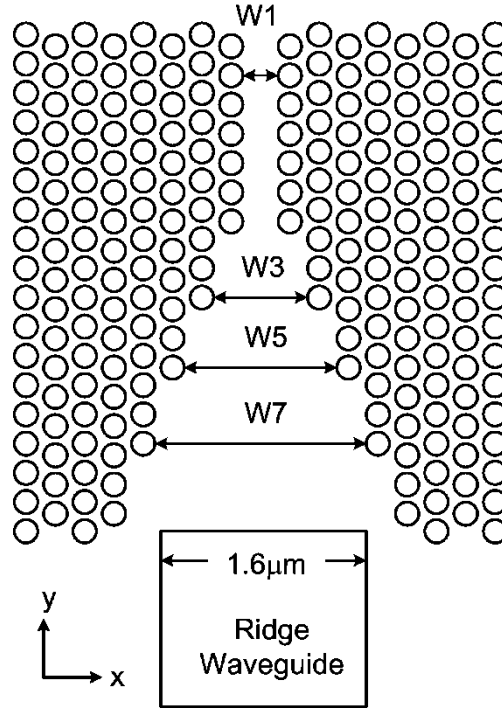


Fig. 4.1: The PC step tapered coupler which connects one input ridge waveguide and one output single-line-defect PC waveguide. The PC structure is a triangular lattice of air holes with a lattice constant $a = 0.25 \mu\text{m}$ and an air hole radius $r = 0.3a$. The effective indices of the ridge waveguide and the cladding layer are 3.343 and 3.342, respectively.

Various lengths of PC tapers shown in Fig. 4.2 are used to compare their transmission abilities from a 1.6- μm -wide ridge waveguide to a single-line-defect PC waveguide. The transmission is calculated by the 2D finite-difference time-domain (FDTD) method. The spatial and temporal grid sizes used in the FDTD method are $a/16$ and $a/64$, respectively. These meet the requirements of the Courant condition [103]; thus, convergent and stable results can be obtained. Perfectly matched layers are applied to the four sides of the computational domain to delimit the boundary. In case (a), the step size in length is two lattices; therefore, the section length of this PC tapered coupler is equivalent to $2.5a$. The transmission through this tapered coupler is 68.9%. For case (b), the section length of each segment is $3.5a$, and its transmission increases to 79.8%.

While in case (c), the length of each section is extended to $4.5a$, but its transmission drops to 55.7%. The transmission decreases counterintuitively when the taper length is increased.

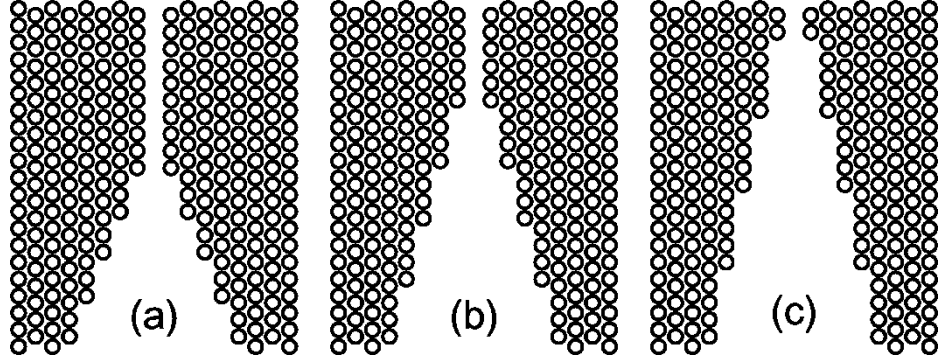


Fig. 4.2: Various lengths of PC tapered couplers used to compare their transmission from a 1.6- μm -wide ridge waveguide to a single-line-defect PC waveguide. The section lengths of each segment in the PC tapered coupler are $2.5a$, $3.5a$, and $4.5a$ in cases (a), (b), and (c), respectively.

First we observe the MMI phenomena in multiple-line-defect PC waveguides to reveal the relation between the optimized section length of a tapered coupler and the imaging length of MMI. In Fig. 4.3(a) and Fig. 4.3(b), a Gaussian light source with a width equal to the waveguide width of W1 is launched from W1 to W3 or from W3 to W1, respectively. It is obvious that self-imaging exists in W3 PC waveguides in both cases. The dual-head arrows in these figures represent the distances between two single images and they come into view at regular intervals with a period equal to $8a$. The first two-fold image appears at $4a$, which is a half of the single-image distance.

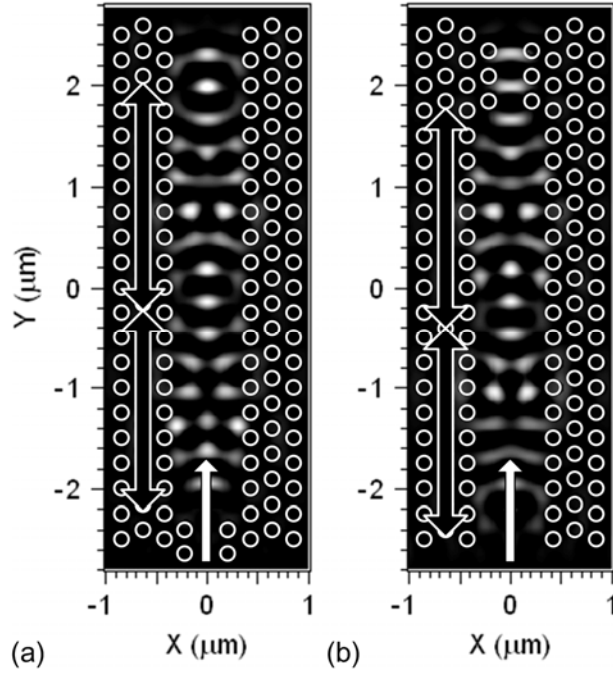


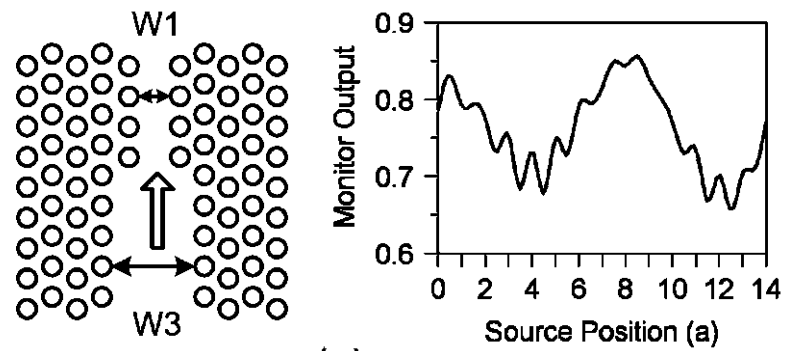
Fig. 4.3: Self-imaging phenomena in multiple-line-defect PC waveguides. The light is launched (a) from W1 to W3, and (b) from W3 to W1. The dual-head arrows represent the distances between two single images.

Next, we show that the transmission between two PC waveguides with different widths is related to the section length of the PC waveguide. In Fig. 4.4, a Gaussian wave with wavelength $\lambda = 1 \mu\text{m}$ propagates from the wider to the narrower PC waveguide. The initial position of the light source located within the wider waveguide is arbitrarily selected away from the interface between two waveguides and then moved toward the interface. The transmission efficiency from the wider to the narrower PC waveguide varies periodically with the position of the light source as shown in these figures. In other words, the transmission is related to the section length of the input waveguide. In case (a), the transmission efficiency from the W3 to the W1 PC waveguide is between 0.65 and 0.86, and its magnitude oscillates in a period of about $8a$. In cases (b) and (c), the transmission efficiencies from W5 to W3 and from W7 to W5 are 0.87~0.94 and 0.90~0.94, respectively. The oscillation period is about $1a$ for both cases. Obviously, there are a larger variation of transmission efficiency and a longer oscillation period in

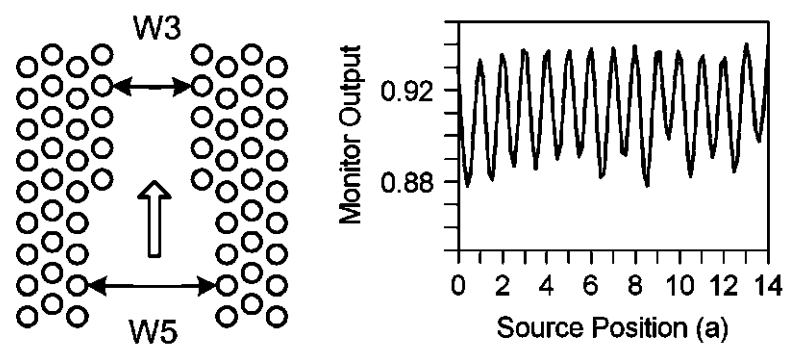
case (a); thus, the section length of W3 in a PC step tapered coupler must be well designed.

The number of modes in a waveguide and the dissimilarity of mode profiles between waveguides affect the efficiency of power conversion. Most of the power loss occurs at the interface of two sections due to the spatial mismatch of waveguides. It has been found that the scattering loss happened mainly at the corners of the abrupt steps [91]. As the waveguide width decreases, so does the number of modes in the waveguide. Since the number of available modes into the PC waveguide falls, the transmission efficiency decreases as well [88]. The W1 waveguide has the fewest modes that can be excited and the narrowest width, which lowers the efficiency of power conversion from W3 to W1.

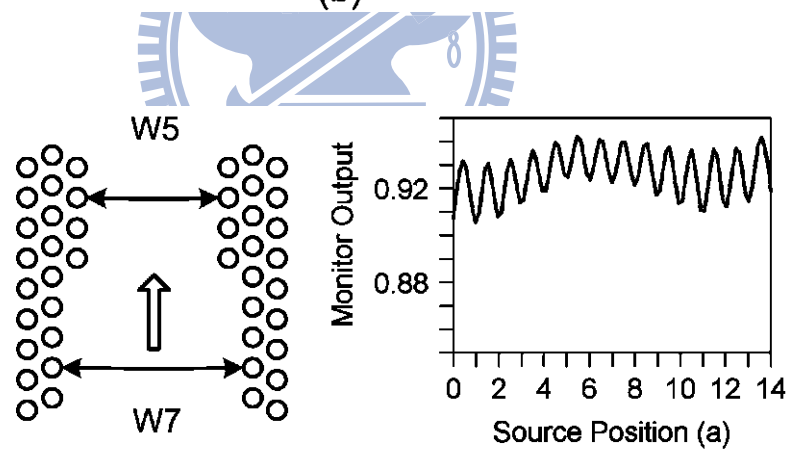
However, the transmission efficiency between two PC waveguides with different widths can be high if the light source is placed at the positions with transmission peaks according to the results in Fig. 4.4. That is equivalent to tuning the section length of the wider waveguide. In Fig. 4.4(a), the magnitude of transmission efficiency from W3 to W1 oscillates with a period of about $8a$, which is the same as the single-image distance of MMI in the W3 waveguides shown in Fig. 4.3. We may conclude that the optimal length of each segment in a PC step tapered coupler is related to the imaging length of MMI. This concept will be evident in the discussion in the next section.



(a)



(b)



(c)

Fig. 4.4: Transmission efficiencies (a) from W3 to W1, (b) from W5 to W3, and (c) from W7 to W5 PC waveguide. A Gaussian wave is launched from the wider to the narrower section to test the transmission between two PC waveguides with different widths. The transmissions vary periodically with the launch position of the light source.

4.3 Design of a PC Tapered Coupler with Different Section Lengths Based on MMI and Mode Matching

As discussed before, the major transmission loss occurs due to the mismatch of mode images between the contiguous sections and the section length of W3 in a PC tapered coupler is the key parameter to be determined. Let us examine the mode profile in each section. Fig. 4.5(a) shows the projected band diagram of the single-line-defect PC waveguide calculated by the PWE method. The gray regions in the band diagram are zones where PC guided modes exist [104]. Those below the first gray region are index guiding modes, and they fold back into the first Brillouin zone at the zone boundary. The white region between two gray zones is the photonic bandgap. For line-defect PC waveguides, PC guiding modes exist in the PBG. The field profile of the fundamental defect mode in the W1 PC waveguide shown in Fig. 4.5(b) is obviously an even mode.

Fig. 4.5(c) shows the projected band diagram of the W3 PC waveguide. Modes e1 and e2 are purely index-guided because there is no bandgap opened at the zone boundary for these modes. Modes e3, e4, and e5 situated in the bandgap are PBG guiding modes. These modes in the wide defect region of the waveguide lead to the operation of MMI. The working frequency a/λ is equal to 0.25 and it can be seen that there are three modes at that frequency. The propagation constants of the fundamental and second-order modes are 0.42 and 0.28, respectively. The single-image distance of MMI is approximately $2\pi/(k_0 - k_2) = 7.14a$, where k_0 and k_2 are the wave numbers of these two modes [98]. Because the PWE method cannot be used to treat problems with loss and dispersion, it should be emphasized that the results evaluated from this band diagram have a large deviation. By using the FDTD method, the distance between two single images can be precisely obtained and is equal to $7.8a$. The first two-fold image appears at $3.9a$.

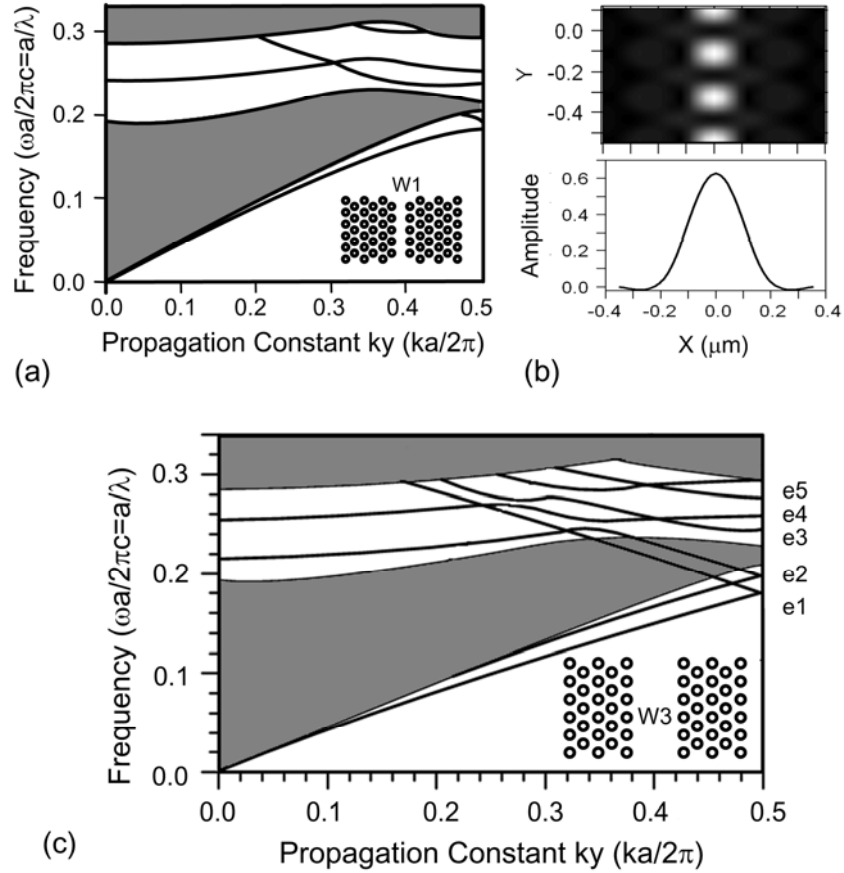


Fig. 4.5: (a) Projected band diagram of the single-line-defect PC waveguide. (b) Field profile of the fundamental mode in the W1 PC waveguide. (c) Projected band diagram of the W3 PC waveguide.

If the section length of W3 is adjusted to $3.9a$, the wave can be coupled smoothly from the W3 to the W1 PC waveguide by mode matching. The section length of W3 in a PC step tapered coupler can be fine-tuned from $3.5a$ to $3.9a$ by adjusting the positions of the first two air holes of the W1 waveguide as shown in Fig. 4.6. Therefore, a PC step tapered coupler with different section lengths can be constructed.

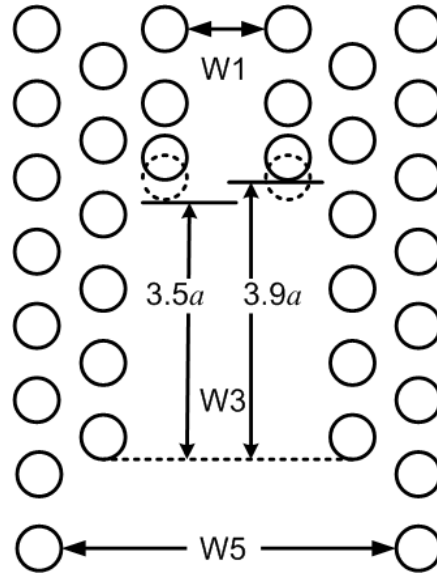


Fig. 4.6: The section length of W3 in a PC step tapered coupler can be fine-tuned from $3.5a$ to $3.9a$ by adjusting the positions of the first two air holes of the W1 waveguide.

Therefore, the section length of W3 of the tapered structure in Fig. 4.2(a) was fine-tuned from $2.5a$ to $3.9a$. The MMI phenomenon in the well-designed PC tapered coupler is shown in Fig. 4.7(a). Whereas the section length of W3 was changed from $2.5a$ to $3.9a$, the transmission efficiency of this tapered coupler was markedly improved from 68.9 to 87.4%. The improvement is mainly due to the mode matching between the W3 and W1 PC waveguides. The transmission is 83.1% when the section length of W3 is $3.5a$, and it drops to 73.5% when the section length of W3 is extended to $4.5a$. The power profiles in the W1 PC waveguide and at the entrance of the W3 section are shown in Fig. 4.7(b) and Fig. 4.7(c), respectively. The wave of a two-fold image at the entrance of the W3 section can couple smoothly into the W1 PC waveguide, which supports the single mode only through one two-fold-image distance. While the section length of W3 is elongated out of the range of two-fold-image distance, the modes are no longer well matched and the wave will not be coupled smoothly from the W3 to the W1 PC waveguide. The mode conversion is reduced when the section length of a PC step

tapered coupler is out of the imaging length of MMI. Therefore, the transmission of a PC step tapered coupler varies periodically with the section lengths. This explains why the transmission decreases counterintuitively in some cases when the taper length is increased. The transmission of a PC step tapered coupler does not increase as the taper length increases, which is different from the case of a conventional waveguide taper. In a conventional waveguide taper, a long taper length is required for an adiabatic mode conversion. The transmission spectrum as a function of the operating wavelength of the well-designed PC tapered coupler is shown in Fig. 4.7(d). It can be seen that the device has a broadband transmission characteristic. Compared with those structures in which high transmissions are achieved using interface resonant modes, whose bandwidths are limited by the resonance width [88], in our design the PC tapered coupler with different section lengths gives a nonresonant way of coupling; the device can have a wider frequency range for high transmission.

The validity and robustness of our method are demonstrated by two test cases. The structure of the first test case shown in Fig. 4.8 is the same as that of the case in Fig. 4.2(a) except that the section length of W3 in the PC tapered coupler is adjusted from $2.5a$ to $11.7a$, which is the length of one two-fold-image distance plus one single-image distance. The transmission efficiency of this tapered coupler is improved from 68.9 to 82.9%, which is slightly smaller than the best one in Fig. 4.7(a) but is still greater than the nonoptimized case. Transmission improvement by introducing the concept of the imaging length of MMI to design a PC tapered coupler was affirmed by this test case.

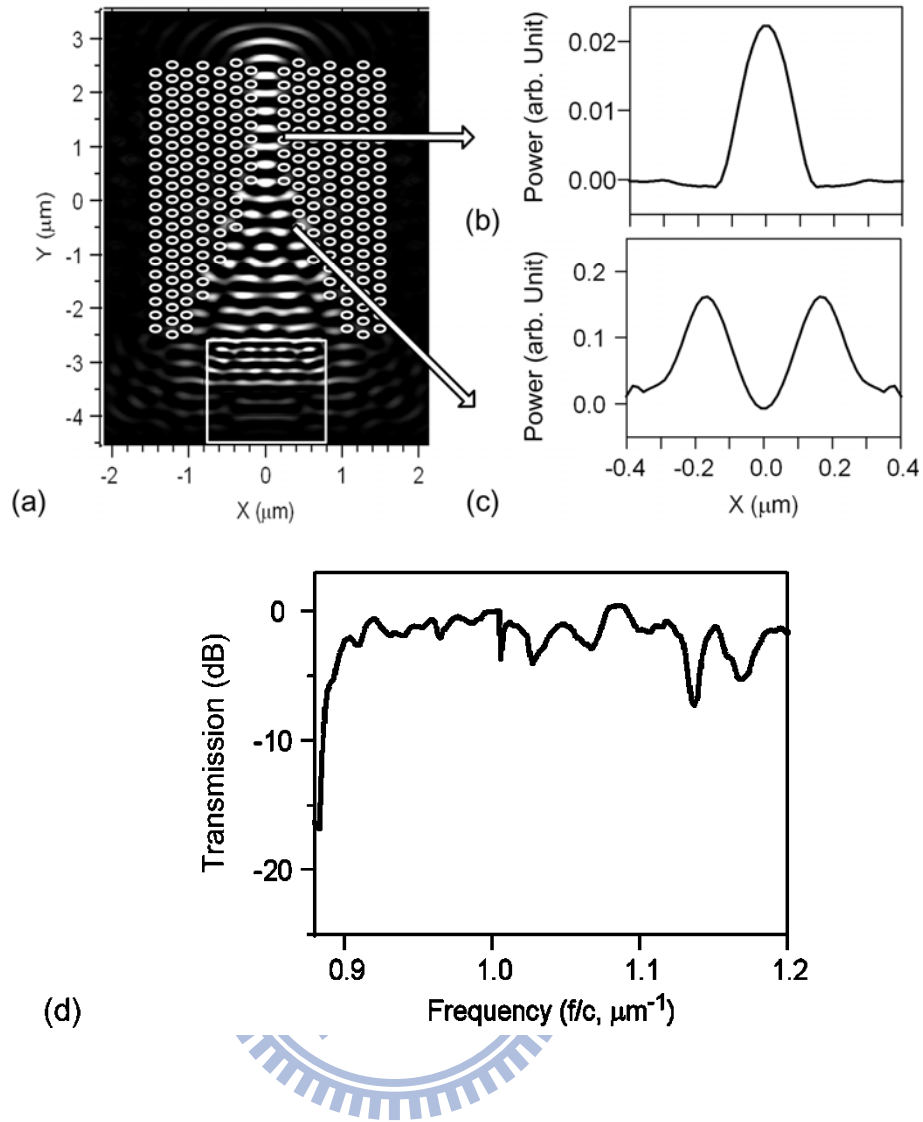


Fig. 4.7: (a) MMI phenomenon in the well-designed PC tapered coupler with different section lengths. The tapered structure is the same as the case in Fig. 4.2(a) except that the section length of W3 is fine-tuned from $2.5a$ to $3.9a$. (b) Power profile of a single image in the W1 PC waveguide. (c) Power profile of two-fold image at the entrance of the W3 PC waveguide. (d) Transmission spectrum of the well-designed PC tapered coupler as a function of the operating wavelength.

Coupling efficiencies can also be improved by changing the radii of air holes in PC couplers, but the corresponding design methodologies are difficult to perform [105]. In the second test case, the correlation between the radii of air holes and the coupling efficiency of tapered couplers will be discussed. The structure of the second test case is the same as that of the case in Fig. 4.2(a) except that the section length of W3 is $3.5a$.

As shown in Fig. 4.9(a), the original radius of the first two air holes of the W1 waveguide is $0.3a$ (the dashed line circles) and we regulate it to see the variation of transmission. The transmission of the PC tapered coupler as a function of the radius of the first two air holes of the W1 waveguide is shown in Fig. 4.9(b). When the radius of the modified air holes is reduced to $0.16a$ (the solid line circles), the transmission reaches its maximum, i.e., 85.1%. The efficiency improvement is partially from the expansion of the waveguide width. However, note that the section length of W3 after fine tuning is equivalent to $3.84a$, which is almost the same as the single-image distance of MMI, i.e., $3.9a$. Altering the radius of the first two air holes in the W1 waveguide is equivalent to modifying the section length of W3. As a result of mode matching between the two neighboring sections, the transmission of this PC tapered coupler can be improved. This explains why we can achieve high coupling efficiency by adjusting the radii of air holes in PC segmented taper couplers.

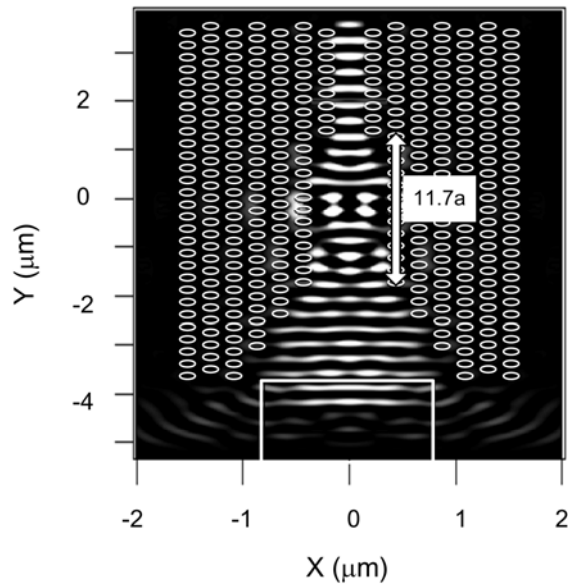
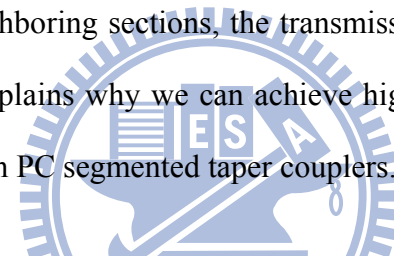


Fig. 4.8: The tapered structure of the first test case. It is the same as that of the case in Fig. 4.2(a) except that the section length of W3 is adjusted from $2.5a$ to $11.7a$, which is the length of one two-fold-image distance plus one single-image distance.

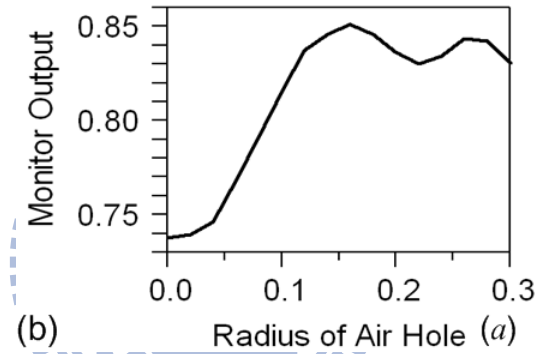
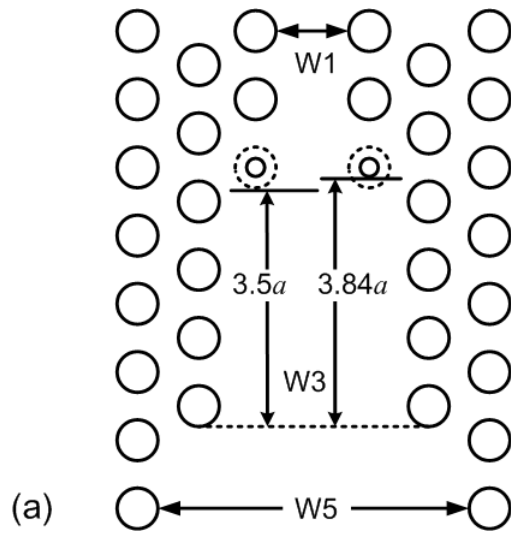
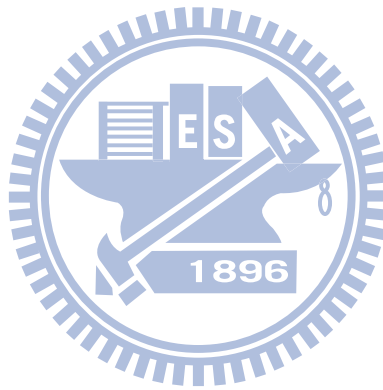


Fig. 4.9: (a) The tapered structure of the second test case. It is the same as that of the case in Fig. 4.2(a) except that the section length of W3 is $3.5a$. The radius of the first two air holes of the W1 waveguide is modified from $0.3a$ (the dashed line circles) to $0.16a$ (the solid line circles). The equivalent section length of W3 after fine tuning is $3.84a$. (b) Transmission as a function of the radius of the first two air holes of the W1 waveguide. The maximum coupling efficiency is 85.1% when the radius of the modified air holes is $0.16a$.

4.4 Summary

PC devices with tapered structures can be easily coupled with other optical elements, such as single-mode optical fibers, slab waveguides, and ridge waveguides. In conventional PC step tapered couplers, the length of each segment is the same and their transmission efficiencies are inhibited. Some researchers concluded that the PC tapers

have to be lengthened to increase their coupling ability. In this study, it is found that the section length in a PC tapered coupler plays a crucial role and is related to the imaging length of MMI. Therefore, a PC step tapered coupler with different section lengths can be designed on the basis of multimode interference. The optimal structure can provide mode matching between two adjacent sections and reduce the scattering loss occurring at the corners of abrupt steps. In the case we studied, when the section length of $W3$ is fine-tuned from $2.5a$ to $3.9a$, the transmission efficiency of this tapered coupler is improved significantly from 68.9 to 87.4%. Thus, the PC step tapered coupler with different section lengths designed on the basis of MMI can provide high transmission efficiency between PC waveguides and other optical devices.



Chapter 5

Ultra Compact Photonic Crystal Polarization Beam Splitter

Based on Multimode Interference

5.1 Introduction

PC devices based on the multimode interference (MMI) effect can be much smaller than conventional MMI devices due to the large dispersion in PC structures [106]. MMI phenomena exist in multimode devices. A field profile can be reproduced in single or multiple images at regular intervals along the path of propagation based on the self-imaging principle [97]. The MMI effect can be used in applications of optical power splitters/combiners, switches, wavelength demultiplexers, Mach-Zehnder interferometers, couplers, etc [107]-[110]. Conventional MMI devices have features such as simple structure, low polarization dependence, low loss, and large optical bandwidth. In the area of PCs, more and more researchers have focused on this topic. PC power splitters, filters, switches, and couplers based on the MMI effect and self-imaging principle have been proposed [111]-[114].

Polarization beam splitters (PBSs) split an unpolarized beam into two beams with orthogonal polarizations. Conventional polarizers can be designed by reflection of the Brewster's angle, birefringent crystals, or thin film technology [115]. PBSs are important components for integrated optoelectronic circuits and can also be realized on PC structures. Design, fabrication, and measurement of a PC polarization splitter made by the autocloning technology have been reported [116], [117]. A two-dimensional (2D) grating coupler was proposed as a polarization splitter [118]. The microwave-scale PBS had been experimentally demonstrated on 2D PCs [119]. A compact PBS based on a PC directional coupler with a triangular lattice of air holes has been designed and simulated

[120]. Its polarization separation functionality is enabled by two different guiding mechanisms: the PBG effect for transverse-electric (TE) light and an index-like effect for transverse-magnetic (TM) light, which makes the two channels of the directional coupler decoupled for TE and tightly coupled for TM light. A PBS and a nonpolarizing beam splitter (NPBS) based on a PC directional coupler that consists of a honeycomb lattice of dielectric pillars in air have been presented [121]. A resonant-coupling-type PBS based on a PC structure with absolute PBG was proposed [122]. Theoretical and experimental results of PC PBSs that exhibit a large reflection coefficient for TE and a high transmission coefficient for TM polarization have been presented [123], [124]. Besides a prism, grating, directional coupler, and cavity, a PBS can also be realized by the negative refractive property of PC structures. A PBS where TM polarization is refracted in the positive direction while TE component is negatively refracted has been proposed [125].

The length of a conventional PBS designed by the MMI effect could be too long, because conventional MMI waveguides are insensitive to polarizations of waves. Maybe that is why, to our knowledge, no one has yet designed a PC PBS using the MMI effect. Dispersions of two polarization states in a PC structure are different; therefore, the PC PBS based on the MMI effect should be much smaller than a conventional one. In this study, we will present that the device size of a PC PBS designed by the self-imaging principle is not compact enough. Thus, a PC PBS based on the difference of the interference effect between the TE and TM modes is proposed. Because the band diagram of a dielectric-rod PC structure is simple, to clarify the design concept we investigate the MMI phenomenon on a dielectric-rod PC structure. First, the parameters of guided modes are extracted from the band diagrams calculated by the plane wave expansion (PWE) method. Modal propagation analysis (MPA), as used in conventional multimode devices, is used to predict the image positions [126]. Then the steady-state

field distribution is simulated by the 2D finite-different time-domain (FDTD) method to have the actual image positions. Through these theoretical procedures, an ultra compact PC PBS based on the MMI effect can be designed. The length of the MMI region can be only seven lattice constants.

In the following sections, the self-imaging phenomena in PC multimode waveguides will be investigated. The performance of a PBS with a dielectric-rod PC structure designed by the self-imaging principle will be discussed. Next, a compact PC PBS based on the difference of the interference effect between TE and TM modes will be proposed. Finally, the performance of this compact device will be evaluated.

5.2 Design of an MMI-based PC PBS by Using the Self-imaging Principle

The operation of conventional MMI devices is based on the self-imaging principle. In conventional optical waveguides, approaches that make use of ray optics [127], the beam propagation method (BPM), or the hybrid method [128], [129] are used to predict the image positions within multimode devices. Because the light confinement in a PC waveguide is due to the PBG but not the total internal reflection, self-imaging phenomena in PC waveguides are not the same as those in conventional waveguides. Therefore, the approximated equations and the rules for designing conventional MMI devices cannot be directly applied to those cases in PC waveguides. The MPA method is the most useful tool for describing the self-imaging phenomena in multimode waveguides [126]. Here we use the MPA method to analyze the imaging lengths in PCs.

Assuming that the input wave is continuous and its spatial spectrum of field is narrow enough not to excite the unguided modes, the total input field $\Psi(y,0)$ at $z = 0$ in the multimode region can be decomposed into the guided modes and expressed as

$$\Psi(y,0) = \sum_{n=0}^{p-1} c_n \varphi_n(y), \quad (5.1)$$

where $\varphi_n(y)$ is the modal field distribution, c_n is the field excitation coefficient, p is the number of modes, and the subscript n denotes the order of modes ($n = 0, 1, 2, \dots, p-1$). The field excitation coefficient c_n can be estimated using overlap integrals based on the field-orthogonality relation as

$$c_n = \frac{\int \Psi(y,0) \varphi_n(y) dy}{\int \varphi_n^2(y) dy}, \quad (5.2)$$

Assuming the time dependence implicit hereafter and taking the phase of the fundamental mode as a common factor, the field profile at a distance z can then be written as a superposition of all the guided mode field distributions

$$\Psi(y, z) = \sum_{n=0}^{p-1} c_n \varphi_n(y) \exp[j(\beta_0 - \beta_n)z] \quad (5.3)$$

The profile of $\Psi(y, z)$ and the types of images formed are determined by the modal excitation coefficient c_n , and by the properties of the mode phase factor $\exp[j(\beta_0 - \beta_n)z]$, where β_0 and β_n are the propagation constants of the fundamental mode and the n th mode.

Then, the length of direct images, L_d , satisfies

$$(\beta_0 - \beta_n)L_d = 2p_n\pi, \text{ with } p_n = 1, 2, 3, \dots, \quad (5.4)$$

and we obtain

$$\Psi(y, L_d) = \Psi(y, 0) \quad (5.5)$$

This condition means that the phase changes of all modes after propagating L_d must differ by integer multiples of 2π , and all guided modes interfere with the same relative phases as those at $z = 0$. Thus, the image at a distance L_d is a direct replica of the input field.

On the other hand, the length of mirror images, L_m , satisfies

$$(\beta_0 - \beta_n)L_m = 2q_n\pi \quad \text{for even modes and}$$

$$(\beta_0 - \beta_n)L_m = (2q_n - 1)\pi \quad \text{for odd modes, with } q_n = 1, 2, 3, \dots \quad (5.6)$$

This condition means that the even modes are in phase and the odd modes out of phase after propagating the length of mirror images. In the case of structural symmetry with respect to the plane $y = 0$, we obtain

$$\Psi(-y, L_m) = \Psi(y, 0). \quad (5.7)$$

Thus, the image at a distance L_m is a mirrored replica of the input field.

An MMI coupler can separate two waves with one wave to form a direct image at one output of the coupler and the other wave to form a mirrored image at the other output. This design concept is widely used in conventional beam splitters based on MMI. In the following a PC PBS based on the self-imaging principle, which can separate TE and TM waves will be designed [130]. In this study, the TE polarization indicates that the electric field is perpendicular to the normal of the lattice plane, which follows the convention used in a photonic crystal.

To design a PBS, the first requirement is that both TE and TM light can propagate with low loss in a PC waveguide. There is no TE gap while the refractive index $n < 3.5$ for a square lattice of dielectric rods in air. Therefore, to have a PC structure with a joint bandgap, the PC structure we will discuss is a square lattice of dielectric rods with refractive index 4.1. Germanium with a refractive index of 4.1 is a promising material that is widely used in advanced semiconductor process. That results in the largest joint bandgap at $r = 0.38a$, where r is the radius of dielectric rods and a is the lattice constant of the PC. The band diagram is shown in Fig. 5.1 and the frequency range of the complete bandgap is from 0.455 to 0.475 (a/λ), where λ is the wavelength in free space. However, the lower edge of the bandgap at X point is extended to 0.440 (a/λ). The schematic structure of the PC PBS to be designed is shown in Fig. 5.2. It is basically a 1×2 MMI coupler and has one input access port and two output access ports, Port 1 and

Port 2. A single-line-defect PC waveguide that is formed by removing one row of dielectric rods along the Γ -X direction in the square lattice acts as the access waveguide and is denoted by W1. W_n stands for a PC waveguide with *n* rows of dielectric rods removed.

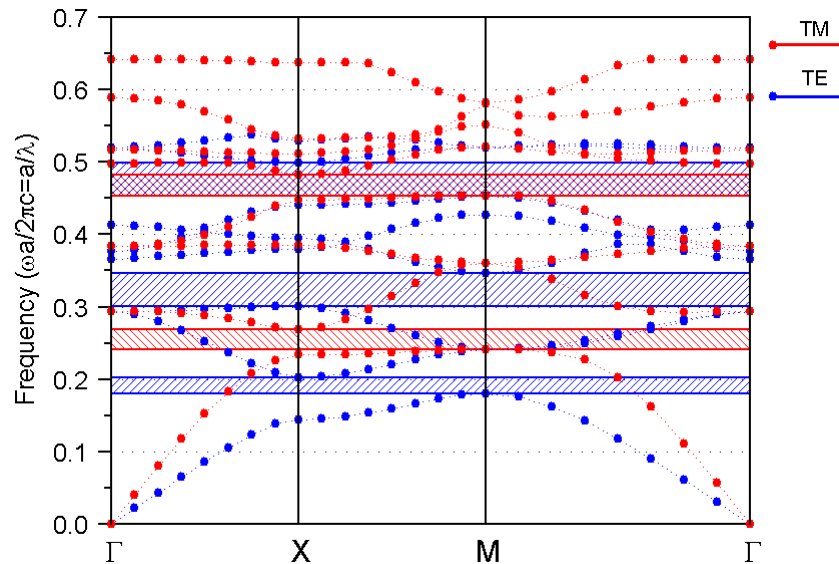


Fig. 5.1: (Color) Band diagram of the PC structure. The PC structure is a square lattice of dielectric rods with refractive index 4.1 and the radius of dielectric rods $r = 0.38a$, where a is the lattice constant of the PC.

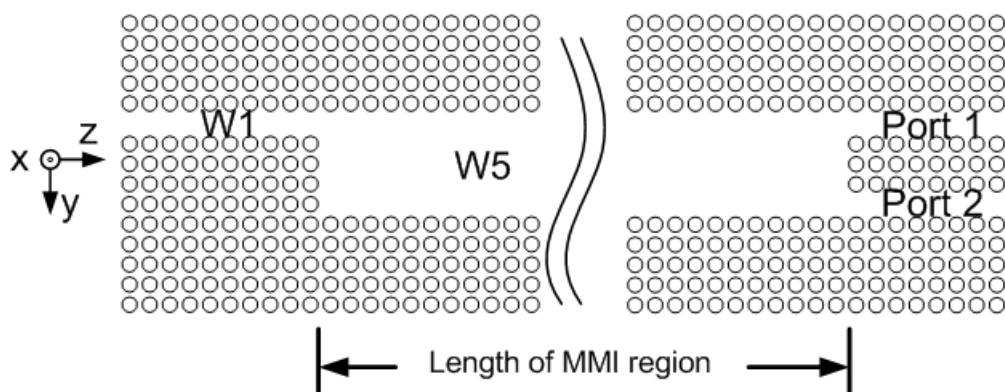


Fig. 5.2: Schematic structure of a PC PBS based on the MMI effect. The 1×2 MMI coupler has one input and two output access ports. W1 PC waveguides act as the access waveguides. A W5 PC waveguide acts as the multimode interference region and its section length is to be designed.

The TE and TM projected band diagram for this W1 PC waveguide calculated by the PWE method with the supercell approximation are shown in Fig. 5.3(a) and Fig. 5.3(b), respectively. It can be seen that this PC waveguide supports two TE defect modes and one TM defect mode within the frequency range of PBG. The 0th TE mode is even and the 1st is odd. The high transmission frequency of this W1 PC waveguide is around 0.444 (a/λ) for TE and TM waves, so 0.444 (a/λ) is chosen as the operating frequency.

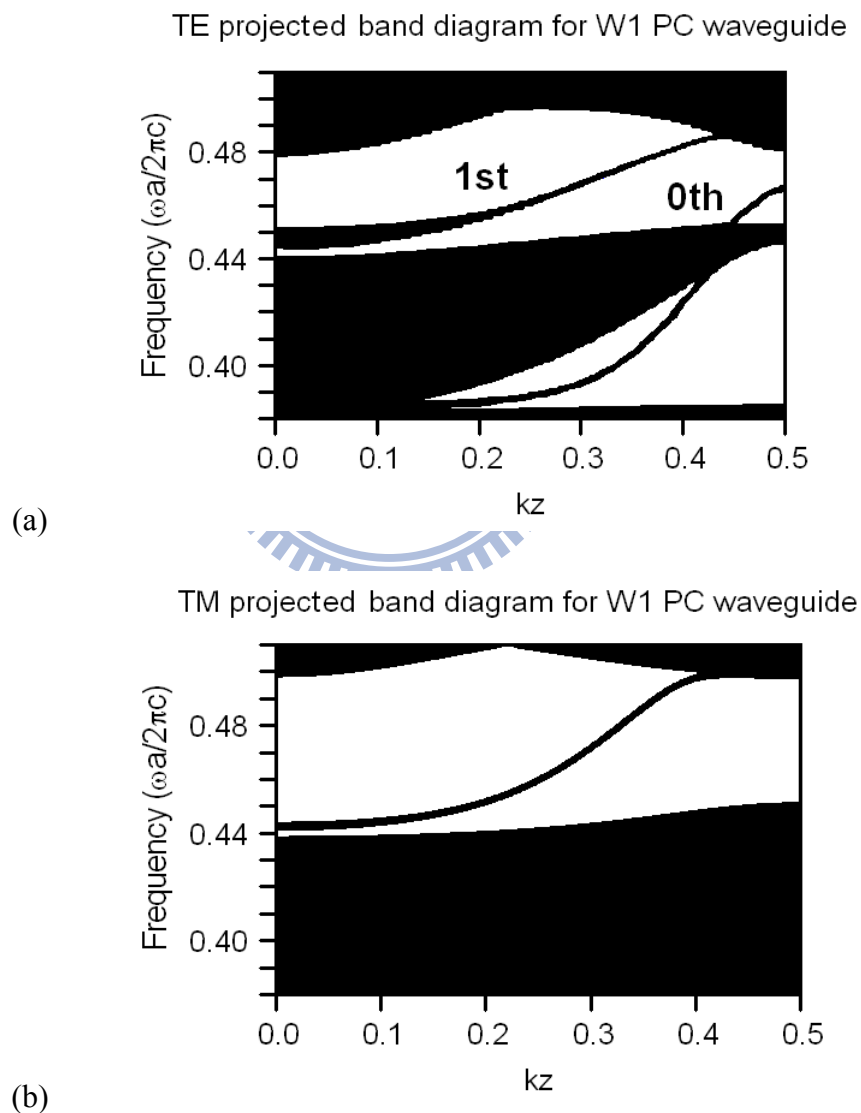


Fig. 5.3: (a) TE and (b) TM projected band diagram of the W1 PC waveguide. This PC waveguide supports two TE defect modes and one TM defect mode.

The W5 PC waveguide acts as the multimode interference region and its length is to be designed. The imaging property of a waveguide is linked to the characteristic of its spectrum of propagation constants. The TE projected band diagram of the W5 PC waveguide simulated by the PWE method is shown in Fig. 5.4. It can be seen that this multimode PC waveguide supports four modes for a TE wave at an operating frequency of $0.444 (a/\lambda)$. These modes in the wide defect region lead to the operation of MMI. The parameters about these modes, including propagation constants and the symmetry property of modal field patterns, are listed in Table 5.1. The coupling length between the fundamental mode and the n th mode is defined as $L_C = \pi/(\beta_0 - \beta_n)$. It can be calculated that the coupling length between the fundamental mode and the first mode is $44a$ and self-imaging exist if all coupling lengths are very nearly the integer multiples of this fundamental difference, as described by Eqs. (5.4)-(5.7). The lengths of direct images L_d and mirror images L_m can be calculated from these parameters by Eqs. (5.4) and (5.6), respectively. Consequently, the first mirror image and the direct image are estimated at $44a$ and $88a$ in this multimode region.

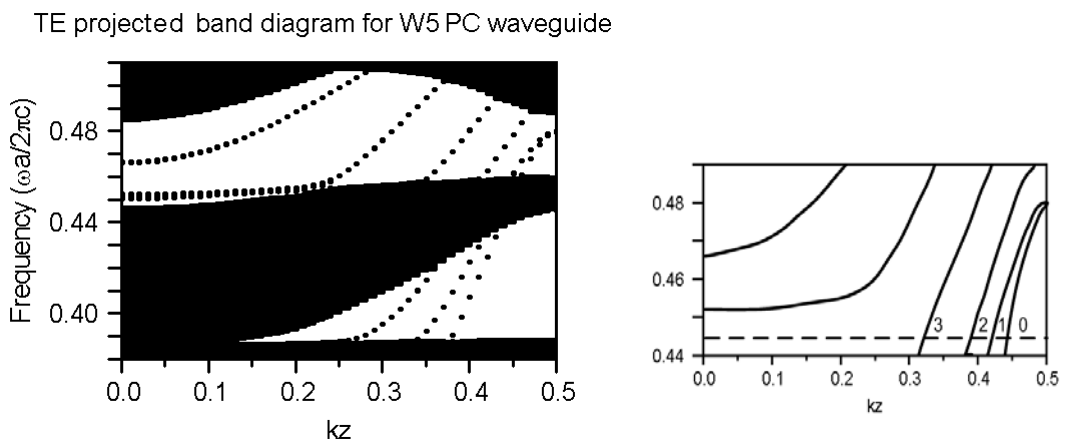


Fig. 5.4: TE projected band diagram of the W5 PC waveguide. This PC multimode waveguide supports four modes at the operating frequency of $0.444 (a/\lambda)$.

Table 5.1: Parameters used to calculate the locations of images of the W5 PC waveguide for a TE wave at 0.444 (a/λ).

Mode no.	Parity	$\beta_n (2\pi/a)$	$L_C = \pi/(\beta_0 - \beta_n)$	First mirror image	First direct image
0	even	0.441	-	-	-
1	odd	0.429	$43a$	$L_C \times 1 = 43a$	$L_C \times 2 = 86a$
2	even	0.395	$11a$	$L_C \times 4 = 44a$	$L_C \times 8 = 88a$
3	odd	0.312	$3.9a$	$L_C \times 11 = 43a$	$L_C \times 22 = 86a$

The TM projected band diagram of this W5 PC waveguide calculated by the PWE method is illustrated in Fig. 5.5. From these dispersion curves, it can be seen that this PC multimode waveguide supports four defect modes for a TM wave at an operating frequency of 0.444 (a/λ). The parameters about these modes are listed in Table 5.2. It is estimated that there is a mirror image at $88a$ in the multimode region for a TM wave. If the length of W5 PC waveguide is designed as $88a$, the TE wave will be a direct image at Port 1 and the TM wave will be a mirror image at Port 2. Consequently, we can use the difference of imaging lengths between two polarizations to design a PBS that can separate TE and TM waves.

Table 5.2: Parameters used to calculate the locations of the mirror image of the W5 PC waveguide for a TM wave at 0.444 (a/λ).

Mode no.	Parity	$\beta_n (2\pi/a)$	$L_C = \pi/(\beta_0 - \beta_n)$	Mirror image
0	even	0.431	-	-
1	odd	0.402	$17.3a$	$L_C \times 5 = 87a$
2	even	0.341	$5.6a$	$L_C \times 16 = 89a$
3	odd	0.243	$2.6a$	$L_C \times 33 = 87a$

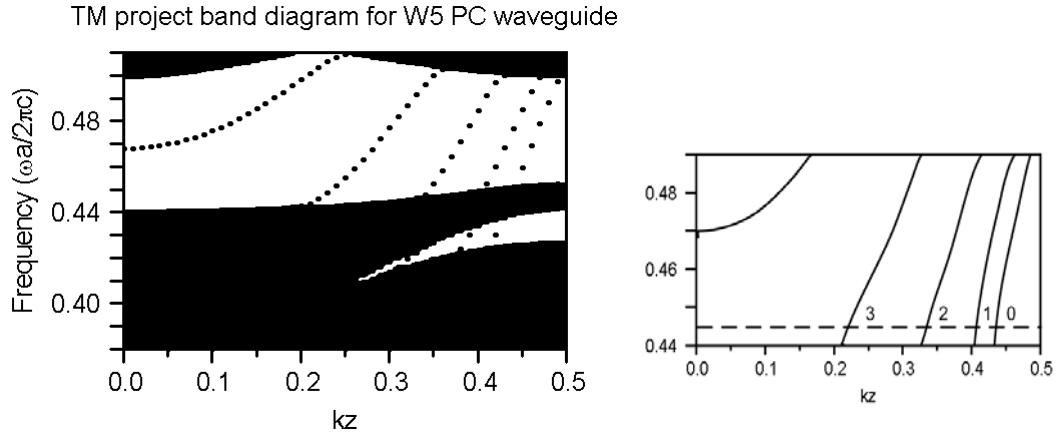


Fig. 5.5: TM projected band diagram of the W5 PC waveguide. This multimode PC waveguide supports four guided modes at the operating frequency of 0.444 (a/λ).

The steady-state electric field distributions of this PC PBS simulated by the 2D FDTD method for TE and TM waves are shown in Figs. 6(a) and 6(b), respectively. The TE wave will be routed to the upper output port (Port 1) and the TM wave to the lower output port (Port 2). The transmissions, bending losses and extinction ratios for two output ports are listed in Table 5.3. Simulation results show that the extinction ratios are 12.8 dB for Port 1 and 9.2 dB for Port 2. The extinction ratio for one output port is defined as the power of desired field to that of the undesired field and is expressed as $10\log(P_{TE(TM)} / P_{TM(TE)})$. The transmissions and the insertion losses are 88.8% and 0.79 dB for the TE wave and 93.3% and 0.30 dB for the TM wave. The insertion loss is the attenuation expressed in decibels for a particular path through the component and is defined as $10\log(P_{port\ 1(2)} / P_{input})$. To avoid the coupling between these two output waveguides, a 90 degree bend is added to the upper output waveguide and the insertion loss of Port 2 includes the bending loss 0.27 dB. Compared to other PC PBSs, the size of this PC PBS designed by the self-imaging principle is not compact enough and we will design a more compact one with a different design consideration.

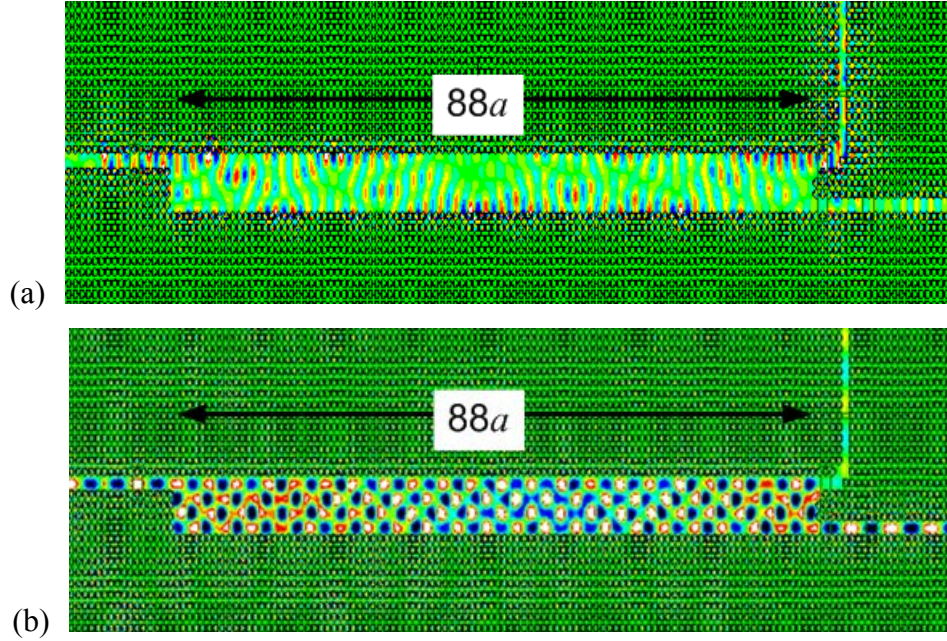


Fig. 5.6: (Color) Steady-state electric field distributions of the PC PBS designed by the self-imaging principle for (a) a TE, and (b) a TM wave.

Table 5.3: Transmissions, extinction ratios and insertion losses of the PC PBS designed by the self-imaging principle.

	MMI Transmission		PBS Extinction Ratio	Insertion Loss
	TE	TM		
Port 1	88.8% (0.52 dB)	4.7% (13.3 dB)	12.8 dB	0.79 dB
Port 2	11.2% (9.51 dB)	93.3% (0.30 dB)	9.2 dB	0.30 dB

5.3 Design of a Compact PC PBS by Difference of Interference between Two Polarizations

The imaging distance for TE polarization is found to be longer than that for TM polarization in conventional MMI devices. This phenomenon may be interpreted as a manifestation of the Goos-Hähnchen effect [127]. In a PC structure, it is also found that the imaging lengths for a TE wave and for a TM wave are different. This phenomenon

can be interpreted by anisotropy of a photonic band structure [116]. It can be seen that there are many high-intensity points, except the self-images in Fig. 5.6(b). In the following, a compact PC PBS will be designed using the high-intensity point instead of the self-imaging principle.

To verify the interference difference between two polarizations, we observe the steady-state field distribution in an open-ended W5 PC waveguide, as shown in Fig. 5.7, by the 2D FDTD method. According to the central line ($y = 0$) of the open-ended W5 PC waveguide, the upper half portion is called Channel 1 and the lower half is called Channel 2. The optical powers within Channel 1 and Channel 2 are measured by Monitors A and B, respectively. Transmissions of a TE wave measured by Monitor A (solid curve) and Monitor B (dashed curve) under different positions within the W5 PC waveguide are shown in Fig. 5.8. The transmission is defined as the ratio of the measured power to the input power. It can be seen that the first peaks of transmission along Channel 2 and Channel 1 happen at $44a$ and $88a$, respectively. That is consistent to the imaging lengths calculated from Table 5.2.

On the other hand, transmissions of a TM wave measured by Monitor A (solid curve) and Monitor B (dashed curve) under different positions within the W5 PC waveguide are shown in Fig. 5.9. Compared with the case of a TE wave, the field distribution due to the interference effect for a TM wave is strongly dependent on the propagation distance in this PC structure. It can be seen that peak values happen alternatively along Channel 1 and Channel 2 with a period of about $9.8a$, and the first peak of the transmission along Channel 2 appears at $6a$.

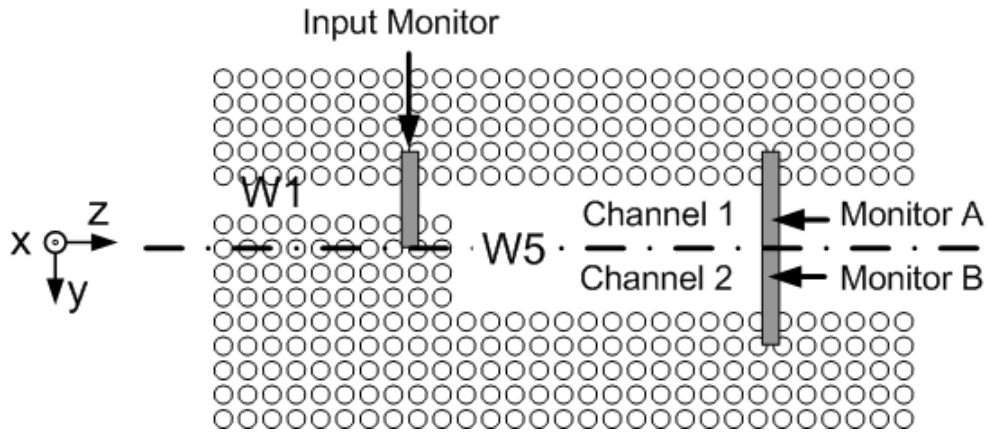


Fig. 5.7: Open-ended W5 PC waveguide to be studied. The optical powers within the upper- (Channel 1) and lower- (Channel 2) half portions of the open-ended W5 PC waveguide are measured by Monitors A and B, respectively.

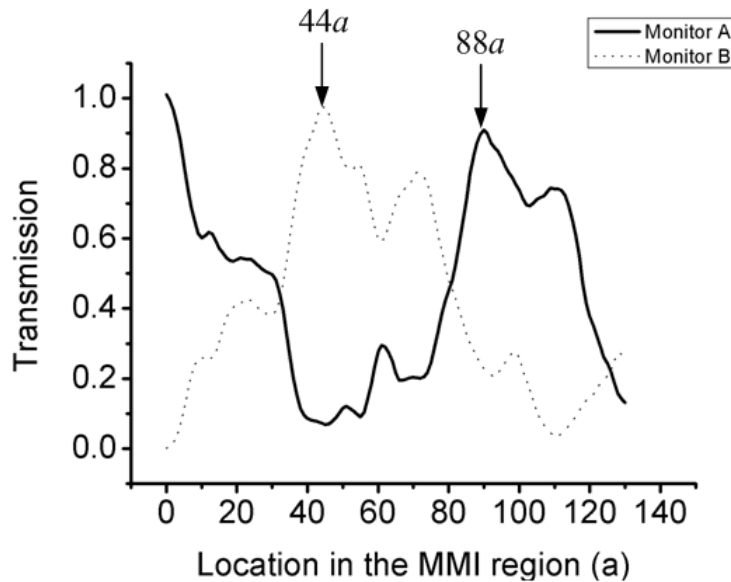


Fig. 5.8: Transmissions of a TE wave measured by Monitor A (solid curve) and Monitor B (dashed curve) under different positions within the W5 PC waveguide. The first peaks of transmission along Channel 2 and Channel 1 happen at about $44a$ and $88a$, respectively.

Next we will use the PWE method to reveal why there is a transmission peak at $6a$ along Channel 2 for a TM wave. The normalized field profiles of the W1 and W5 PC waveguides for the TM mode are shown in Figs. 5.10(a) and 5.10(b), respectively.

These field profiles are taken from the central plane (x - y plane at $z = 0$) of the supercell calculated by the PWE method. Though the field profiles are not uniform along the z -axis within a supercell, they can be approximately represented by the field profile taken from the central plane due to the strong confinement of light within a PBG. The normalized field excitation coefficients calculated from these field profiles by Eq. (5.2) are 0.2452, -0.4797, -0.5740, and 0.6167.

According to Eq. (5.1), the field profile at a distance of z within the W5 PC waveguide can be written as

$$\begin{aligned} \Psi(y, z) &= \sum_{n=0}^3 c_n \varphi_n(y) \exp[j\beta_n z] \\ &= 0.2452 \times \varphi_0 \times \exp[j2\pi \times 0.431z] - 0.4797 \times \varphi_1 \times \exp[j2\pi \times 0.402z] \\ &\quad - 0.5740 \times \varphi_2 \times \exp[j2\pi \times 0.341z] + 0.6167 \times \varphi_3 \times \exp[j2\pi \times 0.213z]. \end{aligned} \quad (5.8)$$

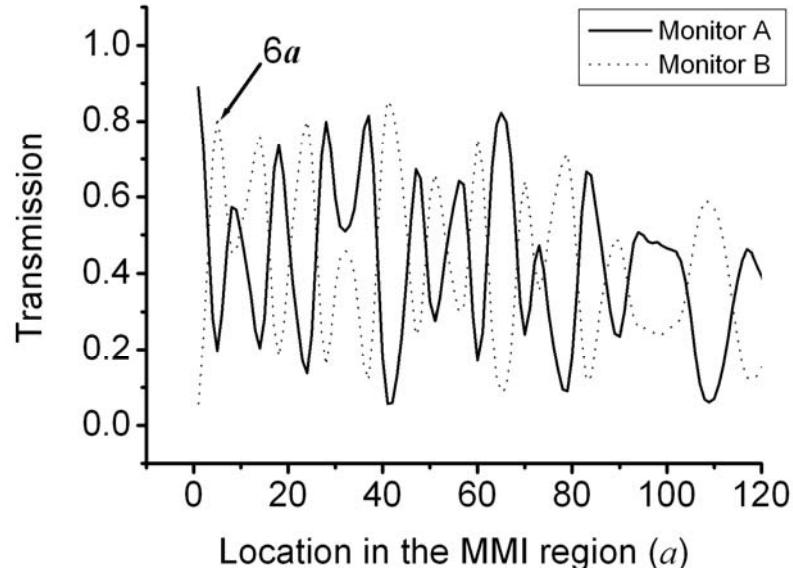


Fig. 5.9: Transmissions of TM wave measured by Monitor A (solid curve) and Monitor B (dashed curve) under different positions within the W5 PC waveguide.

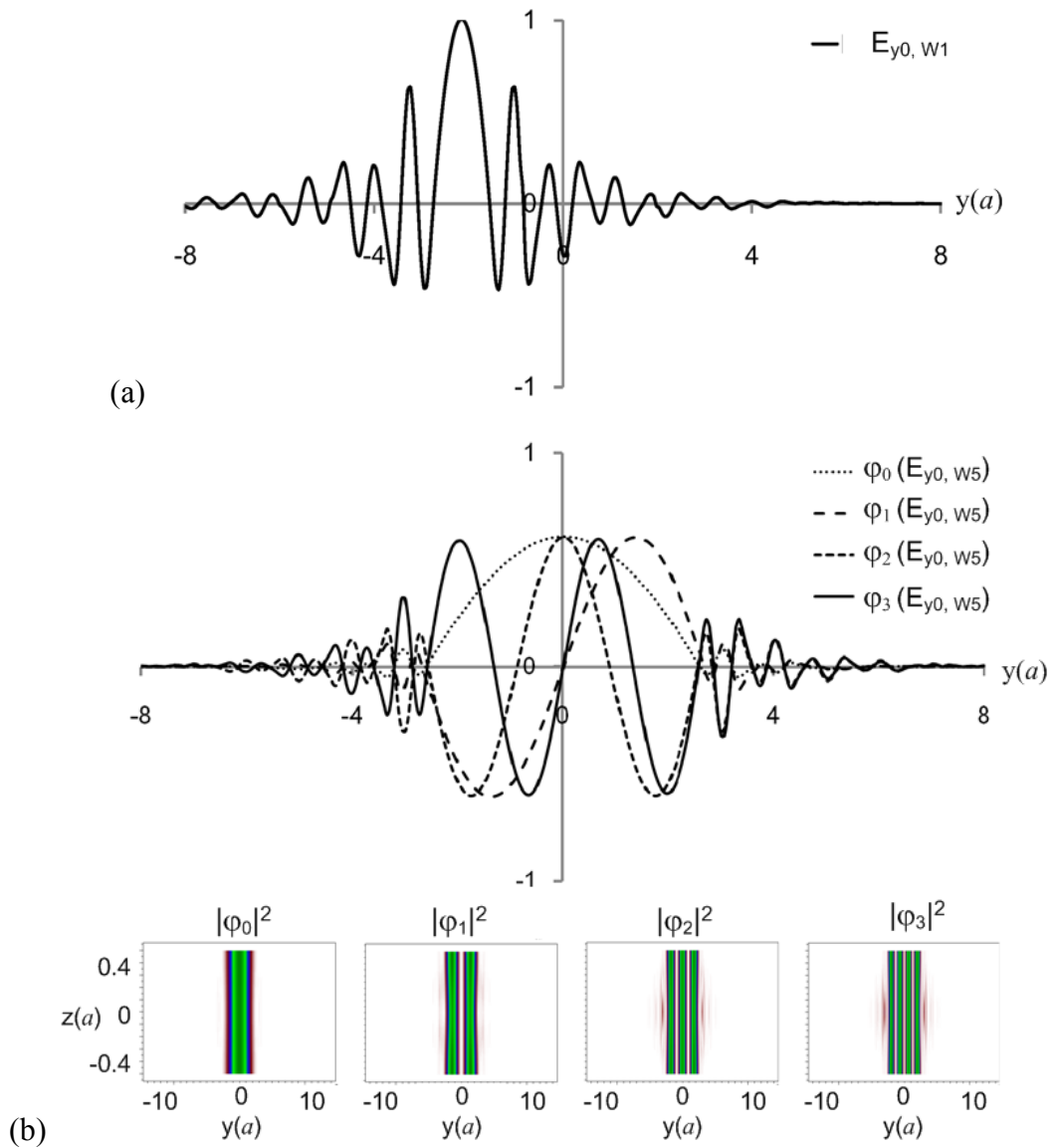


Fig. 5.10: (Color) Normalized field profiles of the (a) W1 and (b) W5 PC waveguides.

The power profile of these modes within the W5 PC waveguide calculated by Eq. (5.8) is shown in Fig. 5.11(a). The intensity distributions counterchange between Channel 1 and Channel 2, and strongly depend on the propagation distance. High intensity happens when these fields are constructive; therefore, the first peak of transmission along Channel 2 for a TM wave appears at $z = 6a$. The real part (dashed curve) and imaginary part (dotted curve) of the field superposition of all modes along

z -axis at $y = 2a$ are shown in Fig. 5.11(b). These fields form a beat wave with a period of $9.8a$ (solid curve), and the first peak happens at $z = 6a$. That is consistent to the dashed curve in Fig. 5.9.

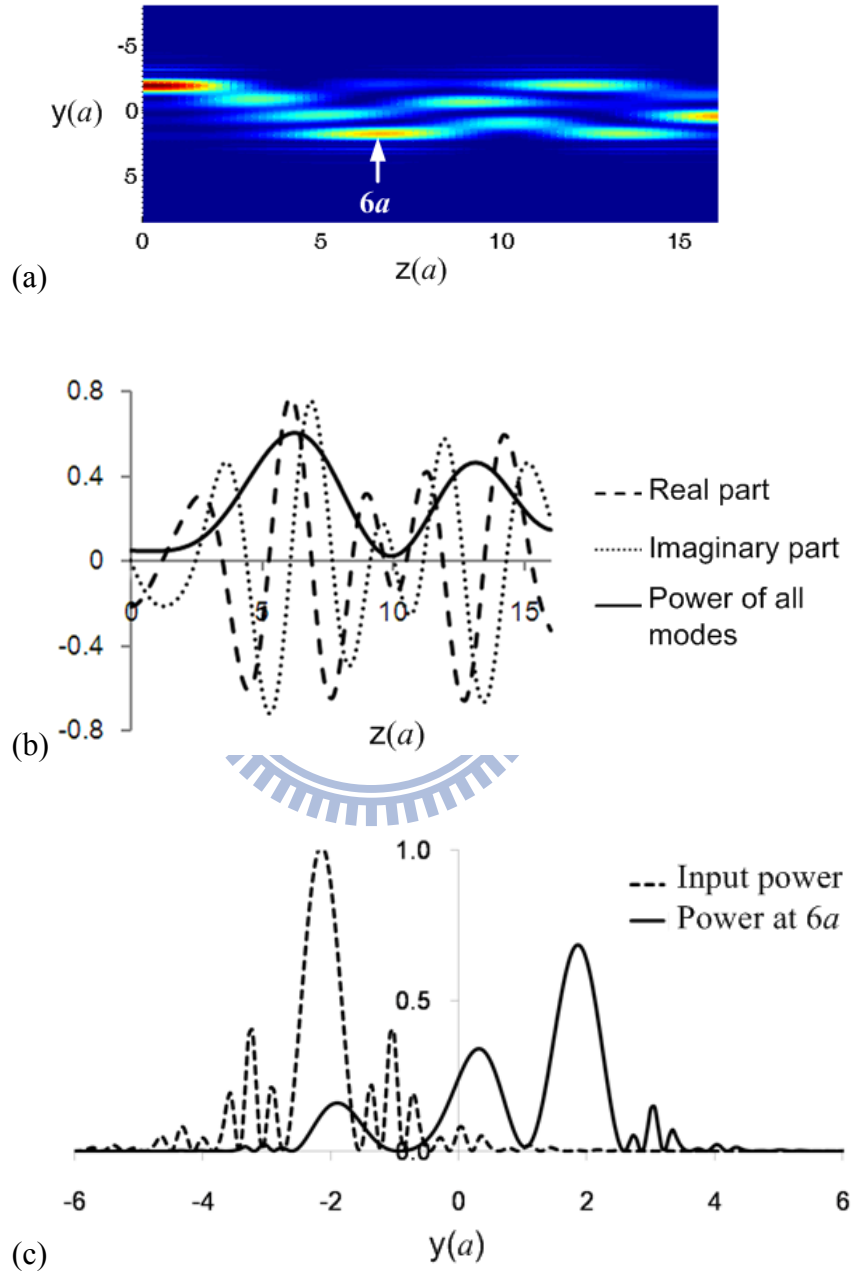


Fig. 5.11: (Color) (a) Power profile of all TM modes within the W5 PC waveguide. (b) Field superposition of all modes along the z -axis at $y = 2a$. (c) Power profile of a TM wave at $z = 6a$.

Image quality is an important factor while designed by the self-imaging principle. To reveal the image quality, the power profile of all modes at $z = 6a$ is shown in Fig. 5.11(c). Although the profile of a TM wave at $z = 6a$ is not a true mirror image of the input wave, the power within Channel 2 of the W5 PC waveguide is about 84% for this open-ended structure.

It has been shown that the interference effect within the MMI coupler for a TM wave is more sensitive to the propagation distance than that for a TE wave. We can use this difference behavior between TE and TM polarizations to design a compact PBS that can separate these two waves. The transmissions of a TE wave measured by Monitor A (solid curve) along Channel 1 in Fig. 5.8 and a TM wave measured by Monitor B (dashed curve) along Channel 2 in Fig. 5.9 are redrawn in Fig. 5.12. It can be seen that both transmissions along Channel 1 for a TE wave and Channel 2 for a TM wave are high at $6a$. Therefore, the ultra compact PC PBS we designed is shown in Fig. 5.13. The length of the MMI section is only seven lattice constants. To avoid the coupling between two output waveguides, a 90 degree bend is added to the lower output waveguide.

The TM wave will be routed to the lower output port (Port 2) after a propagation distance of the first peak along Channel 2. On the other hand, the TE wave will travel directly to the upper output port (Port 1) because its interference effect is weakly dependent on the propagation distance. The MMI coupler can separate two waves because it is a bar coupler for one wave and a cross coupler for another wave.

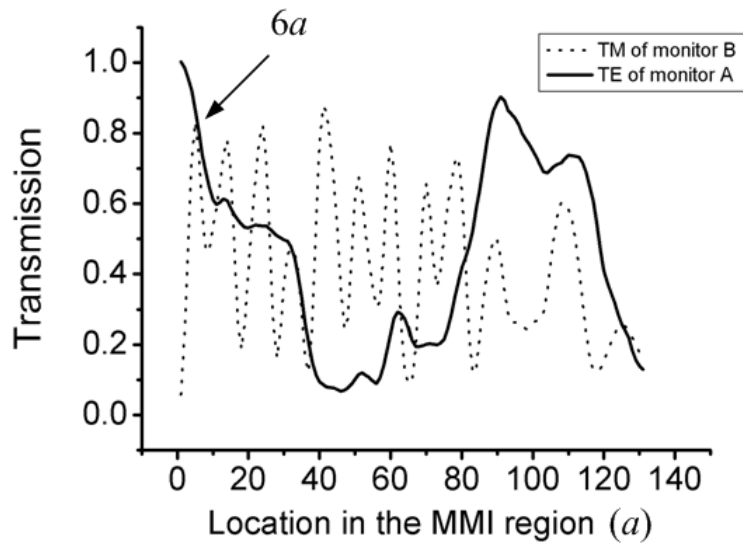


Fig. 5.12: Transmissions of TM wave measured by Monitor B (dashed curve) in Fig. 5.9 and TE wave measured by Monitor A (solid curve) in Fig. 5.8 under different positions within the W5 PC waveguide. It can be seen that both transmissions at Channel 1 for TE wave and at Channel 2 for TM wave are high at $6a$.

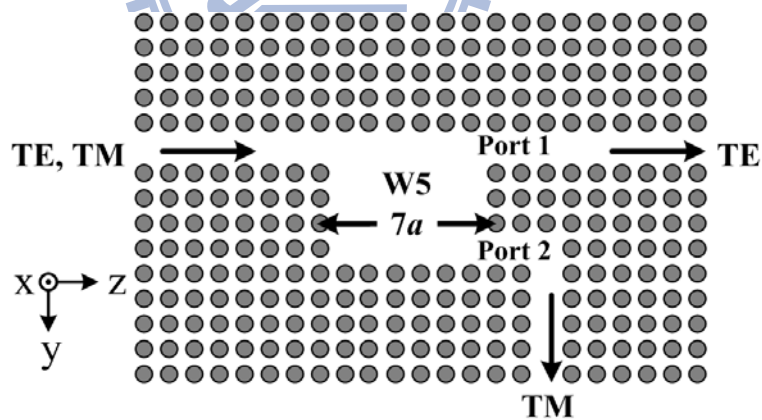


Fig. 5.13: Structure of the ultra compact PC PBS. The length of the MMI region is only $7a$. The TE wave is routed to the upper output port (Port 1) and TM wave to the lower output port (Port 2).

The steady-state electric field distributions of this PC PBS for TE and TM waves are shown in Fig. 5.14(a) and Fig. 5.14(b), respectively. It can be seen that the separation function of polarization beams works well. Transmissions, bending losses,

and extinction ratios of this compact PC PBS are listed in Table 5.4. Simulation results show that the insertion losses are 0.32 and 0.89 dB, and the extinction ratios are 14.4 and 17.5 dB for Port 1 (TE mode) and Port 2 (TM mode), respectively. The insertion loss of Port 2 includes the bending loss 0.7 dB. Note that the transmission at $6a$ is about 84% for an open-ended W5 PC waveguide, as shown in Fig. 5.8, and improved to above 93% for this PC PBS due to the existence of output waveguides. Seven lattice constants is the optimal length of the MMI section in this study. The PC PBS based on a directional coupler has been reported with a length of $24.2 \mu\text{m}$ [120]. Insertion losses and extinction ratios are found to be around 0.8 dB and 18-20 dB in other studies [118]. Therefore, this proposed MMI-based PC PBS has a compact size and high extinction ratio.

5.4 Summary

The design method of a compact PC PBS based on the difference of the interference effect between TE and TM polarizations is presented. The MMI region is a bar coupler for a TE wave and is a cross coupler for a TM wave, and its length is only $7a$. To our knowledge, this is the first study to show that a PC PBS can be designed by the MMI effect. Simulation results show that the insertion losses are 0.32 and 0.89 dB, and the extinction ratios are 14.4 and 17.5 dB for output Port 1 (TE mode) and Port 2 (TM mode), respectively. Compared with conventional counterparts of millimeter scale and other PC devices designed by self-imaging principle, this MMI-based PC PBS has advantages of compactness and low loss.

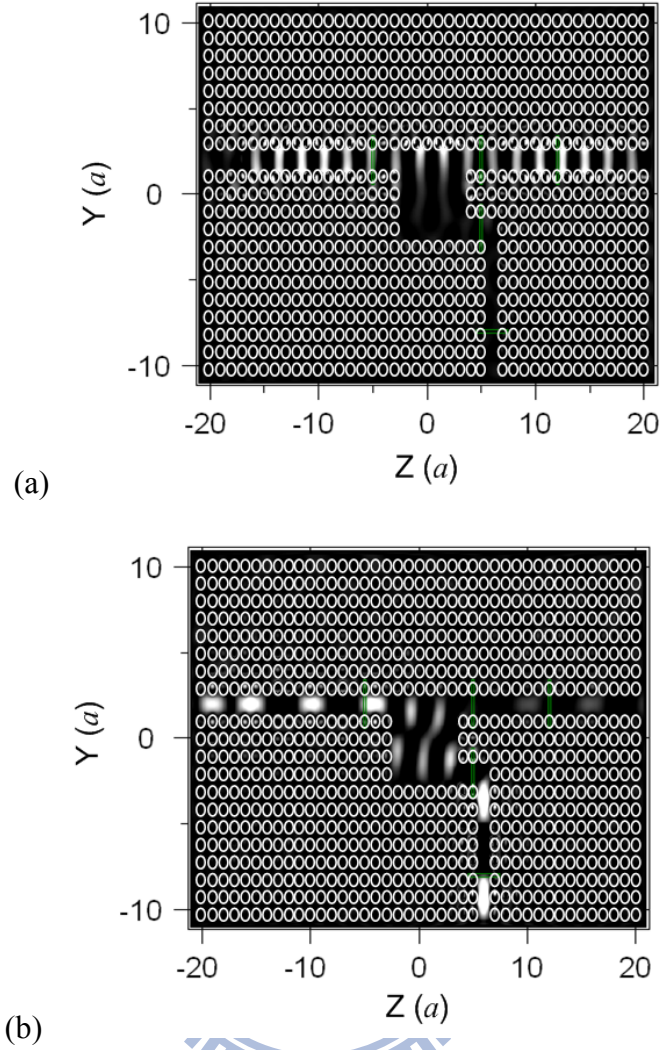


Fig. 5.14: Steady-state electric field distributions of the compact PC PBS for (a) TE and (b) TM waves.

Table 5.4: Transmissions, extinction ratios and insertion losses of the compact PC PBS.

	MMI Transmission		PBS Extinction Ratio	Insertion Loss
	TE	TM		
Port 1	93.0% (0.32 dB)	3.4% (14.7 dB)	14.4 dB	0.32 dB
Port 2	1.7% (17.7 dB)	95.8% (0.19 dB)	17.5 dB	0.89 dB

Chapter 6

Photonic Crystal Waveguides with Type-B Antiresonant Reflecting Optical Waveguide (ARROW-B) Structures

6.1 Introduction

Optical confinement in PC slab structures is supported by PBG guiding in a lateral plane and index guiding in the third dimension of the slab. In order to sustain a PBG and the feature of single-mode propagation, the core size of traditional PC slab waveguide is less than one micron. In contrast, single-mode optical fibers are in sizes on the order of a few microns. The coupling losses due to mismatch of core sizes between PC waveguides and fibers are on the order of 20–30 dB. Measurements and further applications of PC devices are limited by coupling issue. Thus, there have been many couplers proposed for efficient coupling, including gratings, mirrors, and tapered structures [131]-[133]. The research group of Ziolkowski showed some compact structures that consist of gratings, PBG mirrors or graded-index (GRIN) lens for perpendicular coupling between dielectric and PC waveguides [134]-[136]. Taillaert *et al.* found an out-of-plane grating coupler for efficient butt-coupling between planar waveguides and single-mode fibers [137]. Kuang *et al.* proposed that the PC cladding's periodicity can be a grating coupler to have high efficient coupling from optical fibers to PC waveguides [138]. In addition, Prather *et al.* demonstrated that a reflective parabolic mirror can be used to focus light from a multimode feed waveguide into a single-line-defect PC waveguide [139]. Mekis and Joannopoulos showed that tapered couplers can be used for efficient light coupling into and out of PC waveguides [26]. Happ *et al.* reported that light can be coupled into and out of a PC waveguide by adiabatic coupling with tapered slab waveguides [89], [92]. A mode matching technique

for highly efficient coupling based on setting localized defects in a PC tapered waveguide was reported [93]. Furthermore, Pottier *et al.* designed a PC continuous taper for low-loss direct coupling [140].

The highest coupling efficiency of those structures predicted by two-dimensional calculations can be greater than 90%. However, most of the couplers can only solve the coupling problem in the lateral plane. Balmer *et al.* proposed the vertically tapered epilayers as mode converters between waveguides and optical fibers [91]. But the length of waveguide taper must be over 1 millimeter for gradual expansion of mode sizes.

Antiresonant reflecting optical waveguide (ARROW) utilizes Fabry-Perot cavities as the reflectors instead of the total internal reflection. Hence, in comparison with conventional waveguides, it has some advantageous features: wave propagating in a low-index core and with relatively large core size suitable for efficient connection to single-mode fibers, flexible structure design rules, easy fabrication process, and low-loss with good light confinement. We have shown that a PC waveguide based on an ARROW platform has high transmission and low bending loss [141]. However, ARROW structures guide TE waves only, whereas type-B antiresonant reflecting optical waveguide (ARROW-B) structures support TE and TM modes [55], [56]. Note that in order to be compatible with the convention used in optical waveguide, TE-polarization (TM-polarization) indicates that the electric (magnetic) fields are perpendicular to the direction of light propagation. This study presents a PC waveguide based on an ARROW-B platform. Light waves propagating in this PC waveguide are confined by antiresonant reflection vertically and the PBG laterally. We will show that the PC waveguide based on an ARROW-B platform also has high transmission and low bending loss, and can solve the coupling issue with single-mode fibers in the vertical direction.

In the following sections, the related parameters of this new device based on

semiconductor process will be designed. The transmissions of ARROW-B-based waveguides and bending losses of waveguide bends for TE and TM modes will also be discussed. Finally, with the aid of a PC tapered coupler, the coupling ability between optical fibers and PC waveguides with an ARROW-B structure will be demonstrated.

6.2 Design of a PC Waveguide Based on an ARROW-B

Platform

As shown in Fig. 6.1, ARROW is a kind of layered structure consisting of a pair of interference cladding layers sandwiched by a core and a substrate and the refractive index of the first cladding is higher than those of the core and the second cladding [50]. In an ARROW-B structure, the refractive index of the first cladding is smaller than those of the core and the second cladding. The thickness of the first cladding layer is so thin that there is an evanescent field reaching the interface of this layer and the second cladding, which results in a frustrated total internal reflection. This reflection is also a kind of interference reflection. Since the first reflection at the interface between the core and the first cladding dominates the overall reflection, the reflectivity in ARROW-B is less dependent on the polarization than in ARROW. Thus, not only TE wave but also TM wave can propagate with low losses in ARROW-B waveguides.

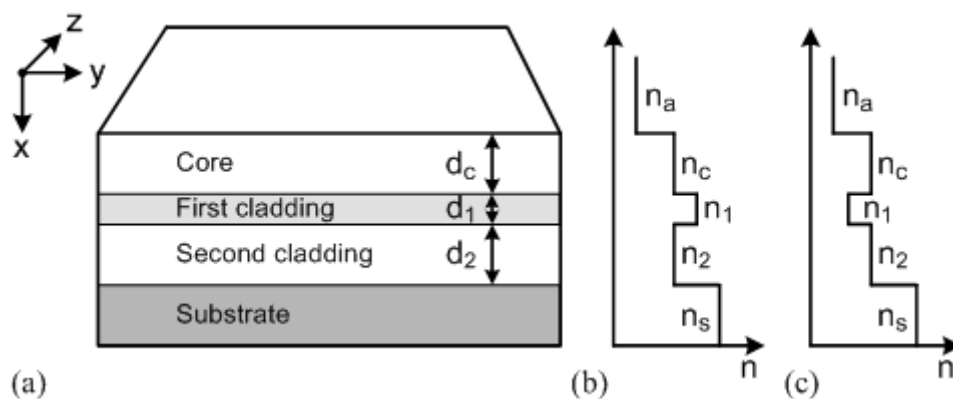


Fig. 6.1: (a) Cross sectional view of an ARROW structure. (b) Index profile of an ARROW structure. (c) Index profile of an ARROW-B structure.

The photonic crystal waveguide with an ARROW-B structure we proposed is shown in Fig. 6.2. The PC structure is a triangular lattice of air holes arranged on an ARROW-B plane. The triangular lattice with a much wider bandgap than the square lattice causes the greater symmetry and the smoother Brillouin zone. A PC waveguide is formed by removing a line of air holes along the z -direction. As a consequence, the optical confinement of this waveguide is supported by the PBG in the lateral plane and by the antiresonant reflection rather than the index guiding in the vertical direction of the slab.

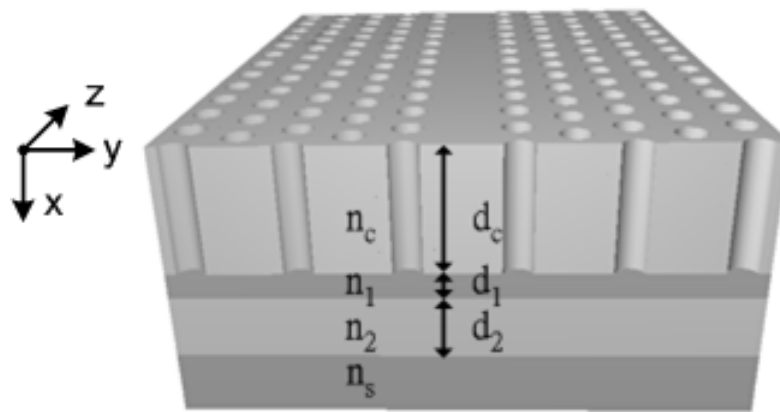


Fig. 6.2: A photonic crystal waveguide based on an ARROW-B platform.

The first step is to determine the material and thickness of each layer used in the ARROW-B structure. For the purpose of further integration with other optical components, the waveguide is designed on a silicon substrate, and the material of the first cladding layer is SiO₂. Therefore, $n_s = 3.5$ and $n_1 = 1.45$, where n_s and n_1 are the refractive indices of the substrate and the first cladding layer, respectively. In order to be compatible to single-mode fibers for 1.55- μm operations, the thickness of core d_c is designed as 8 μm . Under the condition of antiresonance, the thickness of second

cladding satisfies [50], [79]

$$d_2 \cong \frac{\lambda}{4n_2} \left(1 - \frac{n_c^2}{n_2^2} + \frac{\lambda^2}{4n_2^2 d_c^2}\right)^{-1/2} (2M + 1), \quad M = 0, 1, 2, 3, \dots, \quad (6.1)$$

where n_c and n_2 are the refractive indices of the core and second cladding, respectively. It is found that there is an appropriate joint band gap when the refractive index of the core is equal to 3.2. In most cases, the material of the second cladding is usually the same as that of the core, so n_c and n_2 are chosen to be 3.2. Porous silicon or polycrystalline silicon with doping can be the materials of core and the second cladding layers. If the refractive index of the core is equal to that of the second cladding, Eq. (6.1) can be reduced to

$$d_2 \cong d_c (N + 1/2), \quad N = 0, 1, 2, 3, \dots, \quad (6.2)$$

In most cases, d_2 is designed to be half of the thickness of the core, that is $d_2 = 0.5d_c = 4 \mu\text{m}$.

The thickness requirement of the first cladding layer of an ARROW-B waveguide is to have loss discrimination between the fundamental mode and higher order modes. Fig. 6.3(a) and Fig. 6.3(b) show the propagation losses as a function of the thickness of the first cladding layer for TE and TM modes, respectively. When d_1 is $0.05 \mu\text{m}$, the propagation losses of fundamental modes are smaller than 0.1 dB/cm both for TE and TM modes. On the other hand, losses of higher order modes are much greater than those of fundamental modes. That makes this waveguide an effective single-mode device. In summary, the device parameters of the ARROW-B-based waveguide are $n_d/n_c/n_1/n_2/n_s = 1.00/3.20/1.45/3.20/3.50$, and $d_c/d_1/d_2 = 8.00/0.05/4.00 \mu\text{m}$.

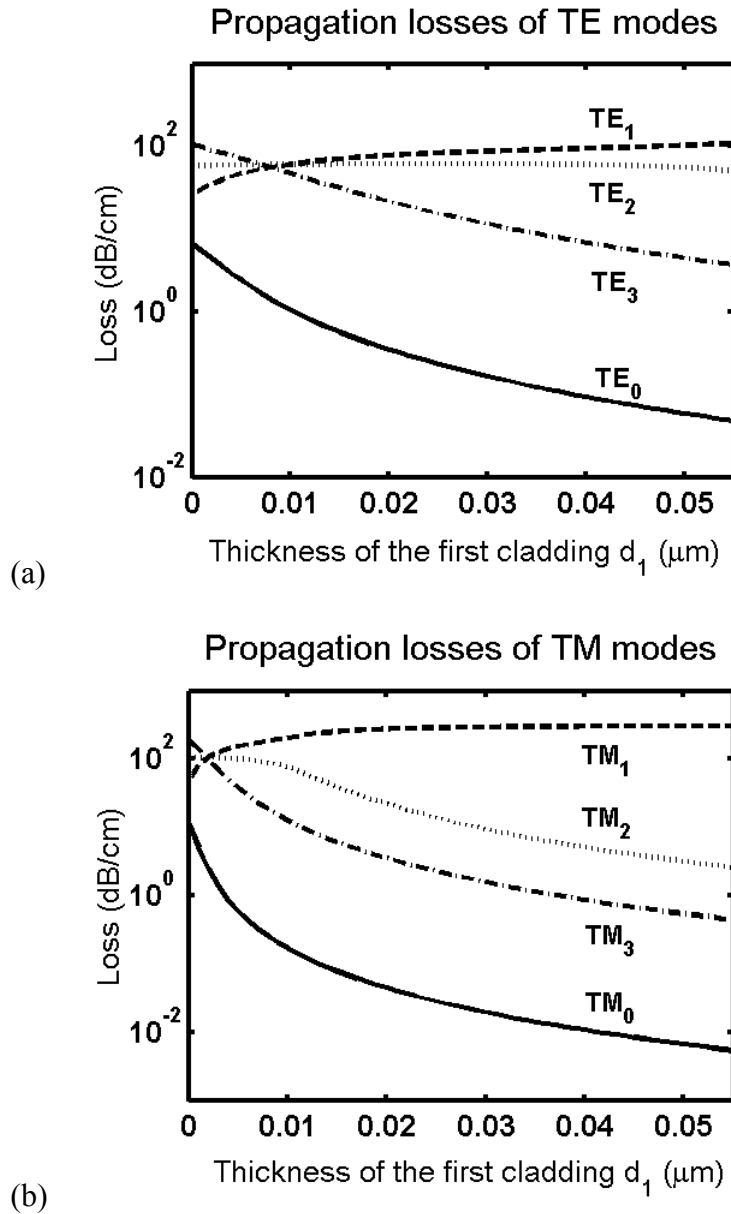


Fig. 6.3: Propagation losses of the ARROW-B waveguide as a function of the thickness of the first cladding layer for (a) TE modes and (b) TM modes.

Next, the parameters of the PC structure will be determined from the photonic band gap. When the refractive index of background is 3.2, the gap map of a PC structure with a triangular lattice calculated by plane wave expansion (PWE) method is shown in Fig. 6.4. There is a maximum joint gap at $r/a = 0.47$, where r is the radius of air hole and a is the lattice constant. The corresponding frequency range of joint band gap is between

0.46 and $0.51(a/\lambda)$ and the central frequency is 0.485. For the operating wavelength $\lambda = 1.55 \mu\text{m}$, the lattice constant $a = 0.485\lambda = 0.752 \mu\text{m}$ and the radius of the air hole $r = 0.47a = 0.353 \mu\text{m}$. The diameter of air holes is larger than that of conventional PC waveguides, meaning that it can be realized by photolithography and does not require the electron-beam lithography and high-resolution dry etching.

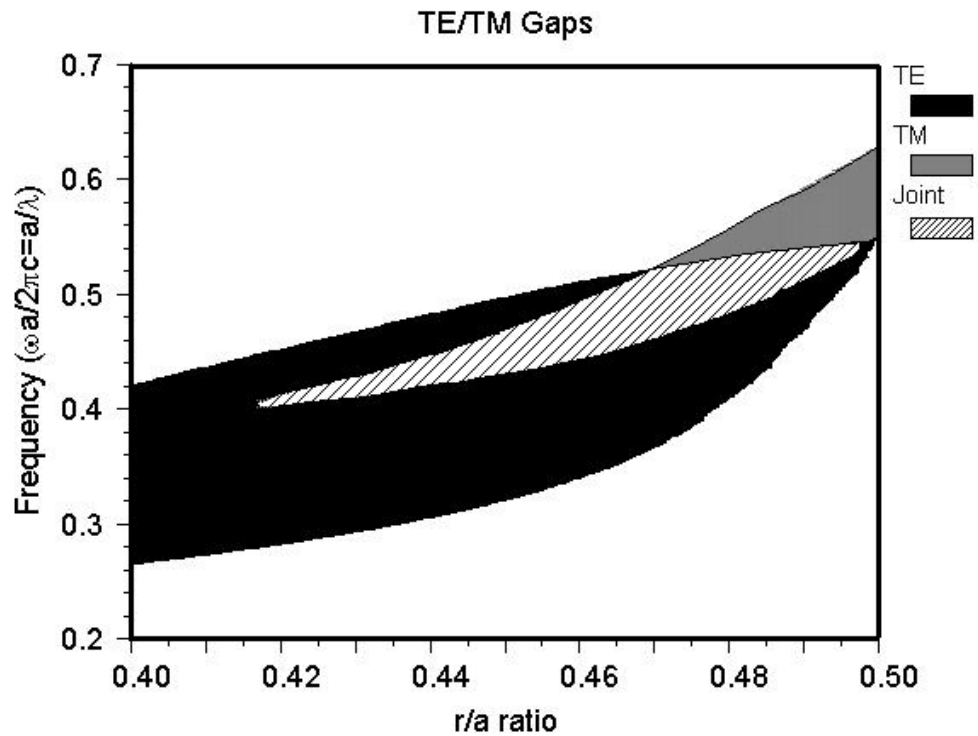


Fig. 6.4: The joint band gap of a photonic crystal structure with a triangular lattice. The refractive index of background is 3.2.

6.3 Characteristics of a PC Waveguide Based on an ARROW-B Platform

6.3.1 Transmission

A Gaussian beam is launched from the input of the ARROW-B-based PC waveguide to calculate its transmission. The transmission is defined as the ratio of the measured power to the input power. Because huge memory and computational time required for three-dimensional finite difference time domain (3D FDTD) method, the length of device under simulation is about $100a$. The propagation losses are 12.3 dB/mm and 19.3 dB/mm for TE and TM modes, respectively, at the operating wavelength $\lambda = 1.55 \mu\text{m}$. The transmission of a 20- μm ARROW-B-based PC waveguide as a function of the normalized frequency (a/λ) for TE and TM modes simulated by 3D FDTD method is shown in Fig. 6.5. It can be seen that the average transmission efficiency in the frequency range of band gap exceeds 90% both for TM and TE modes. The good confinement of wave in the ARROW-B-based PC waveguide is supported by the PBG in the lateral plane and by the antiresonant reflection in the vertical direction of the slab.

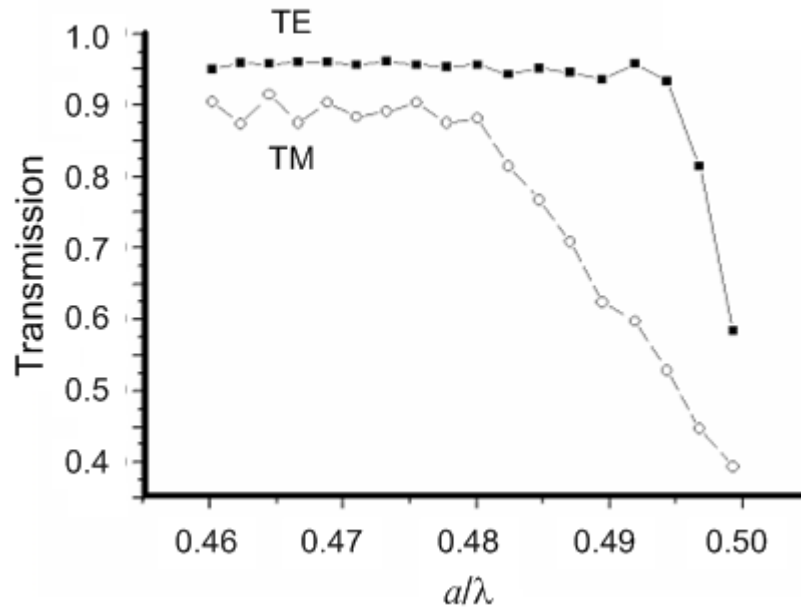
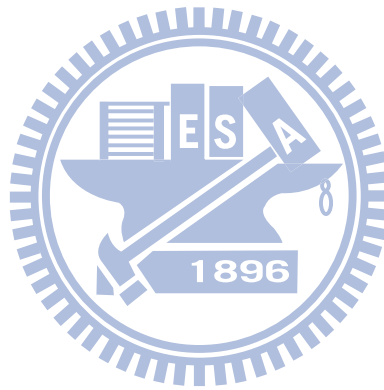


Fig. 6.5: Transmission spectra for TE and TM modes.

6.3.2 Bend Loss

One of the most attractive features of PC waveguides is allowing sharp bends with low losses. Due to back reflection and radiation loss at the bend corner, the transmission of a PC waveguide bend will be decreased. Therefore, there have been many PC bend structures proposed for transmission and bandwidth improvement [79]-[81]. Though the ARROW-B-based PC waveguide has low propagation loss at the operating wavelength $\lambda = 1.55 \mu\text{m}$, the transmission through a 60° ARROW-B-based PC waveguide bend is only 44.6% for TE mode and 39.5% for TM mode. Fig. 6.6(a) shows the propagation of TE wave in a 60° ARROW-B-based PC waveguide bend. We have shown that the transmission of a PC waveguide bend can be significantly improved by shifting the lattice points around the bend corner [142]. If the lattice points around the bend corner are shifted $0.3a$ along the Γ -K direction indicated by the arrow in Fig. 6.6(b), the transmission of this 60° PC waveguide bend with offset can be improved to 97.9% (0.09

dB/bend) and 91.0% (0.40 dB/bend) for TE and TM modes, respectively. Furthermore, this mode matching technique can also be used to design a high efficient 120° PC waveguide bend. For a 120° ARROW-B-based PC waveguide bend as shown in Fig. 6.6(c), most of the power of light is reflected backward from the bend corner. Therefore, the transmission is only 22.9% for TE mode and 18.8% for TM mode. The directions are the same for 60° and 120° in a PC structure with a hexagonal array of lattices. Therefore, if the lattice points around the bend corner are shifted $0.3a$ along the Γ -K direction indicated by the arrow in Fig. 6.6(d), the transmission of this 120° ARROW-B-based PC waveguide bend with offset is dramatically improved to 83.9% (0.76 dB/bend) and 80.0% (0.99 dB/bend) for TE and TM modes, respectively.



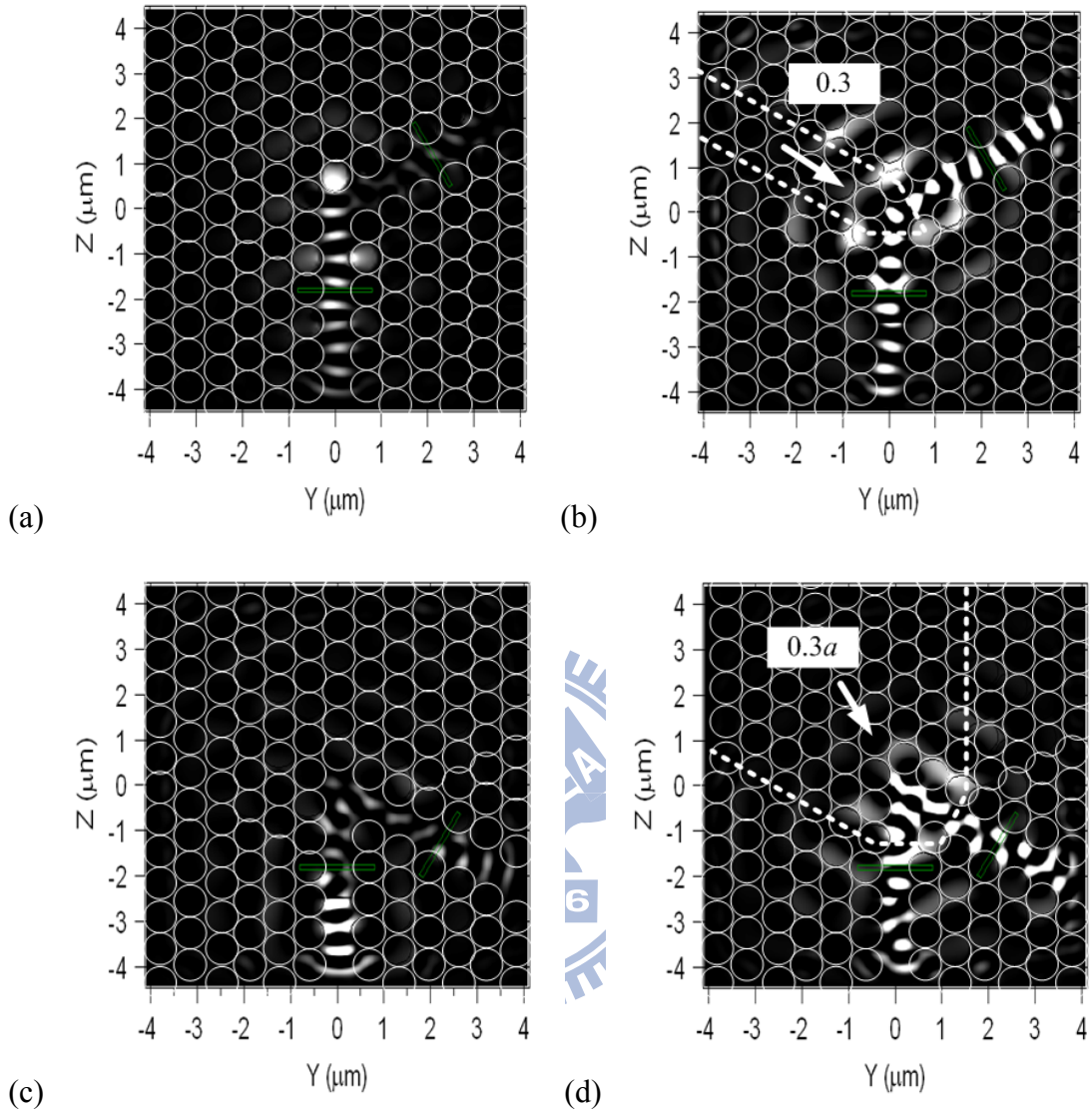


Fig. 6.6: (a) The wave propagation in a 60° PC waveguide bend without offset (TE mode as an example). (b) The propagation of wave in the 60° PC waveguide bend with offset. The lattice points around the bend corner are shifted $0.3a$ along the Γ -K direction indicated by the arrow. (c) The wave propagation in a 120° PC waveguide bend without offset (TE mode as an example). (d) The propagation of wave in the 120° PC waveguide bend with offset. The lattice points around the bend corner are shifted $0.3a$ along the Γ -K direction indicated by the arrow.

6.3.3 Butt Coupling Efficiency

To maintain the features of single-mode and PBGs, the core sizes of PC waveguides must be less than half of a micron. On the contrary, the core diameters of single-mode fibers operating at 1.55 μm are normally 6-10 μm . Due to mismatch of core sizes, the butt-coupling efficiencies between a conventional PC waveguide and a single-mode optical fiber are on the order of 20-30 dB. The core layer of a PC waveguide based on an ARROW-B platform is as thick as 8 μm ; therefore, the coupling efficiency can be improved. An ARROW-B-based PC waveguide coupled directly with a single-mode optical fiber is shown in Fig. 6.7(a) and its top view is shown in Fig. 6.7(b). The refractive indices of fiber core and cladding are $n_{\text{core}} = 1.451$ and $n_{\text{cladding}} = 1.445$, respectively, and the core diameter of fiber is 6 μm . Light source of fiber mode is launched from the optical fiber and the coupling efficiency is monitored. Coupling efficiency is defined as the ratio of power measured at the input of PC waveguide to that measured at the end of fiber. Although the interface changes abruptly from 6 μm to 0.6 μm as light propagates from a single-mode fiber to an ARROW-B-based PC waveguide, the coupling efficiencies calculated by 3D FDTD are 28.1% (-5.516 dB) for the TE mode and 34.4% (-4.634 dB) for the TM mode, respectively. The efficiency improvement is mainly a result of mode matching in the vertical direction due to the large core size of an ARROW-B-based PC waveguide.

The tapered coupler is the most popular device used in connecting PC waveguides and other optical devices. In order to further improve the coupling ability of our device, a PC tapered coupler which acts as a mode converter is placed between a single-mode optical fiber and an ARROW-B-based PC waveguide as shown in Fig. 6.7(c). The width of the PC tapered coupler decreases gradually from 6 μm to 0.6 μm and the length of each section is $3.5a$ as in Fig. 6.7(d). The coupling efficiencies calculated by 3D FDTD

are 82.0% (-0.862 dB) and 82.5% (-0.834 dB) for TE and TM modes, respectively. The high coupling efficiencies are mainly the consequence of mode matching in the vertical direction by the ARROW-B structure and mode conversion in the lateral direction provided by the PC tapered coupler.

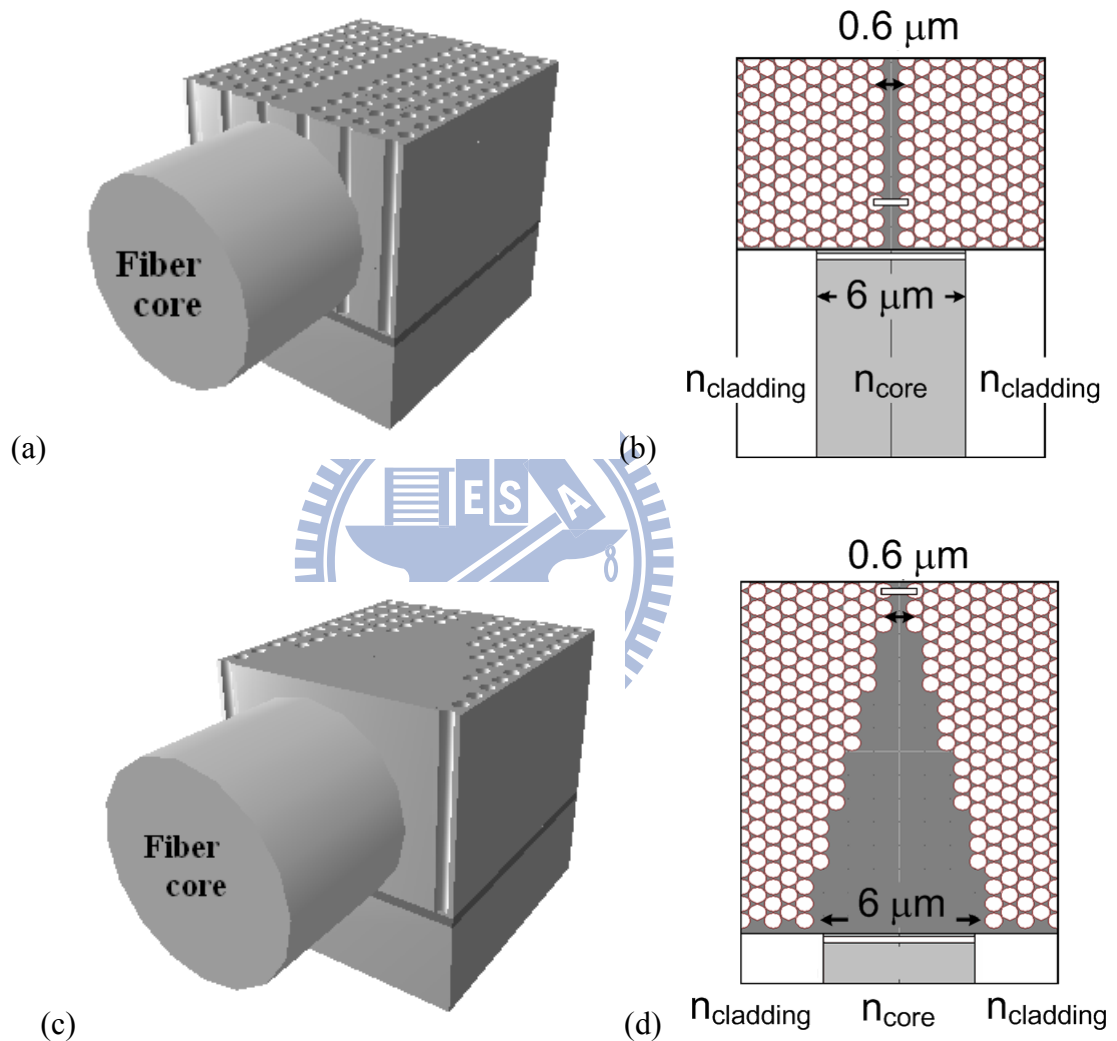


Fig. 6.7: (a) An ARROW-B-based PC waveguide coupled directly with a single-mode optical fiber. (b) The top view of (a). (c) An ARROW-B-based PC waveguide coupled with a single-mode optical fiber through a three-dimensional PC tapered coupler. (d) The top view of (c).

6.4 Summary

A photonic crystal waveguide based on an ARROW-B platform is proposed in this study. Optical confinement of this device is supported by PBGs in the lateral plane and by the antiresonant reflection in the vertical direction of the slab. Finite-thickness slabs can support modes with higher order. If the slab is too thick, the presence of these modes can result in closing of the bandgap [143]. Therefore, the thickness of the slab is a critical parameter in conventional structure and needs to be modeled. Even though the core size is as thick as 8 μm , this ARROW-B-based PC waveguide supports quasi-single mode. The ARROW-B-based PC waveguide has high transmission and low bending loss. The propagation losses are 12.3 dB/mm and 19.3 dB/mm for TE and TM modes, respectively. The bending losses of 60° and 120° ARROW-B-based PC waveguide bends are 0.09 dB/bend and 0.76 dB/bend for the TE mode, and 0.40 dB/bend and 0.99 dB/bend for the TM mode. Furthermore, with the aid of a PC tapered structure, the butt coupling efficiencies between a single-mode optical fiber and a PC waveguide with an ARROW-B structure can be as high as 82.0% and 82.5% for TE and TM modes, respectively. Simulation results show that an ARROW-B structure can be served as a platform for PC devices.

Besides our group, we have noticed that other researchers studied the PC waveguides based on an antiresonant reflecting platform [144]-[147]. Litchinitser proposed a simple analytical theory for low-index core photonic bandgap optical waveguides based on an antiresonant reflecting guidance mechanism and discussed the implications of the results for photonic bandgap fibers [144]. Lavrinenko applied the antiresonant reflecting layers arrangement to silicon-on-insulator based photonic crystal waveguides [147]. They analyzed several layered structures with different combinations of materials. Simulation results reveal that PC waveguides with an ARROW or

ARROW-B structure have potential for competing with membrane-like photonic crystal waveguides.



Chapter 7

Conclusion

In this study, we have shown that a high efficient photonic crystal waveguide bend can be designed by mode matching technique. By shifting lattice points around the bend corner, the bound state in the waveguide bend and the guided mode in the straight waveguide can be matched. The transmissions of the 60° and 120° PC waveguide bend with mode matching are improved significantly. The bound state in a waveguide bend is similar to a cavity mode; therefore, the PC waveguide bend performs a narrow-band transmission. Frequency-shift of the spectra for a PC waveguide bend due to this lattice shifting is observed.

The multimode interference phenomena in multiple-line-defect PC waveguides have been studied. It is found that the optimal length of each section in a PC step tapered coupler is related to the imaging length of MMI. Therefore, a PC step tapered coupler with different section lengths is proposed. The optimal structure can provide mode matching between two adjacent sections and reduce the scattering loss occurring at the corners of abrupt steps. We also revealed the reason why in some cases the transmission of PC step tapered couplers decreases counterintuitively when the taper length is increased.

Based on the MMI effect, the compact PC polarization beam splitter is proposed. This compact PC PBS is based on the difference of interference effect between TE and TM modes. Within the MMI coupler, the dependence of interference of modes on propagation distance is weak for a TE wave and strong for a TM wave; as a result, the length of the MMI section is only seven lattice constants. Simulation results show that this PBS has low insertion losses and high extinction ratios for TE and TM modes. The same method can be applied to the design of PC power splitters, wavelength

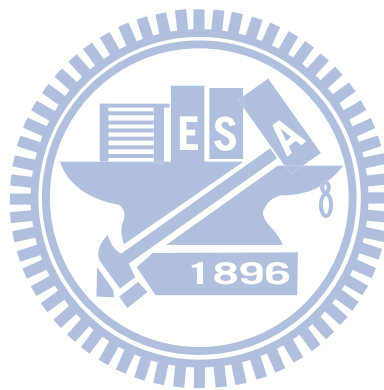
multiplexing, and demultiplexing devices, etc.

We have shown that the ARROW-B structure is a good platform for PC devices. Optical confinement of a PC slab waveguide based on an ARROW-B platform is supported by PBGs in the lateral plane and by the antiresonant reflection in the vertical direction of the slab. The core size of the ARROW-B-based PC waveguide is thicker than that of a conventional PC waveguide; however, it can support quasi-single mode and has high transmission for TE and TM modes. By mode matching technique, the 60° and 120° ARROW-B-based PC waveguide bends with low bending losses can be designed. Furthermore, with the aid of a PC step tapered structure, the butt coupling efficiency between a single-mode optical fiber and a PC waveguide with an ARROW-B structure is improved.

Though the test cases we studied in each chapter are different, the design methods we proposed are based on the mode matching technique and multimode interference those are basic physics; therefore, the methodologies can be applied to general cases. In the real world, the characteristics of a PC structure are three-dimensional problems to be solved. The finite heights and radiation losses are issues that need to be taken into account in practical 3D PC devices. The guided modes of a slab waveguide are not completely confined in the slab. The energy of the guided mode extends into the air; therefore, the bands will be at higher frequencies than in the case of 2D. In addition, modes with frequencies above the light line will couple to the radiation modes and leak energy into the air, and thus represent the loss mechanism of the waveguide. However, we can investigate the MMI phenomena and find out the physics easily in a simplified two-dimensional model. While a 3D problem is converted to a 2D model, the dielectric constant of the host medium must be replaced by its effective index.

In the future, the fabrication and measurement of PC devices based on an ARROW-B platform will be carried out. The manufacturing of ARROW-B based PC

devices is going on at National Nano Device Laboratories (NDL). The transmission of a photonic crystal waveguide can be experimentally investigated using the end-fire coupling. Light from a diode laser that can be tuned over a broad wavelength range is transmitted through an optical fiber and focused onto the waveguide facet. The light emitted from the other end of the waveguide is imaged on a camera or detected by a photodiode. Further works will be required to set up these equipments and collect useful data.



Bibliography

- [1] E. Yablonovitch, "Inhibited spontaneous emission in solid-state physics and electronics," *Phys. Rev. Lett.*, vol. 58, no. 20, pp. 2059-2062, 1987.
- [2] S. John, "Strong localization of photons in certain disordered dielectric superlattices," *Phys. Rev. Lett.*, vol. 58, no. 23, pp. 2486-2489, 1987.
- [3] V. P. Bykov, "Spontaneous emission in a periodic structure," *Sov. Phys.*, no. 35, pp. 269-273, 1972.
- [4] V. P. Bykov, "Spontaneous emission from a medium with a band spectrum," *Sov. J. Quant. Electron.*, no. 4, pp. 861-871, 1975.
- [5] D. M. Pustai, A. Sharkawy, S. Shi, and D. W. Prather, "Tunable photonic crystal microcavities," *Appl. Opt.*, vol. 41, no. 20, pp. 5574-5579, 2002.
- [6] G. Subramania, S. Y. Lin, J. R. Wendt, and J. M. Rivera, "Tuning the microcavity resonant wavelength in a two-dimensional photonic crystal by modifying the cavity geometry," *Appl. Phys. Lett.*, vol. 83, no. 22, pp. 4491-4493, 2003.
- [7] K. Srinivasan, P. E. Barclay, and O. Painter, "Fabrication-tolerant high quality factor photonic crystal microcavities," *Opt. Express*, vol. 12, no. 7, pp. 1458-1463, 2004.
- [8] Z. Zhang and M. Qiu, "Small-volume waveguide-section high Q microcavities in 2D photonic crystal slabs," *Opt. Express*, vol. 12, no. 17, pp. 3988-3995, 2004.
- [9] D. Englund, I. Fushman, and J. Vuckovi, "General recipe for designing photonic crystal cavities," *Opt. Express*, vol. 12, no. 16, pp. 5961-5979, 2005.
- [10] T. Asano, B. S. Song, and S. Noda, "Analysis of the experimental Q factors (~ 1 million) of photonic crystal nanocavities," *Opt. Express*, vol. 14, no. 5, pp. 1996-2002, 2006.
- [11] D. N. Chigrin, A. V. Lavrinenko, D. A. Yarotsky, and S. V. Gaponenko,

- “All-dielectric one-dimensional periodic structures for total omnidirectional reflection and partial spontaneous emission control,” *J. Lightwave Technol.*, vol. 17, no. 11, pp. 2018-2024, 1999.
- [12] V. Tolmachev, T. Perova, and K. Berwick, “Design criteria and optical characteristics of one-dimensional photonic crystals based on periodically grooved silicon,” *Appl. Opt.*, vol. 42, no. 28, pp. 5679-5683, 2003.
- [13] A. S. Jugessur, P. Pottier, and R. M. De La Rue, “One-dimensional periodic photonic crystal microcavity filters with transition mode-matching features, embedded in ridge waveguides,” *Electron. Lett.*, vol. 39, no. 4, pp. 367-369, 2003.
- [14] J. T. Shen and S. Fan, “Coherent photon transport from spontaneous emission in one-dimensional waveguides,” *Opt. Lett.*, vol. 30, no. 15, pp. 2001–2003, 2005.
- [15] J. J. Li, Z. Y. Li, and D. Z. Zhang, “Second harmonic generation in one-dimensional nonlinear photonic crystals solved by the transfer matrix method,” *Phys. Rev. E*, vol. 75, no. 5, pp. 056606-1~7, 2007.
- [16] C. J. M. Smith, H. Benisty, D. Labilloy, U. Oesterle, R. Houdre, T. F. Krauss, R. M. De La Rue and C. Weisbuch, “Near-infrared microcavities confined by two dimensional photonic bandgap crystals,” *Electron. Lett.*, vol. 35, no. 3, pp. 228-230, 1999.
- [17] E. Chow, S. Y. Lin, S. G. Johnson, P. R. Villeneuve, J. D. Joannopoulos, J. R. Wendt, G. A. Vawter, W. Zubrzycki, H. Hou, and A. Alleman, “Three-dimensional control of light in a two-dimensional photonic crystal slab,” *Nature*, vol. 407, pp. 983- 86, 2000.
- [18] Y. Akahane, T. Asano, H. Takano, B. S. Song, Y. Takana, and S. Noda, “Two-dimensional photonic-crystal-slab channel drop filter with flat-top response,” *Opt. Express*, vol. 13, no. 7, pp. 2512-2530, 2005.
- [19] K. Sakai, E. Miyai, and S. Noda, “Two-dimensional coupled wave theory for

- square-lattice photonic-crystal lasers with TM-polarization,” *Opt. Express*, vol. 15, no. 7, pp. 3981-3990, 2007.
- [20] C. Sell, C. Christensen, G. Tuttle, Z. Y. Li, and K. M. Ho, “Propagation loss in three-dimensional photonic crystal waveguides with imperfect confinement,” *Phys. Rev. B*, vol. 68, no. 11, pp. 113106-1~4, 2003.
- [21] L. Pierantoni, A. Massaro, and T. Rozzi, “Efficient modeling of 3-D photonic crystals for integrated optical devices,” *IEEE Photon. Technol. Lett.*, vol. 18, no. 2, pp. 319-321, 2006.
- [22] M. Che, Z. Y. Li, and R. J. Liu, “Tunable optical anisotropy in three-dimensional photonic crystals,” *Phys. Rev. A*, vol. 76, no. 2, pp. 023809-1~4, 2007.
- [23] S. A. Rinne, F. G. Santamaria, and P. V. Braun, “Embedded cavities and waveguides in three-dimensional silicon photonic crystals,” *Nature Photonics*, vol. 2, pp. 52-56, 2008.
- [24] S. Y. Lin and J. G. Fleming, “A three-dimensional optical photonic crystal,” *J. Lightwave Technol.*, vol. 17, no. 11, pp. 1944-1947, 1999.
- [25] S. Kawashima, L. H. Lee, M. Okano, M. Imada, and S. Noda, “Design of donor-type line-defect waveguides in three-dimensional photonic crystals,” *Opt. Express*, vol. 13, no. 24, pp. 9774-9781, 2005.
- [26] A. Mekis, J. C. Chen, I. Kurland, S. Fan, P. R. Villeneuve, and J. D. Joannopoulos, “High transmission through sharp bends in photonic crystal waveguides,” *Phys. Rev. Lett.*, vol. 77, no. 18, pp. 3787-3790, 1996.
- [27] B. Temelkuran and E. Ozbay, “Experimental demonstration of photonic crystal based waveguides,” *Appl. Phys. Lett.*, vol. 74, no. 4, pp. 486 - 488, 1999.
- [28] M. Loncar, D. Nedeljkovic, T. Doll, J. Vuckovic, A. Scherer, and T. P. Pearsall, “Waveguiding in planar photonic crystals,” *Appl. Phys. Lett.*, vol. 77, no. 13, pp. 1937-1939, 2000.

- [29] S. Boscolo, C. Conti, M. Midrio, and C. G. Someda, "Numerical analysis of propagation and impedance matching in 2-D photonic crystal waveguides with finite length," *J. Lightwave Technol.*, vol. 20, no. 2, pp. 304-310, 2002.
- [30] N. Susa, "Towards perfect vertical photonic band gap confinement in a photonic crystal slab," *Jpn J. Appl. Phys.*, vol. 42, part 1, no. 11, pp. 7157-7162, 2003.
- [31] J. Witzens, T. B. Jones, M. Hochberg, M. Loncar, and A. Scherer, "Photonic crystal waveguide-mode orthogonality conditions and computation of intrinsic waveguide losses," *J. Opt. Soc. Am. A*, vol. 20, no. 10, pp. 1963-1968, 2003.
- [32] 湯家榮, "A study of photonic band gap materials by finite-difference time-domain method," M. S. Thesis, National Taiwan University, 2001.
- [33] 汪天仁, "二維光子晶體之帶隙分析," M. S. Thesis, National Taiwan University, 2001.
- [34] 巫金樺, "Potential applications of photonic crystals by using finite-difference time-domain method," M. S. Thesis, Tatung University, 2001.
- [35] 許委斌, "The study of finite-difference time-domain method and its applications on photonic crystals," M. S. Thesis, Tatung University, 2001.
- [36] 蔡雅芝, "Formation and properties of band gaps in photonic crystals," M. S. Thesis, National Tsing Hua University, 1997.
- [37] 王志明, "Terahertz photonic crystals," M. S. Thesis, National Tsing Hua University, 1998.
- [38] 王海蒂, "Two-dimensional photonic crystal in THz range - Using etched silicon wafer stack," M. S. Thesis, National Tsing Hua University, 2000.
- [39] 賴瑋治, "The study of two dimensional terahertz photonic crystal," M. S. Thesis, National Tsing Hua University, 2001.
- [40] 林鳳瑜, "Fabrication and measurement of two-dimensional and three-dimensional photonic crystal," M. S. Thesis, National Tsing Hua University, 2002.

- [41] 闕欣男, "Localized defect modes calculation of photonic crystal," M. S. Thesis, National Chiao Tung University, 2001.
- [42] 侯鴻龍, "The basic study of different 2-D photonic crystal structures," M. S. Thesis, National Chiao Tung University, 2000.
- [43] 林永倫, "Negative index of refraction phenomenon in photonic crystal," M. S. Thesis, National Chiao Tung University, 2002.
- [44] T. W. Lu, P. T. Lin, K. U. Sio, and P. T. Lee, "Square lattice photonic crystal point-shifted nanocavity with lowest-order whispering-gallery mode" *Opt. Express*, vol. 18, no. 3, pp. 2566-2572, 2010.
- [45] L. W. Chung and S. L. Lee, "Multimode-interference-based broad-band demultiplexers with internal photonic crystals," *Opt. Express*, vol. 14, no. 11, pp. 4923-4927, 2006.
- [46] C. C. Lin and S. L. Tsao, "Multimode interference-based heterostructure photonic crystal waveguide power splitter," *Proceedings of SPIE*, vol. 5907, 9 pages, 2005.
- [47] T. Y. Tsai, Z. C. Lee, J. R. Chen, C. C. Chen, Y. C. Fang, and M. H. Cha, "A novel ultra compact two-mode-interference wavelength division multiplexer for 1.5- μm operation," *Opt. Lett.*, vol. 41, no. 5, pp. 741-746, 2005.
- [48] T. H. Chang, S. H. Chen, C. C. Lee, and H. L. Chen, "Fabrication of autocloned photonic crystals using electron-beam guns with ion-assisted deposition," *Thin Solid Films*, vol. 516, pp.1051-1055, 2008.
- [49] T. H. Chang, S. H. Chen, C. H. Chan, Y. W. Yeh, C. C. Lee and C. C. Chen, "Fabrication of three-dimensional photonic crystals using autocloning layers on the self-assembled microspheres," *Opt. Eng.*, vol. 48, no. 7, pp. 073401-1~5, 2009.
- [50] M. A. Duguay, Y. Kokubun, T. L. Koch, and L. Pfeiffer, "Antiresonant reflecting optical waveguides in SiO₂-Si multilayer structures," *Appl. Phys. Letters*, vol. 49, no. 1, pp. 13-15, 1986.

- [51] T. Baba, Y. Kokubun, T. Sakaki, and K. Iga, "Loss reduction of an ARROW waveguide in shorter wavelength and its stack configuration," *J. Lightwave Technol.* vol. 6, no. 9, pp. 1440-1445, 1988.
- [52] W. Huang, R. M. Shubair, A. Nathan, and Y. L. Chow, "The model characteristics of ARROW structures," *J. Lightwave Technol.*, vol. 10, no. 8, pp. 1015-1022, 1992.
- [53] J. M. Kubica, "A rigorous design method for antiresonant reflecting optical waveguides," *IEEE Photon. Technol. Lett.*, vol. 6, no. 12, pp. 1460-1462, 1994.
- [54] S. H. Hsu and Y. T. Huang, "A novel Mach-Zehnder interferometer based on dual-ARROW structures for sensing applications," *J. Lightwave Technol.*, vol. 23, no. 12, pp. 4200-4206, 2005.
- [55] T. Baba and Y. Kokubun, "New polarization-insensitive antiresonant reflecting optical waveguides (ARROW-B)," *IEEE Photon. Technol. Lett.*, vol. 1, no. 8, pp. 232-234, 1989.
- [56] T. Baba and Y. Kokubun, "Dispersion and radiation loss characteristics of antiresonant reflecting optical waveguides-numerical results and analytical expressions," *IEEE J. Quantum Electron.*, vol. 28, no. 7, pp. 1689-1700, 1992.
- [57] S. Asakawa and Y. Kokubun, "ARROW-B type polarizer utilizing birefringence in multilayer stripe lateral confinement," *IEEE Photon. Technol. Lett.*, vol. 7, no. 1, pp. 38-40, 1995.
- [58] K. Sakoda, *Optical properties of photonic crystal*, Springer Press, 2001.
- [59] S. G. Johnson and J. D. Joannopoulos, *Photonic crystal: The road from theory to practice*, Kluwer academic publishers group, 4th ed., 2004.
- [60] J. D. Joannopoulos, S. G. Johnson, J. N. Winn, and R. D. Meade, *Photonic crystal: Molding the flow of light*, Princeton University Press, 2nd ed., 2008.
- [61] J. M. Lourtioz, H. Benisty, V. Berger, J. M. Gerard, D. Maystre, and A. Tchebnokov, *Photonic crystal: Towards nanoscale photonic devices*, Springer, 2nd ed., 2008.

- [62] D. W. Prather, S. Shi, A. Sharkawy, J. Murakowski, and G. J. Schneider, *Photonic crystal: Theory, Applications, and Fabrication*, John Wiley & Sons Inc., 2009.
- [63] K. Aygün, B. Shanker, A. A. Ergin, and E. Michielssen, “A two-level plane wave time-domain algorithm for fast analysis of EMC/EMI problems,” *IEEE Trans. Electromagnetic Comp.*, vol. 44, no. 1, pp. 152-164, 2002.
- [64] J. D. Pursel and P. M. Goggans, “A finite-difference time-domain method for solving electromagnetic problems with bandpass-limited sources,” *IEEE Trans. Antennas and Prop.*, vol. 47, no. 1, pp. 9-15, 1999.
- [65] M. Yokoyama and S. Noda, “Finite-difference time-domain simulation of two dimensional photonic crystal surface-emitting laser,” *Opt. Express*, vol. 12, no. 8, pp.2869-2880, 2004.
- [66] K. S. Yee, “Numerical solution of initial boundary value problems involving Maxwell’s equations in isotropic media,” *IEEE Trans. Antennas Propagat.*, AP-14, 302, 1966.
- [67] H. C. Chang and C. P. Yu, “Yee-mesh-based finite difference eigenmode analysis algorithms for optical waveguides and photonic crystals,” *OSA IPR*, IFE4, 2004.
- [68] A. Mekis, S. Fan, and J. D. Joannopoulos, “Absorbing boundary conditions for FDTD simulations of photonic crystal waveguides,” *IEEE Microwave and Guided Wave Letters*, vol. 9, no. 12, pp. 502-504, 1999.
- [69] M. Koshiba, Y. Tsuji, and S. Sasaki, “High-performance absorbing boundary conditions for photonic crystal waveguide simulations,” *IEEE Microwave and Guided Wave Letters*, vol. 11, no. 4, pp. 152-154, 2001.
- [70] T. Tamir, *Guided-wave optoelectronics*, Springer-Verlag, 1990.
- [71] http://ab-initio.mit.edu/wiki/index.php/MIT_Photonic_Bands
- [72] B. P. Hiett, J. M. Generowicz, S. J. Cox, M. Molinari, D. H. Beckett, G. J. Parker, and K. S. Thomas, “Finite element modelling of photonic crystals,” *PREP*, 2001.

- [73] R. C. McPhedran, L. C. Botten, and N. A. Nicorovici, *Advances in the Rayleigh Multipole Method for Problems in Photonics and Phononics*, Springer-Verlag, 2006.
- [74] *BandSOLVE 3.0 User Guide*, Rsoft Design Group, Inc.
- [75] E. Chow, S. Y. Lin, J. R. Wendt, S. G. Johnson, and J. D. Joannopoulos, “Quantitative analysis of bending efficiency in photonic-crystal waveguide bends at $\lambda = 1.55 \mu\text{m}$ wavelengths,” *Opt. Lett.*, vol. 26, no. 5, pp. 286-288, 2001.
- [76] A. Talneau, Ph. Lalanne, M. Agio, and C. M. Soukoulis, “Low-reflection photonic-crystal taper for efficient coupling between guide sections of arbitrary widths,” *Opt. Lett.*, vol. 27, no. 17, pp. 1522-1524, 2002.
- [77] N. Moll and G. L. Bona, “Bend design for the low-group-velocity mode in photonic crystal-slab waveguides,” *Appl. Phys. Lett.*, vol. 85, no. 19, pp. 4322-4324, 2004.
- [78] S. Olivier, H. Benisty, M. Rattier, C. Weisbuch, M. Qiu, A. Karlsson, C. J. M. Smith, R. Houdre, and U. Oesterle, “Resonant and nonresonant transmission through waveguide bends in a planar photonic crystal,” *Appl. Phys. Lett.*, vol. 79, no. 16, pp. 2514-2516, 2001.
- [79] B. Miao, C. Chen, S. Shi, J. Murakowski, and D. W. Prather, “High-efficiency broad-band transmission through a double-60° bend in a planar photonic crystal single-line defect waveguide,” *IEEE Photon. Technol. Lett.*, vol. 16, no. 11, pp. 2469-2471, 2004.
- [80] A. Chutinan, M. Okano, and S. Noda, “Wider bandwidth with high transmission through waveguide bends in two-dimensional photonic crystal slabs,” *Appl. Phys. Lett.*, vol. 80, no. 10, pp. 1698-1700, 2002.
- [81] J. S. Jensen, O. Sigmund, L. H. Frandsen, P. I. Borel, A. Harpøth, and M. Kristensen, “Topology design and fabrication of an efficient double 90° photonic

- crystal waveguide bend,” *IEEE Photon. Technol. Lett.*, vol. 17, no. 6, pp. 1202-1204, 2002.
- [82] A. Têtu, M. Kristensen, L. H. Frandsen, A. Harpøth, P. I. Borel, J. S. Jensen, and O. Sigmund, “Broadband topology-optimized photonic crystal components for both TE and TM polarizations,” *Opt. Express*, vol. 13, no. 21, pp. 8606-8611, 2005.
- [83] A. Mekis, S. Fan, and J. D. Joannopoulos, “Bound states in photonic crystal waveguides and waveguide bends,” *Phys. Rev. B*, vol. 58, no. 8, pp. 4809-4817, 1998.
- [84] S. Blair and J. Goeckeritz, “Effect of vertical mode matching on defect resonances in one-dimensional photonic crystal slabs,” *J. Lightwave Technol.*, vol. 24, no. 3, pp. 1456-1461, 2006.
- [85] Z. Zhang and M. Qiu, “Small-volume waveguide-section high Q microcavities in 2D photonic crystal slabs,” *Opt. Express*, vol. 12, no. 17, pp. 3988-3995, 2004.
- [86] K. Nozaki, S. Kita, and T. Baba, “Room temperature continuous wave operation and controlled spontaneous emission in ultrasmall photonic crystal nanolaser,” *Opt. Express*, vol. 15, no. 12, pp. 7506-7514, 2007.
- [87] M. F. Lu and Y. T. Huang, “Design of a photonic crystal taper coupler with different section lengths based on the multimode interference and the mode matching,” *Jpn J. Appl. Phys.*, vol. 47, no. 3, pp. 1822-1827, 2008.
- [88] A. Mekis and J. D. Joannopoulos, “Tapered couplers for efficient interfacing between dielectric and photonic crystal waveguides,” *J. Lightwave Technol.*, vol. 19, no. 6, pp. 861-865, 2001.
- [89] Y. Xu, R. K. Lee, and A. Yariv, “Adiabatic coupling between conventional dielectric waveguides and waveguides with discrete translational symmetry,” *Opt. Lett.*, vol. 25, no. 10, pp. 755-757, 2000.

- [90] E. H. Khoo, A. Q. Liu, J. H. Wu, J. Li, and D. Pinjala, "Modified step-theory for investigating mode coupling mechanism in photonic crystal waveguide taper," *Opt. Express*, vol. 14, no. 13, pp. 6035-6054, 2006.
- [91] R. S. Balmer, J. M. Heaton, J. O. Maclean, S. G. Ayling, J. P. Newey, M. Houlton, P. D. J. Calcott, D. R. Wight, and T. Martin, "Vertically tapered epilayers for low-loss waveguide–fiber coupling achieved in a single epitaxial growth run," *J. Lightwave Technol.*, vol. 21, no. 1, pp. 211-217, 2003.
- [92] T. D. Happ, M. Kamp, and A. Forchel, "Photonic crystal tapers for ultracompact mode conversion," *Opt. Lett.*, vol. 26, no. 14, pp. 1102-1104, 2001.
- [93] P. Sanchis, J. Blasco, A. Martinez, and A. Garcia, "Mode matching technique for highly efficient coupling between dielectric waveguides and planar photonic crystal circuits," *Opt. Express*, vol. 10, no. 24, pp. 1391-1397, 2002.
- [94] C. W. Chang, S. C. Cheng, and W. F. Hsieh, "High-efficiency coupling between external and photonic crystal waveguides by longitudinally shifting waveguide junctions," *Opt. Commun.*, vol. 242, pp. 517-524, 2004.
- [95] Y. F. Chau, T. J. Yang, and W. D. Lee, "Coupling technique for efficient interfacing between silica waveguides and planar photonic crystal circuits," *Appl. Opt.*, vol. 43, no. 36, pp. 6656-6683, 2004.
- [96] A. Xing, M. Davanço, D. J. Blumenthal, and E. L. Hu, "Transmission measurement of tapered single-line defect photonic crystal waveguides," *IEEE Photon. Technol. Lett.*, vol. 17, no. 10, pp. 2092-2094, 2005.
- [97] L. B. Soldano and E. C. M. Pennings, "Optical multi-mode interference devices based on self-imaging: principles and applications," *J. Lightwave Technol.*, vol. 13, no. 4, pp. 615-627, 1995.

- [98] T. Liu, A. R. Zakharian, M. Fallahi, J. V. Moloney, and M. Mansuripur, "Multimode interference-based photonic crystal waveguide power splitter," *J. Lightwave Technol.*, vol. 22, no. 12, pp. 2842-2846, 2004.
- [99] C. C. Lin and S. L. Tsao, "Multimode interference-based heterostructure photonic crystal waveguide power splitter," *Proceedings of SPIE*, vol. 5907, 9 pages, 2005.
- [100] H. J. Kim, I. Park, B. H. O, S. G. Park, E. H. Lee, and S. G. Lee, "Self-imaging phenomena in multi-mode photonic crystal line-defect waveguides: application to wavelength de-multiplexing," *Opt. Express*, vol. 12, no. 23, pp. 5625-5633, 2004.
- [101] T. Y. Tsai, Z. C. Lee, J. R. Chen, C. C. Chen, Y. C. Fang, and M. H. Cha, "A novel ultra compact two-mode-interference wavelength division multiplexer for 1.5- μm operation," *IEEE J. Quantum Electron.*, vol. 41, no. 5, pp. 741-746, 2005.
- [102] L. W. Chung and S. L. Lee, "Multimode-interference-based broad-band demultiplexers with internal photonic crystals," *Opt. Express*, vol. 14, no. 11, pp. 4923-4927, 2006.
- [103] R. Courant, K. Friedrichs, and H. Lewy, "On difference methods for parabolic equations and alternating direction implicit methods for elliptic equations," *IBM J. Res. Dev.*, vol. 11, p. 215-234, 1967.
- [104] M. Loncar, T. Doll, J. Vuckovic, and A. Scherer, "Design and fabrication of silicon photonic crystal waveguides," *J. Lightwave Technol.*, vol. 18, no. 10, pp. 1402-1411, 2000.
- [105] Ph. Lalanne and A. Talneau, "Modal conversion with artificial materials for photonic-crystal waveguides," *Opt. Express*, vol. 10, no. 8, pp. 354-359, 2002.
- [106] T. Liu, A. R. Zakharian, M. Fallahi, J. V. Moloney, and M. Mansuripur, "Multimode interference-based photonic crystal waveguide power splitter," *J. Lightwave Technol.*, vol. 22, no. 12, pp.2842-2846, 2004.
- [107] M. R. Paiam, C. F. Janz, R. I. MacDonald, and J. N. Broughton, "Compact planar

- 980/1550-nm wavelength multi/demultiplexer based on multimode interference,” *IEEE Photon. Technol. Lett.*, vol. 7, no. 10, pp. 1180-1182, 1995.
- [108] Z. Li, Z. Chen, and B. Li, “Optical pulse controlled all-optical logic gates in SiGe/Si multimode interference,” *Opt. Express*, vol. 13, no. 3, pp. 1033-1038, 2005.
- [109] T. Y. Tsai, Z. C. Lee, J. R. Chen, C. C. Chen, Y. C. Fang, and M. H. Cha, “A novel ultra compact two-mode-interference wavelength division multiplexer for 1.5- μm operation,” *IEEE J. Quantum Electron.*, vol. 41, no. 5, pp. 741-746, 2005.
- [110] X. Jia, S. Luo, and X. Cheng, “Design and optimization of novel ultra-compact SOI multimode interference optical switch,” *Opt. Commun.*, vol. 281, no. 5, pp. 1003-1007, 2008.
- [111] H. J. Kim, I. Park, B. H. O, S. G. Park, E. H. Lee, and S. G. Lee, “Self-imaging phenomena in multi-mode photonic crystal line-defect waveguides: application to wavelength de-multiplexing,” *Opt. Express*, vol. 12, no. 23, pp. 5625-5633, 2004.
- [112] Y. Zhang, Z. Li, and B. Li, “Multimode interference effect and self-imaging principle in two-dimensional silicon photonic crystal waveguides for terahertz waves,” *Opt. Express*, vol. 14, no. 7, pp. 2679-2689, 2006.
- [113] Z. Li, Y. Zhang, and B. Li, “Terahertz photonic crystal switch in silicon based on self-imaging principle,” *Opt. Express*, vol. 14, no. 9, pp. 3887-3892, 2006.
- [114] C. C. Chiang, C. W. Tsai, and S. L. Tsao, “Design and simulation of a novel 32 \times 32 photonic bandgap power switch based on SOI waveguide,” *Opt. Commun.*, vol. 278, no. 1, pp. 42-47, 2007.
- [115] P. K. Wei and W. S. Wang, “A TE-TM mode splitter on lithium niobate using Ti, Ni, and MgO diffusions,” *IEEE Photon. Technol. Lett.*, vol. 6, no. 2, pp. 245-248, 1994.
- [116] Y. Ohtera, T. Sato, T. Kawashima, T. Tamamura, and S. Kawakami, “Photonic

- crystal polarization splitters,” *Electron. Lett.*, vol. 35, no. 15, pp.1271-1272, 1999.
- [117] Y. Y. Li, M. Y. Li, P. F. Gu, Z. R. Zheng, and X. Liu, “Graded wavelike two-dimensional photonic crystal made of thin films,” *Appl. Opt.*, vol. 47, no. 13, pp. C71-C74, 2008.
- [118] D. Taillaert, H. Chong, P. I. Borel, L. H. Frandsen, R. M. De La Rue, and R. Baets, “A compact two-dimensional grating coupler used as a polarization splitter,” *IEEE Photon. Technol. Lett.*, vol. 15, no. 9, pp. 1249-1251, 2003.
- [119] D. R. Solli, C. F. McCormick, R. Y. Chiao, and J. M. Hickmann, “Photonic crystal polarizers and polarizing beam splitters,” *J. Appl. Phys.*, vol. 93, no. 12, pp. 9429-9431, 2003.
- [120] T. Liu, A. R. Zakharian, M. Fallahi, J. V. Moloney, and M. Mansuripur, “Design of a compact photonic-crystal-based polarizing beam splitter,” *IEEE Photon. Technol. Lett.*, vol. 17, no. 7, pp. 1435-1437, 2005.
- [121] C. Y. Guan, J. H. Shi, and L. B. Yuan, “Photonic crystal polarizing and non-polarizing beam splitters,” *Chinese Phys. Lett.*, vol. 25, no. 2, pp. 556-558, 2008.
- [122] Y. Morita, Y. Tsuji, and K. Hirayama, “Proposal for a compact resonant-coupling-type polarization splitter based on photonic crystal waveguide with absolute photonic bandgap,” *IEEE Photon. Technol. Lett.*, vol. 20, no. 2, pp. 93-95, 2008.
- [123] V. Zabelin, L. A. Dunbar, N. Le Thomas, R. Houdre, M. V. Kotlyar, L. O’Faolain, and T. F. Krauss, “Self-collimating photonic crystal polarization beam splitter,” *Opt. Lett.*, vol. 32, no. 5, pp. 530-532, 2007.
- [124] E. Schonbrun, Q. Wu, W. Park, T. Yamashita, and C. J. Summers, “Polarization beam splitter based on a photonic crystal heterostructure,” *Opt. Lett.*, vol. 31, no. 21, pp. 3104-3106, 2006.

- [125] V. Mocella, P. Dardano, L. Moretti, and I. Rendina, "A polarizing beam splitter using negative refraction of photonic crystals," *Opt. Express*, vol. 13, no. 19, pp. 7699-7707, 2005.
- [126] R. Ulrich, "Light-propagation and imaging in planar optical waveguides," *Nouv. Rev. optique.*, vol. 6, no. 5, pp. 253-262, 1975.
- [127] R. Ulrich and G. Ankele, "Self-imaging in homogeneous planar optical waveguides," *Appl. Phys. Lett.*, vol. 27, no. 6, pp. 337-339, 1975.
- [128] D. C. Chang and E. F. Kuester, "A hybrid method for paraxial beam propagation in multimode optical waveguides," *Trans. Microwave Theory Tech.*, vol. MTT-29, no. 9, pp. 923-933, 1981.
- [129] N. Zhu, D. Dai, and S. He, "A hybrid modeling for the theoretical analysis of reflections in a multimode-interference coupler based on silicon-on-insulator nanowires," *Opt. Commun.*, vol. 281, no. 11, pp. 3099-3104, 2008.
- [130] S. M. Liao, "Design and analysis of multimode interference-based photonic crystal polarizing beam splitter," M. S. Thesis, National Chiao Tung University, 2008.
- [131] P. E. Barclay, K. Srinivasan, and O. Painter, "Design of photonic crystal waveguides for evanescent coupling to optical fiber tapers and integration with high- Q cavities," *J. Opt. Soc. Am. B*, vol. 20, no. 11, pp. 2274-2284, 2003.
- [132] M. Notomi, A. Shinya, S. Mitsugi, E. Kuramochi, and H. Y. Ryu, "Waveguides, resonators and their coupled elements in photonic crystal slabs," *Opt. Express*, vol. 12, no. 8, pp. 1551-1561, 2004.
- [133] M. Palamaru and Ph. Lalanne, "Photonic crystal waveguides: out-of-plane losses and adiabatic modal conversion," *Appl. Phys. Lett.*, vol. 78, no. 11, pp. 1466-1468, 2001.
- [134] T. Liang and R. W. Ziolkowski, "Grating assisted waveguide-to-waveguide

- couplers,” *IEEE Photon. Technol. Lett.*, vol. 10, no. 5, pp. 693-695, 1998.
- [135] R. W. Ziolkowski and T. Liang, “Design and characterization of a grating-assisted coupler enhanced by a photonic-band-gap structure for effective wavelength-division demultiplexing,” *Opt. Lett.*, vol. 22, no. 13, pp. 1033-1035, 1997.
- [136] M. E. Potter and R. W. Ziolkowski, ”Two compact structures for perpendicular coupling of optical signals between dielectric and photonic crystal waveguides,” *Opt. Express*, vol. 10, no. 15, pp. 691-698, 2002.
- [137] D. Taillaert, W. Bogaerts, P. Bienstman, T. F. Krauss, P. V. Daele, I. Moerman, S. Verstyft, K. D. Mesel, and R. Baets, “An out-of-plane grating coupler for efficient butt-coupling between compact planar waveguides and single-mode Fibers,” *IEEE J. Quantum Electron.*, vol. 38, no. 7, pp. 949-955, 2002.
- [138] W. Kuang, C. Kim, A. Stapleton, and J. D. O’Brien, “Grating-assisted coupling of optical fibers and photonic crystal waveguides,” *Opt. Lett.*, vol. 27, no. 18, pp. 1604-1606, 2002.
- [139] D. W. Prather, J. Murakowski, S. Shi, S. Venkataraman, A. Sharkawy, C. Chen, and D. Pustai, “High-efficiency coupling structure for a single-line-defect photonic-crystal waveguide,” *Opt. Lett.*, vol. 27, no. 18, pp.1601-1603, 2002.
- [140] P. Pottier, I. Ntakis, and R. M. De La Rue, “Photonic crystal continuous taper for low-loss direct coupling into 2D photonic crystal channel waveguides and further device functionality,” *Opt. Commun.*, vol. 223, pp. 339-347, 2003.
- [141] Y. L. Yang, S. H. Hsu, M. F. Lu, and Y. T. Huang, “Photonic crystal slab waveguides based on antiresonant reflecting optical waveguide structures,” *J. Lightwave Technol.*, vol. 27, no. 14, pp. 2642-2648, 2009.
- [142] M. F. Lu, Y. L. Yang, and Y. T. Huang, “Numerical study of transmission improvement in a photonic crystal waveguide bend by mode matching technique,” *IEEE Photon. Technol. Lett.*, vol. 20, no. 24, pp. 2114-2116, 2008.

- [143] S. G. Johnson, S. Fan, P. R. Villeneuve, and J. D. Joannopoulos, "Guided modes in photonic crystal slabs," *Phys. Rev. B*, vol. 60, pp. 5751–5758, 1999.
- [144] N. M. Litchinitser, A. K. Abeeluck, C. Headley, and B. J. Eggleton, "Antiresonant reflecting photonic crystal optical waveguides," *Opt. Lett.*, vol. 27, no. 18, pp. 1592-1594, 2002.
- [145] Y. L. Yang, S. H. Hsu, M. F. Lu, and Y. T. Huang, "ARROW- based photonic crystal waveguides for efficient coupling with fibers," *12th European Conf. on Integrated Optics (ECIO'05)*, Grenoble, France, April 2005.
- [146] Y. H. Huang, M. F. Lu, S. H. Hsu, and Y. T. Huang, "Photonic crystal waveguides with ARROW-B structure," *The 10th OptoElectronics and Communications Conference (OECC 2005)*, pp. 288-289, Seoul, Korea, July 2005.
- [147] A. V. Lavrinenko, L. H. Frandsen, J. F. Pedersen, and P. I. Borel, "Photonic crystal waveguides based on an antiresonant reflecting platform," *IEEE Proceedings of 2005 7th International Conference on Transparent Optical Networks (ICTON 2005)*, vol. 1, pp. 273-276, July 2005.
- [148] P. R. Villeneuve, S. Fan, S. G. Johnson, and J. D. Joannopoulos, "Three-dimensional photon confinement in photonic crystals of low-dimensional periodicity," *Proc. Inst. Elec. Eng.—Optoelectron.*, vol. 145, pp. 384–390, 1998.
- [149] J. H. Chen, Y. L. Yang, M. F. Lu, Y. T. Huang, and J. M. Shieh, "Fabrication of ARROW-based photonic crystal waveguides for efficient coupling with fibers," *Symposium on Nano Device Technology (SNDT2007)*, Hsinchu, Taiwan, May 2007.

作者簡歷

一、基本資料

姓名：呂明峰
英文姓名：Lu, Ming-Feng
性別：男
出生日期：西元 1963 年 10 月 7 日
籍貫：台灣省嘉義縣
住址：台灣省新竹市光復路二段 301 號 3 樓
電話：(03)5728572, 0922-549836

二、主要學歷

國立交通大學電子研究所博士 2002/09 - 2010/06
(其間 2005/08 - 2006/07 休學一年)
國立交通大學電子研究所碩士 1988/09 - 1990/06
國立成功大學電機工程學系 1981/09 - 1985/06

三、博士論文

多模干涉光子晶體波導元件與 B 型抗諧振反射光波導光子晶體波導元件之研究

Investigation on Multimode Interference Photonic Crystal Waveguide Devices and ARROW-B Photonic Crystal Waveguide Devices

四、著作

(一) 期刊論文：

1. M. F. Lu and Y. T. Huang, "Design of a photonic crystal taper coupler with different section lengths based on the multimode interference and the mode matching," *Japanese Journal of Applied Physics*, vol. 47, no. 3, pp. 1822-1827, Mar. 2008.
2. M. F. Lu, Y. L. Yang, and Y. T. Huang, "Numerical study of transmission improvement in a photonic crystal waveguide bend by mode matching technique," *IEEE Photonics Technology Letters*, vol. 20, no. 24, pp. 2114-2116, Dec. 2008.
3. Y. L. Yang, S. H. Hsu, M. F. Lu, and Y. T. Huang, "Photonic crystal slab

waveguides based on antiresonant reflecting optical waveguide structures,” *IEEE J. Lightwave Technol.*, vol. 27, no. 14, pp. 2642-2648, July 2009.

4. M. F. Lu, S. M. Liao, and Y. T. Huang, “Ultra compact photonic crystal polarization beam splitter based on multimode interference,” *Appl. Opt.*, vol. 49, no. 4, pp. 724-731, Feb. 2010.

(二) 研討會論文：

國際學術會議

1. Y. L. Yang, S. H. Hsu, M. F. Lu, and Y. T. Huang, “ARROW- based photonic crystal waveguides for efficient coupling with fibers,” *The 12th European Conf. on Integrated Optics (ECIOC’05)*, pp. 642-645, Grenoble, France, April 6-8, 2005.
2. Y. H. Huang, M. F. Lu, S. H. Hsu, and Y. T. Huang, “Photonic crystal waveguides with ARROW-B structure,” *The 10th OptoElectronics and Communications Conference (OECC 2005)*, pp. 288-289, Seoul, Korea, July 4-8, 2005.
3. M. F. Lu, Y. L. Yang, and Y. T. Huang, “Efficient 120° photonic crystal waveguide bend by mode matching technique,” *OSA Topical Conference on Nanophotonics (NANO)*, N-155, Hangzhou, China, June 18-21, 2007.
4. M. F. Lu, C. Y. Hong, Y. L. Yang, and Y. T. Huang, “Design of a multimode interference-based 1×2 wavelength-division-demultiplexer on an air-hole photonic crystal,” *The 6th WSEAS International Conference on System Science and Simulation in Engineering (ICOSSSE’07)*, pp. 139-143, Venice, Italy, Nov. 21-24, 2007.

國內學術會議

1. Y. H. Huang, M. F. Lu, S. H. Hsu, and Y. T. Huang, “Photonic crystal waveguides with ARROW-B structure,” *Optics and Photonics Taiwan ’04*, Chung-Li, Taiwan, Dec. 2004.
2. Y. L. Yang, S. H. Hsu, M. F. Lu, and Y. T. Huang, “ARROW-based photonic crystal waveguides,” *Optics and Photonics Taiwan ’04*, Chung-Li, Taiwan, Dec. 2004.
3. M. F. Lu, Y. L. Yang, and Y. T. Huang, “Efficient three-dimensional couplers between single-mode fibers and photonic crystal waveguides based on ARROW-B platforms,” *Optics and Photonics Taiwan ’06*, Hsinchu, Taiwan, Dec. 2006.
4. J. H. Chen, Y. L. Yang, M. F. Lu, Y. T. Huang, and J. M. Shieh, “Fabrication of ARROW-based photonic crystal waveguides for efficient coupling with

fibers,” *Symposium on Nano Device Technology (SNDT 2007)*, Hsinchu, Taiwan, May 10-11, 2007.

5. J. H. Chen, Y. L. Yang, M. F. Lu, Y. T. Huang, and J. M. Shieh, “Fabrication of ARROW-based photonic crystal waveguides for efficient coupling with fibers,” *Optics and Photonics Taiwan '07 (OPT07)*, Taichung, Taiwan, Dec., 2007. (Poster paper award, Optics & Photonics Taiwan 2007.)

五、專利

1. 黃遠東、黃郁惠、呂明峰、許世欣，”B型抗諧振反射光波導結構之光子晶體波導”，中華民國發明專利，2007/10/01。(專利權號：發明第I287648號)
2. 黃遠東、楊玉麟、許世欣、呂明峰，”抗諧振反射光波導結構之光子晶體波導”，中華民國發明專利，2007/10/21。(專利權號：發明第 I288837號)

六、參與之研究計畫

1. 國科會計畫，”抗諧振反射光波導 (ARROW) 結構之二維光子晶體波導研究”，擔任職務：博士班研究生，2003.08-2004.07，計畫編號：NSC 92-2215-E-009-047。
2. 經濟部學界科專計畫，”微光電系統晶片研發計畫”，擔任職務：博士班研究生，2003.12-2005.11。
3. 國科會計畫，”平面光子晶體波導之偏極性研究與極化分光器之設計”，擔任職務：計畫主持人，2006.08-2007.07，計畫編號：NSC 95-2221-E-159-015。
4. 國科會計畫，”光學連線網路中光子晶體多模干涉式群播光交換元件之設計”，擔任職務：計畫主持人，2008.08-2009.07，計畫編號：NSC 97-2221-E-159-003。